CRANFIELD INSTITUTE OF TECHNOLOGY

COLLEGE OF AERONAUTICS

Ph.D. Thesis

Academic Year 1984-1985

I. KUSMARWANTO

GROUND EFFECT ON A ROTOR WAKE

Supervisor: E.A.Boyd

March 1985

This thesis is submitted in partial submission for the degree of Doctor of Philosophy.

TEXT BOUND INTO

THE SPINE

Summary

The effect of the ground on a rotor wake in forward flight has been investigated experimentally in the working section of an 8ft x 4ft straight-through wind tunnel. A three bladed fully articulated rotor with a solidity ratio of 0.07 and diameter of 1.06m, powered by a hydraulic motor, has been tested at a height of 0.47 rotor diameter above a solid ground board which has an elliptical leading edge.

Tests have been run at various low advance ratios (<0.1) with two collective pitch settings.

A three-element hot wire anemometer probe has been used to measure the average value of the three components of velocity simultaneously in the forward half (advancing side) of the rotor wake and in the main stream surrounding it.

The rotor wake and the ground vortices have been visualized by smoke. Surface flow patterns on the ground board have located the interaction region between the rotor wake and the oncoming flow on the ground board.

Theoretical estimates of the flowfield based on Heyson's vortex cylinder model (Ref.2) are compared with the experimental results.

Both experimental results and theoretical estimates show that the ground-induced interference is an upwash and a decrease in forward velocity. The upwash interference opposes the vertical flow through the rotor, and have large effects on the rotor performance in producing thrust. The streamwise interference decelerates the mainstream and becomes more noticeable as the wake boundary is approached.

CONTENTS

		Page
Summary		
List of Contents		
List of Figures		
Notation		
Acknowledgements		
1.	Introduction	1
2.	Background and Previous Work	3
2.1	Rotor wake in ground effect	3
2.2	Previous work	5
3.	Experimental work	7
3.1	Preliminary consideration	7
3.2	Experimental technique	9
3.2.1	Flow visualisation	9
3.2.1.1	Smoke visualisation	9
3.2.1.2	Surface flow visualisation	10
3.2.2	Velocity measurement	10
3.3	Experimental program	11
3.4	Experimental facilities	14
3.4.1	Test rig	14
3.4.1.1	Rotor model	14
3.4.1.2	Rotor support system	14
3.4.1.3	The ground board	14
3.4.1.4	The hydraulic system	16
3.4.2	The constant temperature three-element hot wire anemometer probe	16
3.4.3	The wind tunnel	19
3.4.4	The traversing gear	19
3.4.5	The hot wire signals analysis and data acquisition	21
3.5	Test procedures	24
3.5.1	Calibration test	24
3.5.2	The experimental test	26
4.	Theoretical work	28
5.	Results and discussion	32
5.1	Surface flow visualisation experiment	33
5.2	Smoke visualisation experiment	37
5.2.1	Rotor wake characteristics	37
5.2.2	Ground vortex	42

5.3	Velocity measurement	46
5.3.1	Velocity field characteristic	47
5.3.2	Effects of ground vortex	50
5.3.3	Effects of advance ratios	50
5.3.4	Effects from the ground	51
5.3.5	Comparison with the theoretical model	52
5.3.6	Effects of collective pitch angle settings	53
6.	Concluding remarks	54
References		56
Bibliography		59
Appendix A	Blade circulation and induced velocity of the rotor wake in free air	62
Appendix B	Calculations of velocity vectors from a three-element hot wire anemometer signal	69

FIGURES

1. Rotor vortex wake 4

2. Skewed wake in forward flight 4

3. Grid network for velocity measurements 13

4. Test rig assembly 15

5. Hydraulic system flow chart 17

6. Rotor head and three element hot wire probe 18

7. 8'x4' environmental aerodynamics wind tunnel 20

8. Data acquisition diagram 25

9. Rotor wake model 29

10. Superposion method to obtain ground effect field 29

11. Hot wire probe coordinate system 32

12. Surface flow visualisation 34

13. Position of the interaction boundary at various μ 35

14. Thrust measurement results 36

15. Front boundary of the rotor wake at $\mu = 0.09$ 38

16. Front boundary of the rotor wake at $\mu = 0.079$ 39

17. Front boundary of the rotor wake at $\mu = 0.063$ 40

18. Rotor wake in ground effect at hover 41

19. Rotor wake in ground effect at $\mu = 0.079$ 43

20. Smoke picture of the ground vortex at $\mu = 0.09$ 44

21. Smoke picture of the ground vortex at $\mu = 0.079$ 45

22. Planar planes to represent the flow field 48

23. Flow velocity vectors in the X-Z plane, $y/R = 0$, $\theta = 16$, $\mu = 0.09$, $\chi = 56.5$ 72

24. Flow velocity vectors in the X_1-Z_1 plane, $y/R = 0.19$, $\theta = 16$, $\mu = 0.09$ 73

25. Flow velocity vectors in the X_2-Z_2 plane, $y/R = -0.38$, $\theta = 16$, $\mu = 0.09$ 74

26. Flow velocity vectors in the X_3-Z_3 plane
$y/R = -0.57$, $\theta = 16$, $\mu = 0.09$ 75

27. Flow velocity vectors in the X_4-Z_4 plane
$y/R = -0.76$, $\theta = 16$, $\mu = 0.09$ 76

28. Flow velocity vectors in the X_5-Z_5 plane
$y/R = -0.94$, $\theta = 16$, $\mu = 0.09$ 77

29 Flow velocity vectors in the X_6-Y_1 plane
$z/R = -0.15$, $\theta = 16$, $\mu = 0.09$ 78

30. Flow velocity vectors in the X_7-Y_1 plane,
$z/R = -0.55$, $\theta = 16$, $\mu = 0.09$ 79

31. Flow velocity vectors in the X_8-Y_3 plane,
$z/R = -0.79$, $\theta = 16$, $\mu = 0.09$ 80

32. Flow velocity vectors in the X-Z plane,
$y/R = 0$, $\theta = 16$, $\mu = 0.079$, $\chi = 45$ 81

33. Flow velocity vectors in the X_1-Z_1 plane,
$y/R = -0.19$, $\theta = 16$, $\mu = 0.079$ 82

34. Flow velocity vectors in the X_2-Z_2 plane,
$y/R = -0.38$ $\theta = 16$, $\mu = 0.079$ 83

35. Flow velocity vectors in the X_3-Z_3 plane,
$y/R = -0.57$, $\theta = 16$, $\mu = 0.079$ 84

36. Flow velocity vectors in the X_4-Z_4 plane,
$y/R = -0.76$, $\theta = 16$, $\mu = 0.079$ 85

37. Flow velocity vectors in the X_5-Z_5 plane,
$y/R = -0.94$, $\theta = 16$, $\mu = 0.079$ 86

38. Flow velocity vectors in the X_6-Y_1 plane,
$z/R = -0.15$, $\theta = 16$, $\mu = 0.079$ 87

39. Flow velocity vectors in the X_7-Y_2 plane,
$z/R = -0.55$, $\theta = 16$, $\mu = 0.079$ 88

40. Flow velocity vectors in the X_8-Y_3 plane,
$z/R = -0.79$, $\theta = 16$, $\mu = 0.079$ 89

41. Flow velocity vectors in the X-Z plane,
$y/R = 0$, $\theta = 16$, $\mu = 0.063$, $\chi = 37^{o}$ 90

42. Flow velocity vectors in the X_1-Z_1plane,
$y/R = -0.19$, $\theta = 16$, $\mu = 0.063$ 91

43. Flow velocity vectors in the X_2-Z_2plane,
$y/R = -0.38$, $\theta = 16$, $\mu = 0.063$ 92

44. Flow velocity vectors in the X_3-Z_3 plane,
$y/R = -0.76$, $\theta = 16$, $\mu = 0.063$ 93

45. Flow velocity vectors in the X_4-Z_4 plane
$y/r = -0.76$, $\theta = 16$, $\mu = 0.063$ 94

46. Flow velocity vectors in the X_5-Z_5 plane
$y/R = -0.94$, $\theta = 16$, $\mu = 0.063$ 95

47. 3-D sketch of a rotor wake in ground effect 96

48. Model velocity vectors in the X-Z plane,
$y/R = 0$, $\mu = 0.09$, $\chi = 56.5$ 97

49. Model velocity vectors in the X_3-Z_3 plane,
$y/R = -0.57$, $\mu = 0.09$ 98

50. Model velocity vectors in the X-Z plane,
$y/R = 0$, $\mu = 0.079$, $\chi = 45$ 99

51. Model velocity vectors in the X_3-Z_3 plane,
$y/R = -0.57$, $\mu = 0.079$ 100

52. Model velocity vectors in the X-Z plane,
$y/R = 0$, $\mu = 0.063$, $\chi = 37$ 101

53. Model velocity vectors in the X_3-Z_3 plane,
$y/R = -0.57$, $\mu = 0.063$ 102

54. Flow velocity vectors in the X-Z plane,
$y/R = 0$, $\theta = 10$, $\mu = 0.09$, $\chi = 63$ 103

55. Flow velocity vectors in the X-Z plane,
$y/R = 0$, $\theta = 10$, $\mu = 0.079$, $\chi = 58$. 104

ACKNOWLEDGEMENTS

I should like to express my deepest gratitude to my supervisor Mr.E.A.Boyd for his friendly support, guidance and constant encouragement throughout the course of this research work, together with his advice during the writing of the draft of this thesis.

My sincere thanks also to Professor J.L.Stollery for his support and encouragement during my study at the Aerodynamics Department College of Aeronautics.

Special thanks to Mr.M.Dunkley and Mr.E.W.Osbourn for their help, assistance and friendly advice in testing, setting and preparing for all of my experiments.

Many thanks to all members of the Department of Aerodynamics technical staff, particularly: Mr.M.Goodridge, Mr.C.Boddington, Mr.P.Dancers, Mr.T.Atkins and Mr.J.Churchill who expertly manufactured and modified my test rig. Also, Mr.M.Watts and Mr.B.Stone who cheerfully rigged the test equipment in the tunnel.

My thanks to all my colleagues in the Department of Aerodynamics, particularly Miss E.Kilkenny and Mr.J.Mathews for their patient help with my computing problem and specially Dr.K.Garry who always gave me more time in the 8'x4' tunnel.

I am indebted to Mrs.Tricia Forrest-Holden and Ms.S.F.Hagan who checked and corrected my original text and expertly typed this manuscript.

NOTATION

h	height of rotor above the ground board
R	rotor radius
R_c	distance from point at (x,y,z) to edge of rotor disk at ψ.
x,y,z	coordinate system in the wind tunnel
u,v,w	components of velocity along x,y,z axis, positive when directed along positive direction of axis
U_∞	tunnel free stream
λ	rotor inflow ratio, $(U_\infty \sin\alpha + w_o)/\Omega R$
μ	rotor advance ratio, $(U_\infty \cos\alpha)/\Omega R$
α	tip path plane, angle of attack
Ω	rotor rotational speed
χ	wake skew angle between negative z-axis and rotor wake, positive rearward, $\tan^{-1}(-\mu/\lambda)$ (for $\alpha = 0$)
ψ	rotor azimuth angle, positive counter clockwise from downstream position
A	rotor disk area
b	number of blades on a rotor
c	blade chord
T	rotor thrust
C_T	rotor thrust coefficient
r	root cut out radius
σ	rotor solidity $= \frac{be(R-r)}{A}$
θ	collective pitch angle

1. Introduction

A lifting rotor experiences a favourable interference when operating close to the ground due to the changes in the flow pattern underneath the rotor. Performance in forward flight close to the ground has significant effects on the operational utility of helicopters.

It has been shown experimentally that this favourable effect decreases with forward speed and height above the ground. Refs.(6,8). This decrease in ground effect with forward speed plays an important part in determining the maximum take-off performance of an overloaded helicopter from a confined area. Ref.(10). In ground effect, as a result of the interaction between the rotor wake and the oncoming flow, ground vortex is generated. Refs.(4,6).

When the ground vortex is close to the rotor, it dominates the flowfield underneath the rotor. The position of the rotor wake, the ground vortex and the structure of the flowfield surrounding them are important considerations in many practical problems. Among these are;

(a) Predicting the effect from the flowfield on the operation of auxilliary devices.

(b) Estimating the potential for entrainment and transport of ground debris and water droplets.

(c) Estimating the rotor induced loads on helicopter structures other than the rotor.

(d) Calculating and estimating performance, blade dynamic response and stability and control derivatives.

(e) Estimating the potential for exhaust gas reingestion.

We have studied the wake of the rotor and these flowfields experimentally by placing a 1.06m diameter model rotor powered by a hydraulic motor at a distance of 0.5m above a ground board in the working section of a straight-through tunnel. Three advance ratios 0.063, 0.079 and 0.09 were tested with two collective pitch angle settings of 16 and 10 degrees. The three components of velocity were measured by means of a three element hot wire probe which was traversed in the flowfield by a traversing system. This system performs three dimensional traversing controlled by a computer which also received and analysed the probe output signals. A theoretical model was used to compare it with the experimental results and to present a coherent explanation of the tested flowfield and the factors causing them.

2. Background and Previous Work

2.1 Rotor wake in ground effect

Rotor blades may be regarded as high-aspect-ratio wings. In forward flight, they operate in a harmonically varying stream. Associated with the thrust of a rotor blade is a bound circulation.

While the wake and fuselage alter the loading on the blades, the total thrust at a given azimuthal position of the rotor will still be approximately equal to the weight of the aircraft. This implies that the circulation around a given blade will vary approximately sinusoidally with the azimuth angle. The wake of each blade is generated as a thin sheet of vertical fluid. The vorticity in this sheet has components in the spanwise direction (radially shed vorticity) due to the azimuthal variation of the bound circulation, and in the chordwise direction (trailed vorticity) due to the radial variation of the bound circulation. (Fig.1). Because of the rotation of the blades, the thrust and circulation are concentrated towards the tips. While circulation drops to zero at the tip over a finite distance, the rate of decrease is still very high. The result is a large trailing vorticity strength at the outer edge of the wake so that the vortex sheet quickly rolls up into a concentrated tip vortex.

On the span portion of the blade the bound circulation drops down gradually to zero at the root. Therefore there is an inboard sheet of trailed vorticity in the wake with the opposite sign to the tip vortex. (Fig.1). The trailed and shed vorticity of the rotor wake are deposited in the flowfield as the blades rotate and are then convected with the local velocity in the fluid. Shed vorticity does not contribute significantly to the flow at low advance ratios and for computational purposes is ignored. (Ref.5). The local velocity consists of the free stream velocity and the wake self induced velocity.

The wake geometry consists of distorted interlocking helical sheets of vorticity, one behind each blade skewed aft in forward flight.

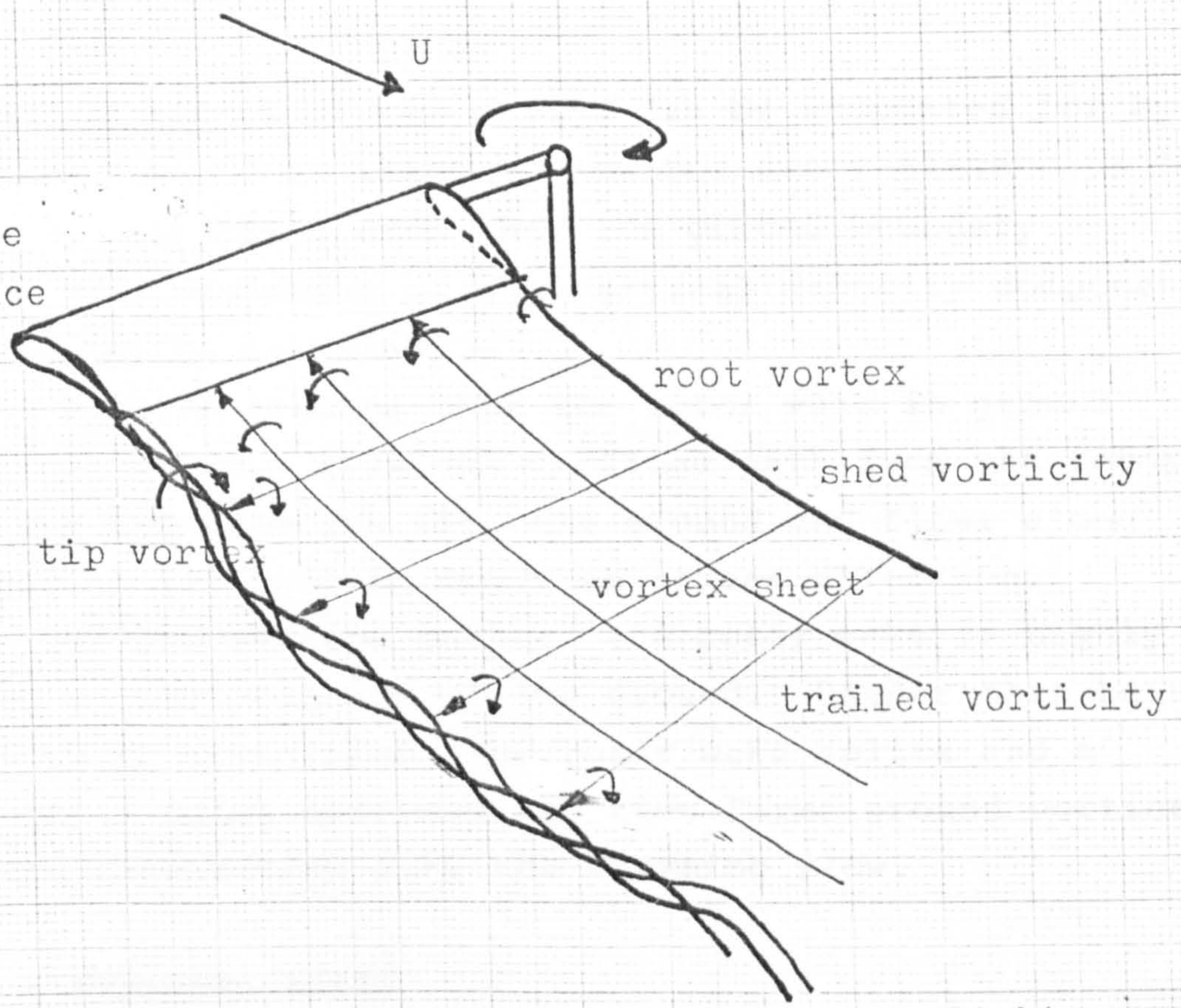

Figure 1- Rotor wake vorticity in forward flight

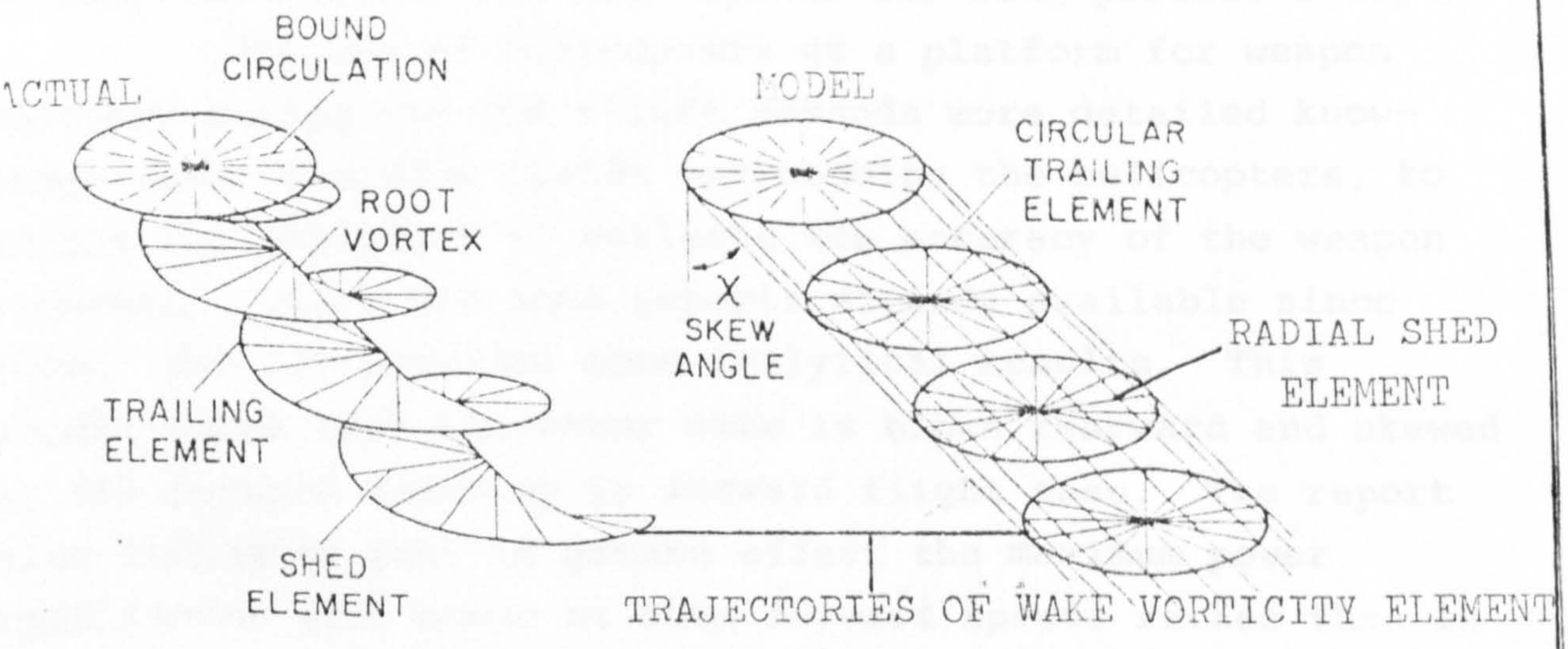

Figure 2 - Skewed wake in forward flight

The effect of the ground can be accounted for by the introduction of an image vortex for every element of the vorticity in the fluid such that the ground boundary condition (the vanishing of the vertical velocity component on the ground) is satisfied.

Ref.(7) assumes that the rotor wake in ground effect flows along a straight inclined path from the rotor disk to its intersection with the ground and flows along the ground to infinity in the free stream direction.

At low advance ratios, the rotor wake is highly distorted by the presence of the ground. Rather than being entirely swept downstream, the rotor wake splits and a portion of it flows upstream and then forms ground vortices due to the interaction with the oncoming flow.

2.2 Previous works

Theoretical and experimental studies of ground effect in forward flight of helicopters have lagged far behind similar studies in hovering.

Only after the army introduced NOE (nap of the earth) concept as an operational doctrine did the need to predict the performance and stability of helicopters to fly at very low heights and slow speeds for long periods emerge.

The use of helicopters as a platform for weapon delivery during the NOE flight demands more detailed knowledge about the flow fields surrounding the helicopters, to enable the designers to evaluate the accuracy of the weapon launched. There are some reports already available since then. Ref.(7) provides some analytical results. This report shows that the rotor wake is blown rearward and skewed by the forward velocity in forward flight case. The report also indicates that in ground effect the maximum power requirement will occur at some forward speeds rather than in hovering.

Ref.(9) reports a wind tunnel test on the adverse effects on tail rotor thrust and power in ground effect. It indicates the effects of the ground vortex (generated by the

interaction of the rotor wake, ground and the oncoming flow) on directional control of helicopters with tail rotors in rearward flight.

Ref.(1) reports the result of powered model wind tunnel investigations carried out by Boeing-Vertol in the 1971-1976 period. The ground vortex is the focal point for the discussion in terms of its occurrence, structure and interaction with the airframe through extensive flow visualisations and model measurements. The flows induced by the ground vortex are shown to lead to aircraft trim distortions, unexpectedly large power required increases, and some very non-linear fuselage loadings.

Ref.(8) reports on the experimental investigations of the aerodynamic characteristics of an isolated rotor operating at low advance ratios near the ground. The paper reports on flow visualization studies in addition to measurements of the forces and moments acting on the rotor as a function of collective pitch angle settings, advance ratios and rotor heights above the ground.

The experimental results show a complex flowfield exists under a thrust producing rotor at low speeds, due to ground proximity, which produces marked changes in the forces and moments.

Ref.(6) reports on our own preliminary effort to investigate a rotor wake in ground effect. The ground vortex is visualized by means of smoke and tufts grid, the interaction boundary, the rotor wake and the freestream flow on the ground by surface flow visualization, and the tangential velocities of the ground vortex are measured, using fine pitot and static tubes to estimate the vortex strength approximately. We have learned that ground effect decreases with the increase of forward speed and height above the ground, and that ground vortex gains strength with the increase of speed until it reaches a peak and then diffuses with a further increase in speed.

These reports do not produce any clear information about the flow field itself.

It is our present aim to provide a data base for the velocities in the flow field experimentally.

3. Experimental work

3.1 Preliminary considerations

The testing of helicopter models in wind tunnels presents many problems that are very different from those encountered in the testing of conventional fixed wing aircraft models. One essential difference between the two types of vehicle is the method of generating lift.

A conventional aircraft obtains its lift from a wing or wings, which may be characterized by moderate values of lift coefficient and relatively low angle of downwash in the flow behind the wings. A helicopter rotor on the other hand, has large values of lift coefficient and its downwash angle (skew angle) varies from 0^{o} at hover to 84^{o}-87^{o} at high speed.

In ground effect, model helicopters will have this large deflection angle with energy added to it. There will be a limit to the maximum rotor size and the lowest advance ratio that can be tested before the wall interference becomes too large and creates additional complexity in the flow field. Refs.(11,13) provide some theoretical estimates of the maximum rotor radius and the maximum skew angle that can be tolerated.

In our case the radius of 0.53m for the tunnel half span of 1.24m and the minimum skew angle of 30^{o} fall within this limit.

In the wind tunnel the simulation of a helicopter flying through stationary air relies on the fact that the details of the flow are not changed by any uniform translatory of the whole configuration. Thus the flow about a helicopter in flight is identical to that about the same vehicle with the rotor rotating at similar rpm placed in a uniform flow with a velocity equal and opposite to that of the vehicle in flight.

For a sealed model of a real helicopter a Froude number similarity is usually employed to scale down the rotor tip speed.

The common method of representing the ground is to use a fixed ground board (Ref.12) or a surface of the tunnel's working section. This requires a relatively simply experimental rig but has the major drawback that a boundary layer inevitably develops on the board. The obvious means of thinning the boundary layer beneath the model position, is to reduce the upstream extension of the ground board. Care must be taken that the flow about its leading edge is not greatly affected by the pressure field of the model, and further reductions of the length of the ground board will cause errors due to the ground not being fully represented.

On the basis of these considerations, we made the following arrangements for our experiments;

1) The tunnel used is a straight-through wind tunnel, parallel all the way downstream. The model fixed on a ground board is approximately 8m downstream from the settling chamber. In this position the boundary layer would be fairly on the tunnel floor. In our preparation we investigated the thickness of the boundary layer at various speeds of the tunnel freestream covering the range to be tested in the helicopter experiments. From these results it was decided to fix the ground board 0.15m above the tunnel floor.

2) To minimize the boundary layer thickness on the ground board we decided to have only 1.2m of the board length upstream of the model. We also had to prevent the leading edge from creating flow separation on the board. An elliptical profile was installed at the edge following (Ref.21) with a length to height ratio of 5 in the ellipse.

3) The freestream (tunnel) flow was always measured 0.3m downstream of the leading edge, so as to allow the flow to reach its designated speed before approaching the rotor wake.

3.2 Experimental technique.

3.2.1 Flow visualization

3.2.1.1 Smoke visualization

This means the injection of smoke into the airflow to make it visible for investigations without changing the density or other properties of the air itself. A convenient way of obtaining this result is mixing the smoke with the airstream. The smoke is generated by a smoke generator with an electrically heated tip which evaporates the paraffin liquid forced to flow through the tip by the pressure in the oil tank set up by an air compressor. The paraffin smoke meets the following requirements:

- possessing the necessary light-scattering quality so that it can readily be photographed.
- non-toxic materials
- sufficient fineness to enable it to follow the flow pattern under investigations.

In controlling the flow of the oil passing through the heated tip, care should be taken to:

- avoid imparting an increase velocity to the flow
- evaporate all of the oil forced to pass through the tip so that the flow is still in its original gaseous nature
- produce sufficient amount of smoke to make the flow being studied easy to photograph.

Rotor tip vortex and ground vortex are the subjects of this technique. We have to realise that although the smoke can record the movement of flow it may not always be seen by the naked eyes. This happens in visualizing unsteady flow which has a fluctuating frequency higher than our eyes can detect. This means that all photographs to record the movement of this unsteady flow should be taken using a high speed camera. The rotor wake is an example of this unsteady flow.

3.2.1.2 Surface flow visualization

A special quick dry paint, made from titanium dioxide powder mixed with raw linseed oil and then lightened by adding paraffin, is painted on the surface of the ground board. When there is an air flow moving on the surface of the board, the paraffin will evaporate leaving the paste to mark the streak lines. The subject of this technique is the interaction boundary between the rotor wake and the freestream flow on the board. The direction of the flow in any particular area of the surface can be traced from the pattern of the streak lines.

3.2.2 Velocity measurement

Two types of velocities were measured in the experiments:

1. the unsteady three components of velocity of the rotor flow field.
2. the steady tunnel flow which determined the advance ratio of the run.

The steady tunnel flow was measured by means of a standard pitot-static probe connected to a micromanometer. The probe should be aligned with the tunnel flow direction. The air density in the tunnel was corrected against the local temperature and pressure.

The unsteady three component of velocities of the rotor flow field were measured using a hot wire probe. The reasons for using the anemometer are:

- the hot wire analyser system has been available
- the hot wire anemoter has high frequency response to accurately follow transients
- the probe is small enough for essential point measurement and minimal flow disturbance
- the anemometer can measure a wide velocity range (min. of 0.1m/s and max. of 200 m/s)
- the system is capable of measuring multi-components of velocity simultaneously.
- the system has low noise

But there are some limitations of the hot wire system such as:

- velocity is not measured directly but is deduced from a measurement of convection heat transfer from the sensor. This means that the results have to depend on preliminary calibrations and settings.
- heat transfer losses from the sensor other than by convection, i.e. by conduction. This is the reason why O.1m/s is the minimum speed that can be accurately measured.

3.3 Experimental program

The aim of our experiments is to meet the need for clearer insights into the flowfield of a helicopter rotor wake in ground effect and its surrounding air, by establishing data base of the velocity field. To achieve this objective the experiments were carried out in three stages:

1. To study how the rotor creates its wake, and what shape this takes in the proximity of the ground. The wake of a rotor is very complex. It consists of vortex sheet left by an individual blade, which is then moved downstream away from the rotor disks, by a combination of freestream velocity and the mean wake induced velocity, at the same time distorting quite considerably under these two components influence. Since the solidity of the rotor is much less than one, the wake and the downwash flow are time dependent. Smoke visualization was used to show the wake shape, the wake edge which is determined by the position of tip vortices and the wake skew angle which is the angle between the wake and the vertical axis. This would allow us to estimate where the rotor wake approaching the ground and the forward portion of the wake. The smoke was then used to visualize the ground vortex. During this stage the smoke was always injected in the longitudinal plane of symmetry of the rotor, upstream of it. All smoke pictures were taken with the camera perpendicular to this plane. As a result the smoke pictures

provide cross-sections of the tip vortices, ground vortices and the shape of the wake. These were qualitative explanations of the real flow which could be used to assist in the interpretation of the flow velocity data measured in this plane of symmetry.

2. To study the interaction boundary between the rotor downwash and the oncoming flow on the ground. As we have seen from our preliminary work (Ref.6) and (Ref.4) this boundary looked like a stagnation region with almost a parabolic shape, and the inner region marks the leading edges of the ground vortices. Surface flow visualization would locate the position of this interaction boundary on the ground board upstream of the rotor. The flow streak lines would show the direction of the flow on the board inside the interaction boundary, and how the flow approaches the interaction boundary.

3. Flow field measurement. The three element hot wire probe was traversed three dimensionally in the flow field by means of the traversing gear, following the grid network as shown in Fig.3. The three components of velocity were measured every 0.05m in the X and Y direction and every 0.03m in the Z direction. The velocity measurements were made as follows:

We started from the longitudinal plane of symmetry of the rotor and from the nearest possible point to the centre of the model and the ground board. With the computer software specially written for this experiment we were able to move the probe first upward and made the measurements every 0.03m until reaching 0.08m under the rotor disk plane. The probe was then moved down to the first Z position and forward to the next X position 0.05m upstream of the previous point and so on until reaching the furthest X position designated. Following this we moved the probe to the next Y position 0.05m to the left of the previous one and started the measurement again from the same X position as the first one and so on until the full network had been completed. These experimental stages (1, 2 and 3) were repeated for three advance ratios and two collective pitch angle settings.

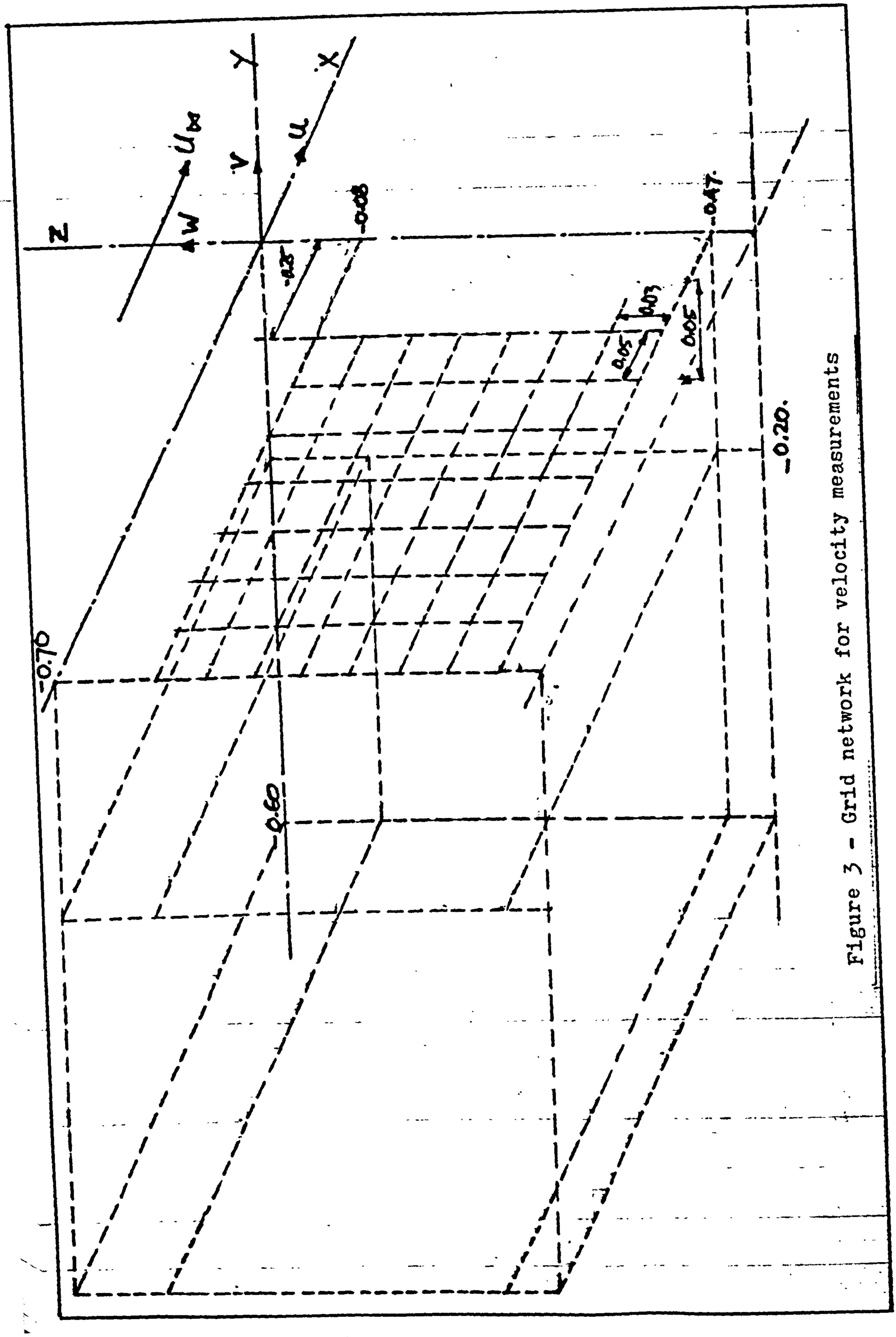

Figure 3 - Grid network for velocity measurements

3.4 Experimental Facilities

All experiments were carried out using facilities and equipment provided by the Aerodynamics Department, Cranfield Institute of Technology.

3.4.1 Test Rig (Fig.4)

The rig consists of:

3.4.1.1 Rotor model

A fully-articulated three bladed rotor model with wooden blades, has a 1.06m diameter. The characteristics of the rotor model are given in Table 1.

TABLE 1 Rotor Model Characteristics

R	Rotor radius (m)	0.53
r	Rotor root cut out (m)	0.215
b	Number of blades	3
σ	Rotor solidity ratio	0.07
n	Rotor r.p.m.	660
ΩR	Rotor tip speed (ms^{-1})	36.63
C	Rotor blade chord (m)	0.065
	Rotor blade profile	NACA 23012
	Rotor blade twist (degrees)	0
γ	Rotor tilt angle (degrees)	0

$M_{tip} = 0.11$

3.4.1.2 Rotor support system

The rotor model is attached to a 0.01m diameter shaft supported by a frame which also acts as a base for the hydraulic motor rotating the shaft and the rotor model. A balance system is connected to the bottom of the shaft, so as to enable the thrust to be measured. A microswitch powered by a D.C. adaptor is placed on the shaft to allow the rotation to be monitored via an electronic tachometer.

3.4.1.3 The Ground Board (Fig.4)

The rotor and its support system is mounted on a

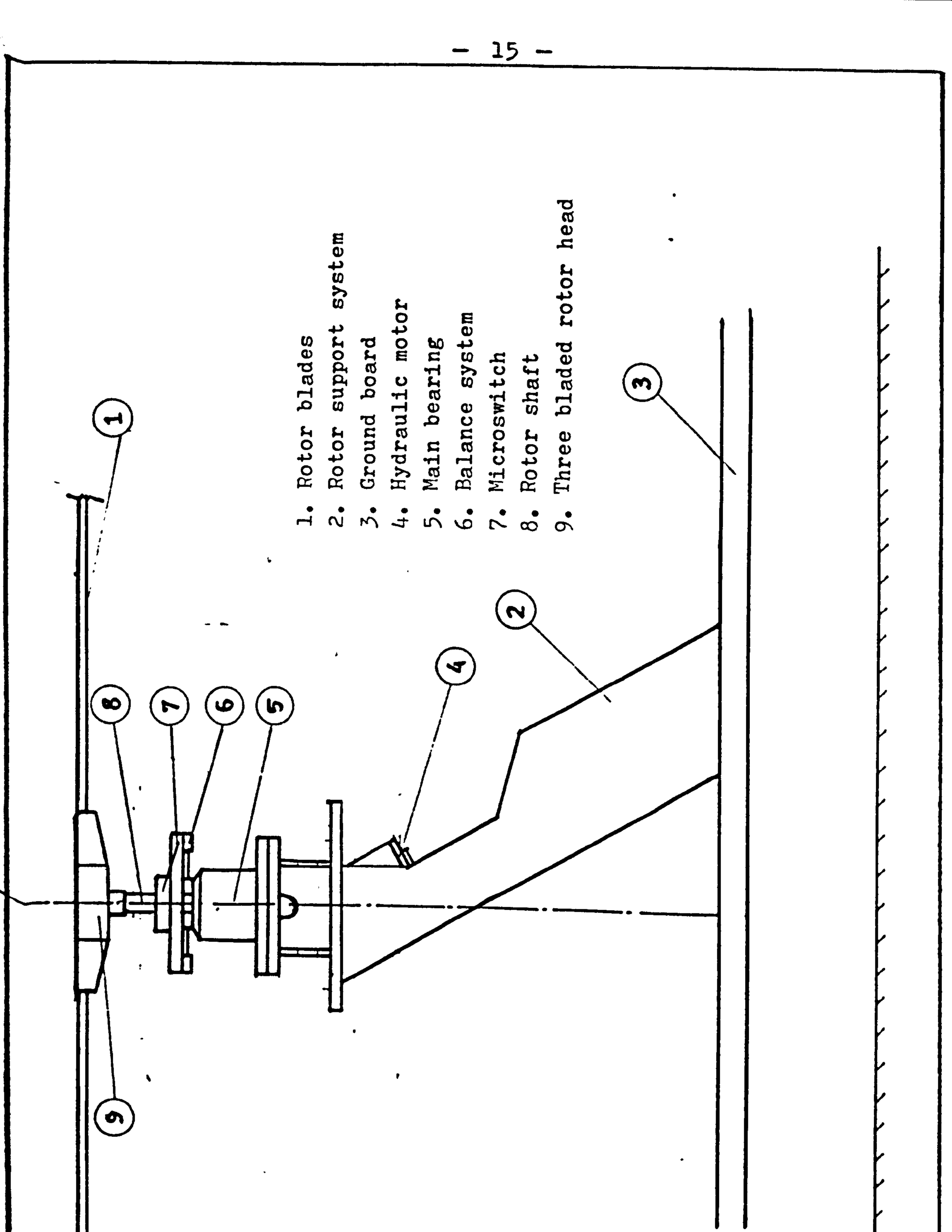

Figure.4. Helicopter Rig General Assembly.

ground board which is 0.025m thick, made of wood. An elliptical profile is fixed at the leading edge to smooth the flow passing over it. This ground board consists of a 1.22m long front section and the rear section where the model and its support mounted. The lower surface of this board was separated at 0.125m from the floor and supported by small blocks during the experiments.

3.4.1.4 The hydraulic system (Fig.5)

To power the hydraulic motor, a hydraulic control system was provided so as to allow the smooth adjustment of the rotor model rotation. It consists of a master hydraulic pump powered by a 20HP electric motor, 2 control valves, 1 high pressure filter to screen the oil and an air cooled radiator to keep the oil temperature low so as to maintain a constant r.p.m. during the tests.

3.4.2 The constant temperature three-element hot wire anemometer probe.

General description:

The probe provides voltages directly proportional to the three components of instantaneous flow velocities at a point in the flow field and to feed these voltages to three analysers capable of extracting the required information. The basic principle is that the small heated probe is placed in the flow and is cooled by the passage of fluid over it. The cooling effect on this probe can be correlated with the fluid velocity by a process of calibration and linearisation.

Technical data:

The three-elements which have individual ground leads, are placed perpendicular to each other forming a right angled coordinate system and are operated by a three anemometer analyser. The combination of the three anemometer signals gives information on the resulting velocity vector and its three components in a reference coordinate system with a fixed orientation with respect to

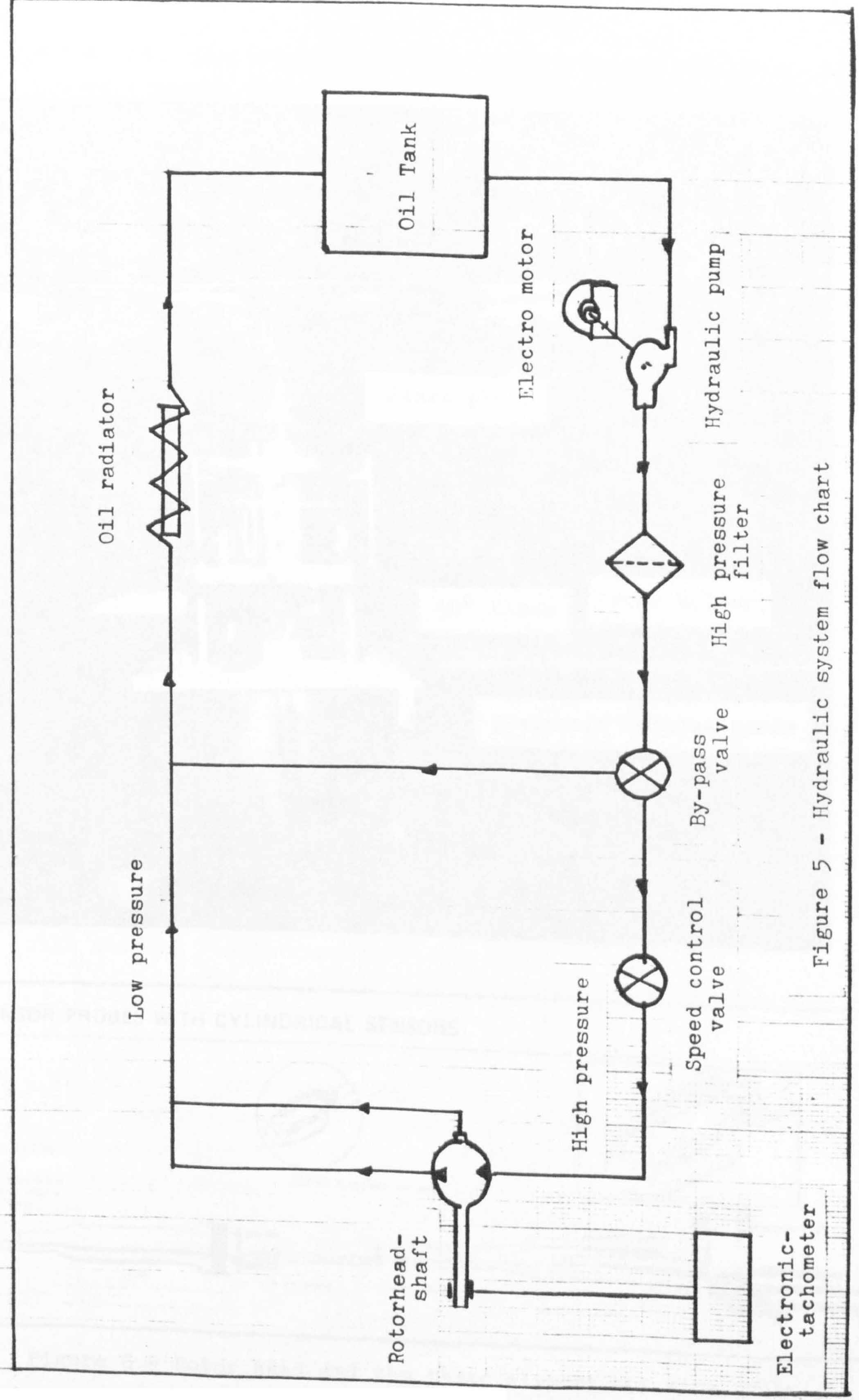

Figure 5 - Hydraulic system flow chart

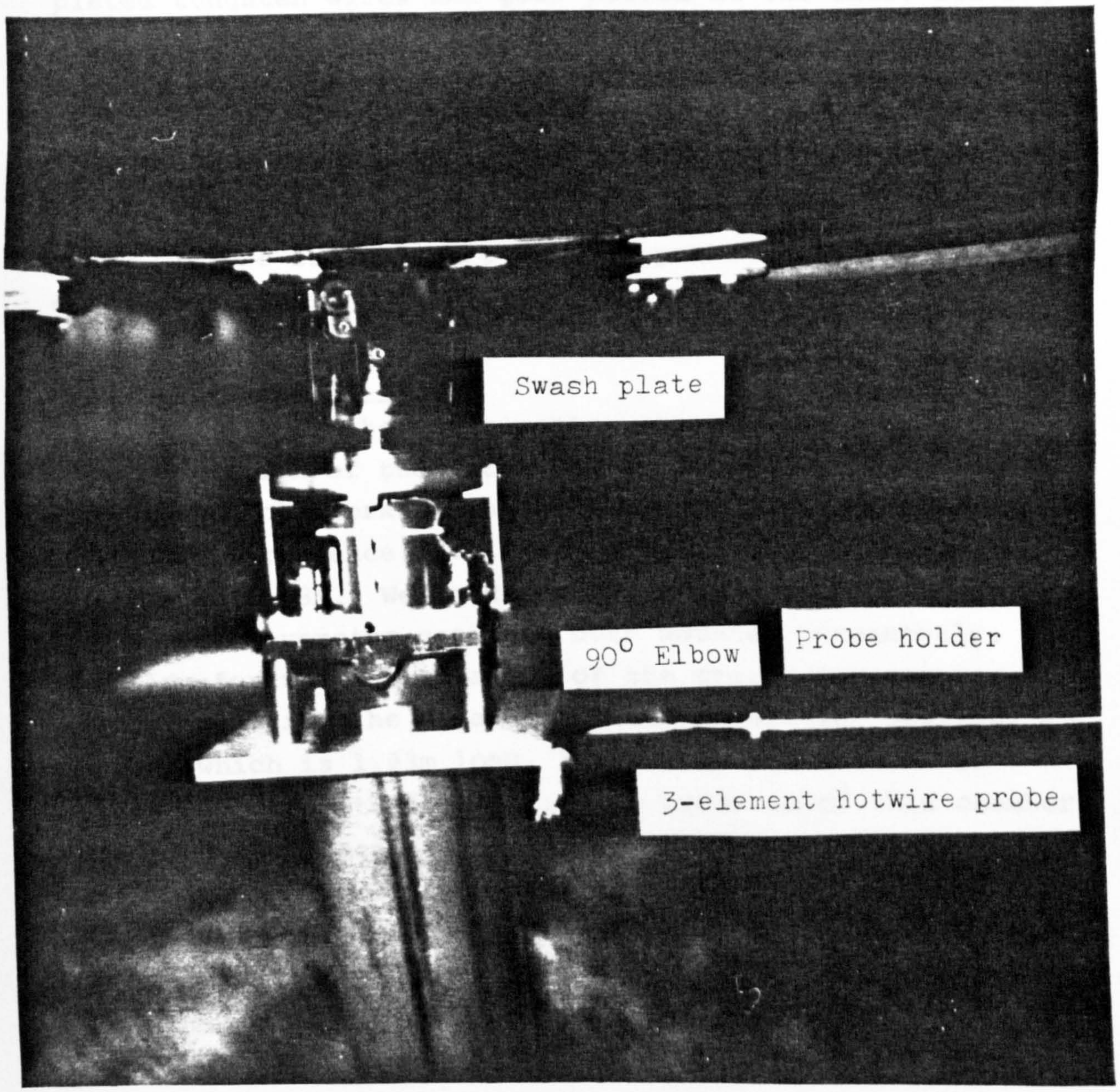

TRIPLE-SENSOR PROBES WITH CYLINDRICAL SENSORS

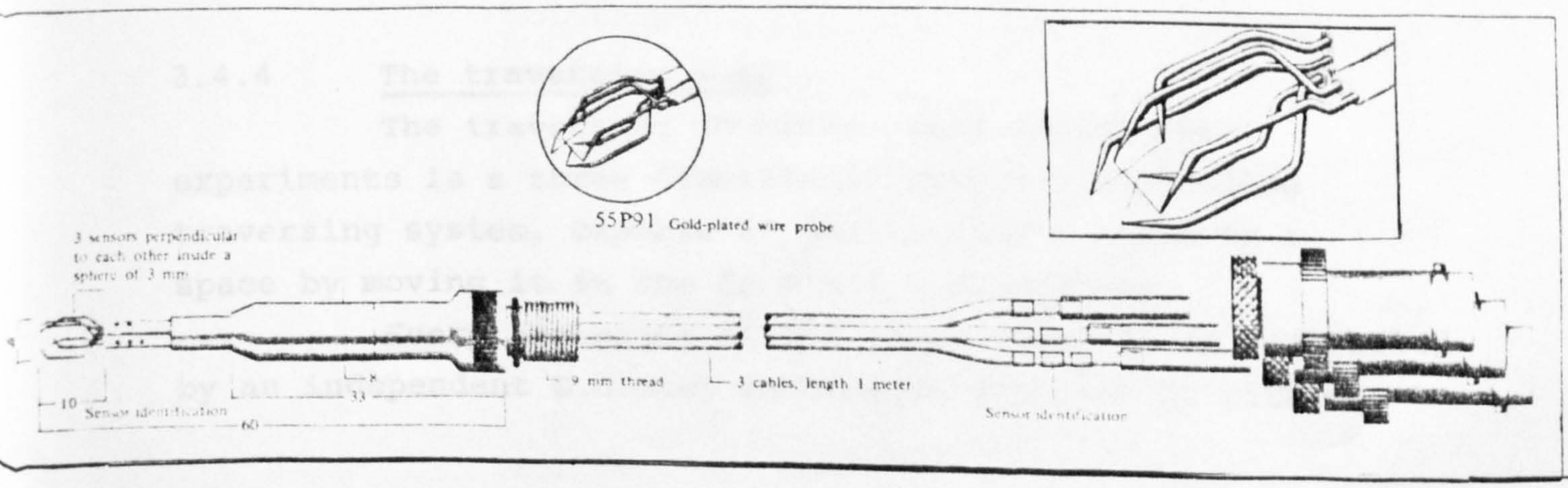

Figure 6 - Rotor head and the three element hot wire probe

the probe. The sensors are 3.2mm long 5 micron platinum-plated tungsten wires and gold plated at the ends, leaving a sensitive length of 1.25mm. These sensors are embedded in ceramic tubings partly covered by a stainless steel tube forming a three-wire probe element, which is mounted in the probe body by soldering. The active portions of the wires are placed inside a sphere of 3mm diameter. The probe picture is in Figure 6. The probe's signals evaluation are in Appendix B.

3.4.3 The wind tunnel

All of the experiments were carried out in the working section of the 8ft x 4ft environmental wind tunnel. This is a close working section, open return tunnel which has a low turbulence level and working section of 2.43m x 1.21m x 18.28m. We used the end of the working section where the traversing gear had been mounted permanently. To allow for the installation of the traversing gear without reducing the area of the tunnel working section, a chamber which is 1.93m long, 2.23m wide and 1.32m high was fixed on the tunnel roof. The pressure of this chamber increased the dimension of the working section where the traversing gear had its operation range. A schematic layout is in Figure 7.

With this arrangement there is an expansion of the flow entering this portion of the working section. The measurement of the tunnel flow should be carried out in this section for an experiment run here.

Ground simulation is achieved by using the ground board.

3.4.4 The traversing gear

The traversing we always used during the experiments is a three dimensional computer controlled traversing system, capable of positioning a probe in a space by moving it in the X, Y and Z directions.

Every dimension of the probe movement is controlled by an independent D.C.step motor with accuracy of within

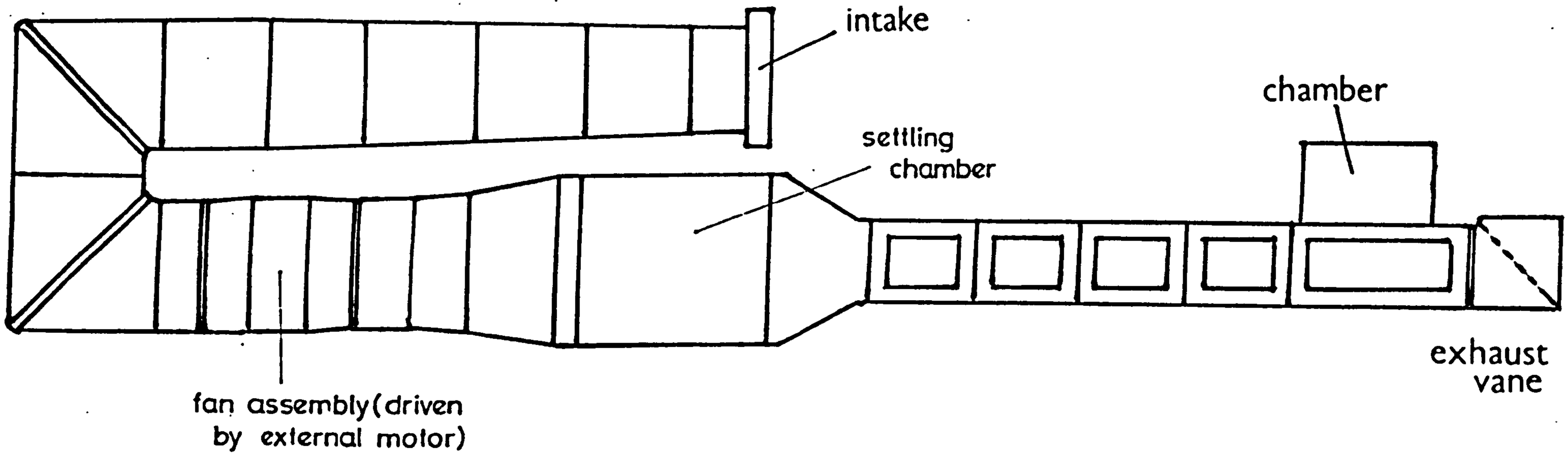

Figure 7
The 8'x4' Enviromental Aerodynamics Wind Tunnel

0.5%. The traversing system is operated via an interface designed to be used either with the parallel interface of the PDP 11 or with the IEEE-488 connection. During our experiments the traversing gear is operated by a PET 2001 computer. The flexibility of the system is that it can be run either manually from the keyboard or automatically (continuously) using written software. The computer keeps track of the traversing position for either ways of running it.

We used the software written for our experiments to operate the traversing gear, to print out the results of the positions and values of the U, V and W components of velocity on the paper and to store them in a floppy disk.

3.4.5 The hot wire signals analysis and data acquisition.

The hot wire anemometer is a thermal device which correlates the heat transfer from a heated sensor with the flow velocity passing over it. Therefore it requires calibration process.

The relationship between flow velocity and output voltage from the anemometer is non-linear and follows approximately the fourth power law (Ref.15), which under certain conditions (unsteady signals) requires linearisation to avoid large errors. The analysis of the convective heat transfer from a heated hot wire probe to the surrounding air can be evaluated using King's law:

$$N_u = A^1 + B^1 Re^n \qquad (1)$$

where N_u = Nusselt number
Re = Reynolds number
A^1 & B^1 = constants

Since $Re = \frac{\rho U d}{\mu}$ and $N_u = \frac{Q}{\ell K (T-T_o)}$ (2)

where: ρ = fluid density
U = flow velocity
μ = fluid viscosity
d = hot wire diameter
ℓ = hot wire length
Q = heat loss from the wire
K = thermal conductivity of the fluid
T & T_o = temperatures of the wire and fluid respectively.

Equation (1) becomes:

$$\frac{Q}{\ell K(T-T_o)} = A^1 + B^1\frac{(\rho Ud)^{n'}}{(\mu)} \qquad (3)$$

The heat loss Q is equal to the electrical power dissipated in the sensor namely V^2/R, where V is the voltage applied across the sensor maintaining its temperature T and R is the sensor resistance. Equation (3) can be rewritten:

$$V^2 = A^1R\ell K(T-T_o) + B^1R\ell K(T-T_o)\left(\frac{\rho Ud}{\mu}\right)^n \qquad (4)$$

or simply:

$$V^2 = A + B\,U^n$$

For U = O then $A = V_o^2$ (voltage output at zero velocity)

Equation (4) can further be simplified to:

$$V^2 - V_o^2 = B\,U^n \qquad (5)$$

V_o depends on flow temperature and wire resistances.

To find the constants B, n and V_o the probe should be placed in a device in which the flow velocity passing over the wire can be controlled and the actual flow velocity is measured accurately using another device.

It is desirable for the calibration to be performed in the actual environment where the actual

measurements are to be made.

For our probe which has three independent wires and produces three output signals which are then combined , to evaluate the U, V and W components of velocity, it is necessary that these outputs should be linearised first before the evaluation process. The reason is that each wire has its own internal resistance and is connected to the analyser via a lead which has its own resistance.

Without linearising the signals the output from the analysers may differ to one another for the same velocity seen by each wire, which then produce wrong results of the U, V and W components from the combination process.

To linearise the signals, outputs from each analyser should be passed through a device called a lineariser which has a transfer function the inverse of King's law. From equation 5, we have written the relations of V_{out} and V_o as:

$$V_{out}^2 - V_o^2 = B\,U^n$$

Linearisers transfer function is used to interpret further.

Consider: $V_{out} = k(V_o^2 + BU^n - C^2)^m$ (6)

where k, m and C are constants produced by the lineariser.

If C is adjusted to equal V_o and m is adjusted to equal $\frac{1}{n}$ then

$$V_{out} = k\,B^{\frac{1}{n}}\,U \quad (7)$$

and $k\,B^{\frac{1}{n}} = K$

The final result is

$$V_{out} = K.U.$$

The output from the lineariser is a voltage directly proportional to the velocity which implies that every wire

can produce a similar output for the same velocity.

Appendix B gives the combination process of the signals from linearisers.

Since the flow velocities that we measured were unsteady, a computer was used to perform the evaluation of the U, V and W components. For this computer evaluation purpose, the output signals from the linearisers should be digitised first using a multichannel 12 bits analogue to digital converter. The computer took forty signals from each channel simultaneously and then averaged them, followed by the evaluation process of the velocities component.

A diagram of this data acquisition process is in Figure 8.

3.5 Test procedures

3.5.1 Calibration tests

The balance system for measuring the thrust and the hot wire anemometer system need calibrating before we can actually use them in the experiments. The thrust measurement instrumentation consists of a D.C. power supply, a digital volt meter, and the balance system fixed onto the rig. The power supply provides the input voltage of the system and the voltmeter is used to read the output voltage. When an input voltage is fed to the balance system, it activates this device and produces an output voltage. If the webs of the balance system are bent by a certain force the reading will change. The difference between those two readings is proportional to the force which bends the webs.

The calibration was carried out by pulling the shaft up with a known force and then increasing the force step by step. A calibration chart was drawn on the basis of the results. This chart was then used to interpret the test results.

Since the sensitivity of the output voltages depends on the input voltage, there should be a constant

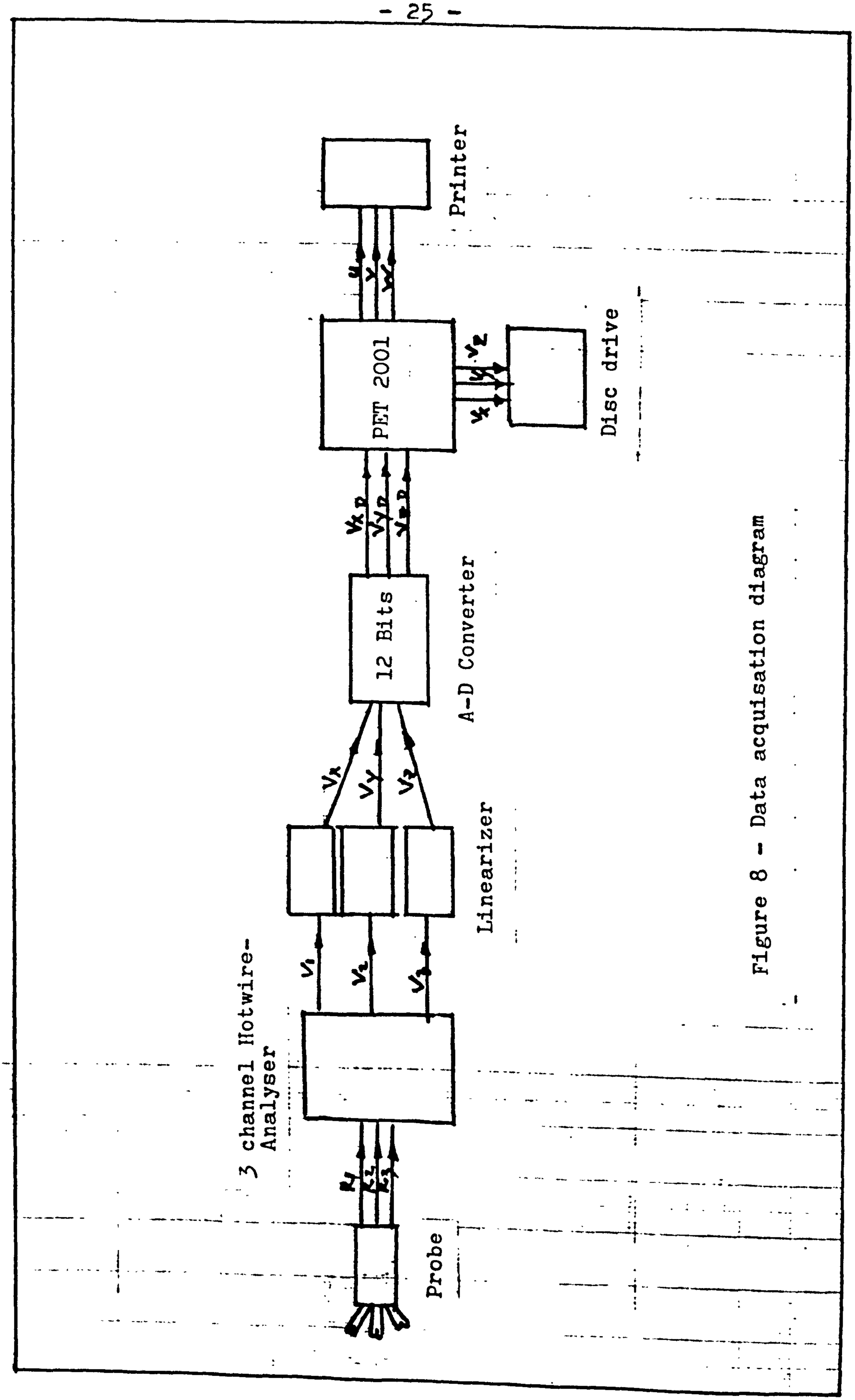

Figure 8 - Data acquisation diagram

voltage input to maintain the validity of the calibration chart.

The hot wire system was calibrated in the tunnel, using the tunnel flow in the working section as the measuring fluid.

The three-element of the anemometer probe can not be totally calibrated at the same time. Instead they have to be calibrated and linearised one by one, since during the calibration each wire being tested should be exactly perpendicular to the flow. An ordinary pitot-static probe connected to a micromanometer was used as a means of reading the flow velocity passing the probe. The hot wire probe and this pitot-static probe were mounted in the centre of the tunnel at the same height and close distance, so as to ensure a similarity in the flow seen by each probe. Then the tunnel was run at various speeds and the linearisers were adjusted until a certain linear proportionality had been obtained for the range of velocities we were interested in (0 - 15ms^{-1}). When all three elements of the probe had been linearised, the probe was positioned in the actual setting for the experiments, and then to check the combination process of the anemometer signals, the tunnel was run again and the printed out result should show the free stream velocity only.

3.5.2 The experimental tests

All tests were started by smoke visualization followed by surface flow visualization and velocity measurements. In every test, the reference free stream flow was measured using the pitot static probe in the region just upstream of the rotor wake. Blockage correction was not applied since the size of the rotor wake was small compared with the area where the chamber had been fixed.

Test conditions are in Table 2.

TABLE 2

μ	advance ratio	0.09,0.079 & 0.063
h	rotor height from the ground board (m)	0.5
θ	collective pitch angle settings (deg)	16, 10
	Mode	Constant speed
	Cyclic pitch	Free
X	Wake skew angle (deg)	0 - 90
ψ	Azimuth angle (deg)	0 - 360
H	rotor height from the tunnel floor (m)	0.65

4. THEORETICAL WORK

There have been some analytical models available and we can see that these models always employ some simplificiations and assumptions, based on flow pictures or physical considerations.

We have chosen the vortex cylinder model (Ref.2) since there seems to be an agreement about the wake shape between the model and our smoke pictures of the rotor wake.

Further assumptions to make:

1. The flow is inviscid and incompressible
2. The blades bound circulation are constant along the radius. This implies that only tip vortices and root vortices leave the blade tips and roots and are carried downward with the speed and direction of the mean flow at the rotor. These vortices thus lie on the surface of the outer cylinder wake (tips) and inner cylinder wake (roots). These vortices are so closely spaced that these two cylinders (outer and inner) may be considered to be two sheets of continuous vorticity. This assumption restricts the analysis to obtaining only the time averaged value of induced velocity.
3. The blades bound circulation is allowed to vary azimuthwise. This implies that the blades also shed radial components of vorticity into the wake.
4. Negligible effects from the root vortices.
5. For small advance ratios ($\mu < 0.1$) the effect from shed vorticity can be ignored.
6. There is no vortex dissipation.

The rotor flow field in free air at point P(x,y,z) can be found by integrating the BIOT SAVART law over the entire wake (Appendix A). The results are:

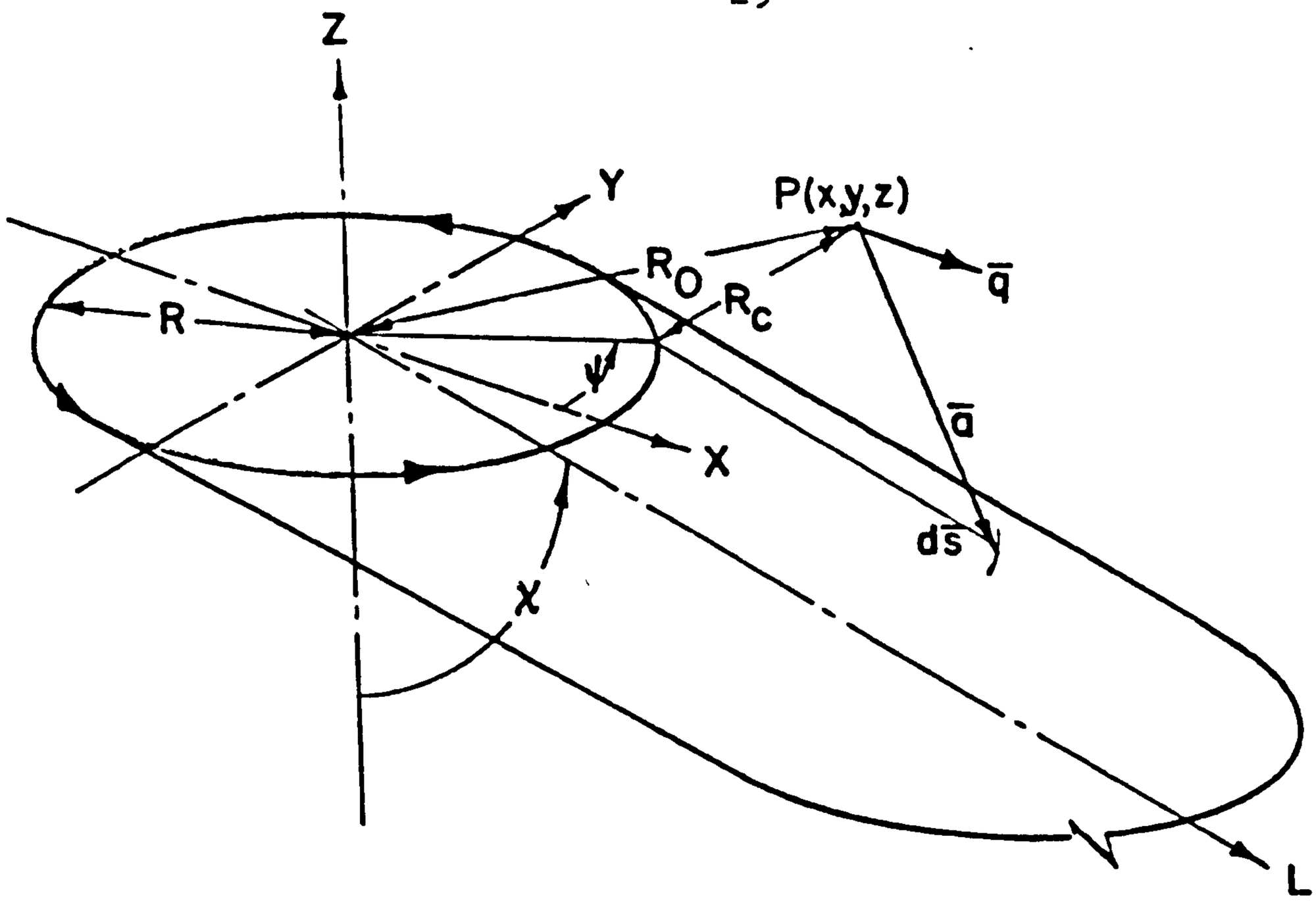

Figure 9 - Rotor wake model in free air

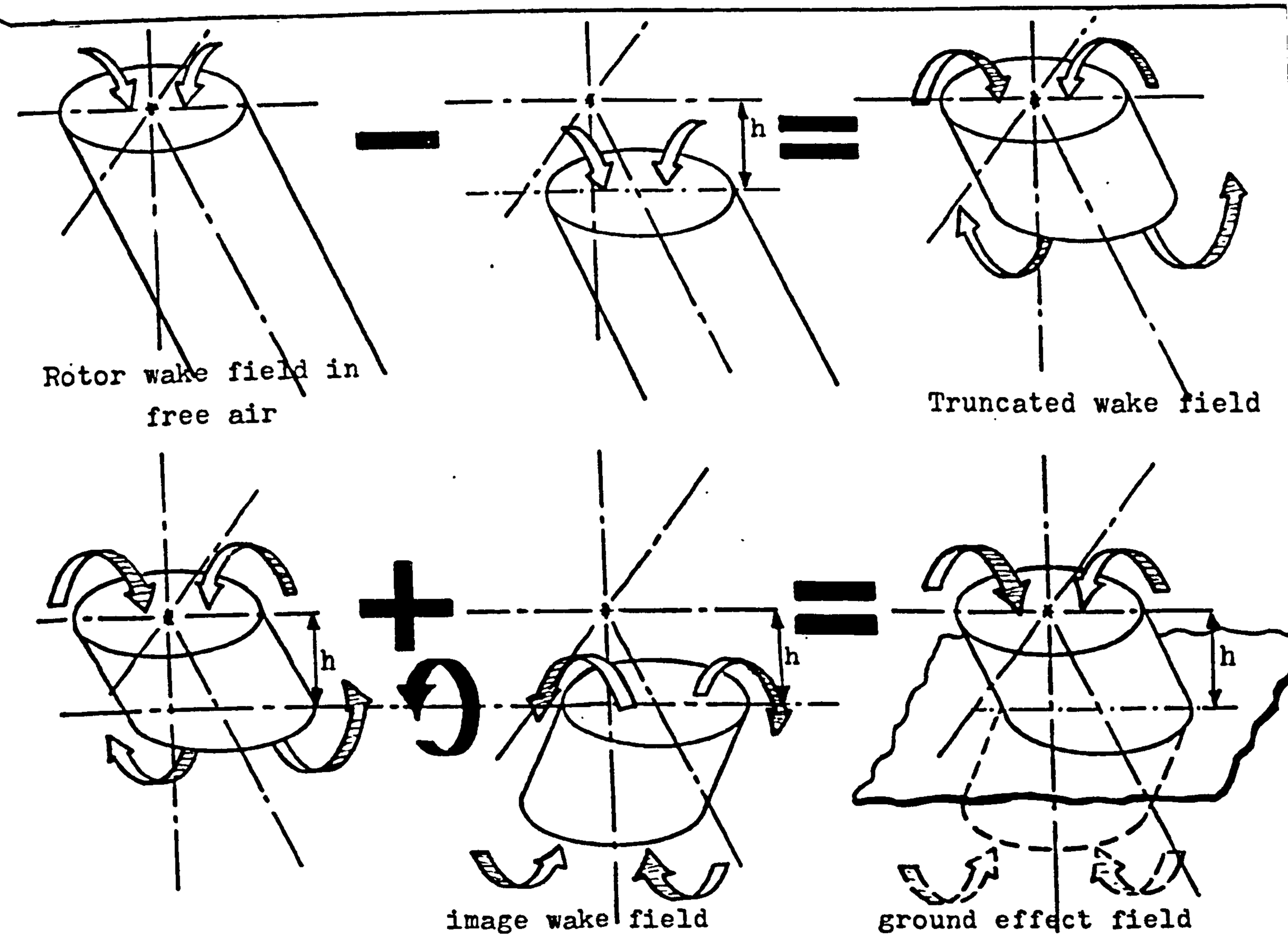

Figure 10 - Superposition method to obtain ground effect field

$$u = U^* \int_0^{2\pi} f(\psi) \left[\frac{\{ (\frac{Z}{R} + \frac{R_C}{R} \cos\chi) \cos\psi \}}{D} \right] d\psi \qquad (1)$$

$$v = U^* \int_0^{2\pi} f(\psi) \left[\frac{\{ (\frac{Z}{R} + \frac{R_C}{R} \cos\chi) \sin\psi \}}{D} \right] d\psi \qquad (2)$$

$$w = U^* \int_0^{2\pi} f(\psi) \left[\{1 - (\frac{X}{R}\cos\psi + \frac{Y}{R}\sin\psi) + \frac{R_C}{R} \sin\chi \cos\psi \}/D \right] d\psi \qquad (3)$$

where

$f(\psi) = (1 + 1.5\mu \sin\psi)$

$U^* = (-U_\infty / 2\pi \tan\chi)$

$$D = \left[\frac{R_C}{R} \{ \frac{R_C}{R} + (\cos\psi - \frac{x}{R})\sin\chi + \frac{z}{R}\cos\chi \} \right]$$

$$R_C = \{ R^2 + x^2 + y^2 + z^2 - 2R(x\cos\psi + y\sin\psi) \}^{0.5}$$

Symbolically, the rotor flow field in free air is written as:

$$(\bar{q}_f) = q_f(\frac{x}{R}, \frac{y}{R}, \frac{z}{R})$$

These results can be superimposed to obtain the flow field in ground effect as indicated in Fig.(10). (Ref.2).

The first step is to translate the velocity field downward and rearward following the wake shape to its point of intersection with the floor and then subtracting the resulting field from the original velocity field in free air to obtain the velocity field of a truncated wake.

Symbolically, the velocity field of the truncated wake is:

$$\bar{q}_{tr} = \bar{q}_f(\frac{x}{R}, \frac{y}{R}, \frac{z}{R}) - \bar{q}(\frac{x}{R} - h \tan\frac{\chi}{R}, \frac{y}{R}, \frac{(z+h)}{R})$$

The next step in evaluating the velocity field in ground effect is to rotate the velocity field of the truncated cylinder wake about the longitudinal axis of its intersection with the ground and add the original truncated velocity field. Thus the total induced velocity field in ground effect is:

$$\bar{q}_G = \bar{q}_f\left(\frac{x}{R},\frac{y}{R},\frac{z}{R}\right) - \bar{q}\left(\frac{x}{R} - h\tan\frac{\chi}{R},\frac{y}{R},\frac{(z+h)}{R}\right)$$

$$-(-1)^p\,\bar{q}\left(\frac{x}{R},-\frac{y}{R},-\left(\frac{(z-2h)}{R}\right)\right.$$

$$-(-1)^p\,\bar{q}\left(\frac{x}{R} - h\tan\frac{\chi}{R},-\frac{y}{R},-\frac{(z+h)}{R}\right)$$

Since the v and w components of the velocity field are reversed during the rotation, p equals 1 for the u component and is zero for the v and w components.

These complex integration equations have been solved numerically by applying Romberg's rule from Ref.(18) with accuracy of 1%.

Since in the flow field we also have U_∞ component in the χ direction, then the total longitudinal component of the flow field is $(U_\infty + U_G)$

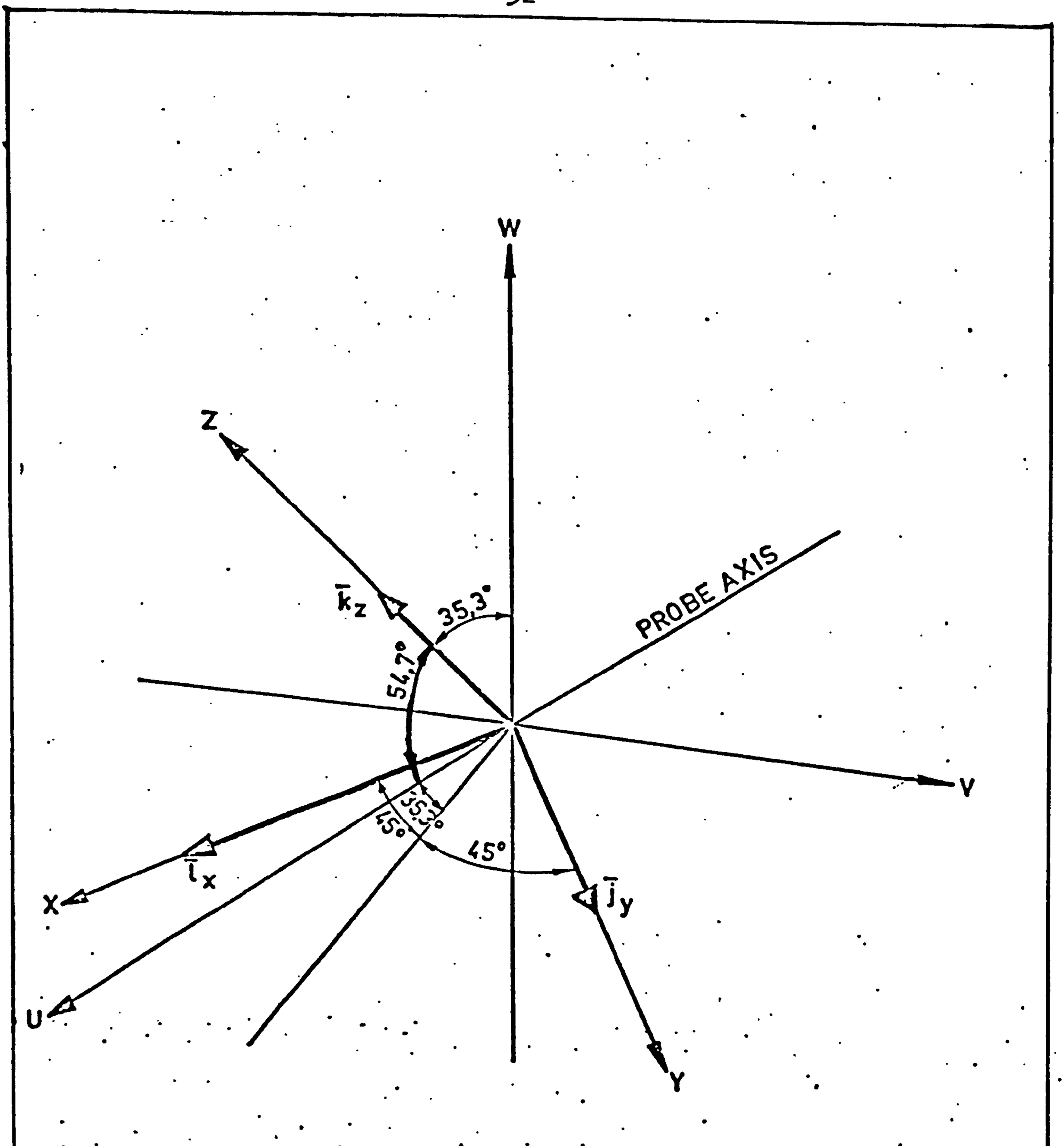

Figure 11 - Hot wire probe coordinate system

5. Results and Discussion

5.1 Surface Flow Visualisation Experiment

Surface flow visualisation explains some facts of the flow behaviour on the ground board such as:

- The boundary formed by the interaction between the oncoming flow (tunnel free stream) and the rotor wake on the ground. From Figs.(12) and (13) and also from Ref.4, this boundary has an approximately parabolic shape. Inside the boundary the flow is moving outward, as shown by the streak lines on the ground.
- The higher the speed of the oncoming flow, the closer the interaction boundary is to the rotor. This implies that this boundary is formed by a kind of local momentum balance between the oncoming flow and the outgoing rotor wake. In fact the position of the boundary in relation to a point at ($h \tan \chi$, 0, -0.5) on the ground is in proportion with the thrust produced by the rotor for various advance ratios. Only at $\mu = 0.09$, the interaction boundary is slightly forward than it should be due to the influence of the ground vortex (will be discussed later). The thrust measurement results in Fig.(14) shows how the thrust decreases with advance ratios, but only slightly in the range of the ratios we tested. This supports the discussion before about the position of the interaction boundary from the rotor.
- The higher the advance ratio, the more asymmetric is the shape of the interaction boundary. The reason is that at a higher speed the advancing side of the rotor produces more lift than the retreating side does. Ref.18 indicates that rotor wake asymmetry resulted from a difference in blade loading. The blade with more loading on the advancing side imparts a greater impulse to the top vortex passing underneath it which has been generated by the preceeding blade. As a result the wake on the retreating side is always weaker, thus causing the asymmetry. Our test rig has got a flapping freedom provided by the three flapping hinges. But since the cyclic pitch is free and the rotor

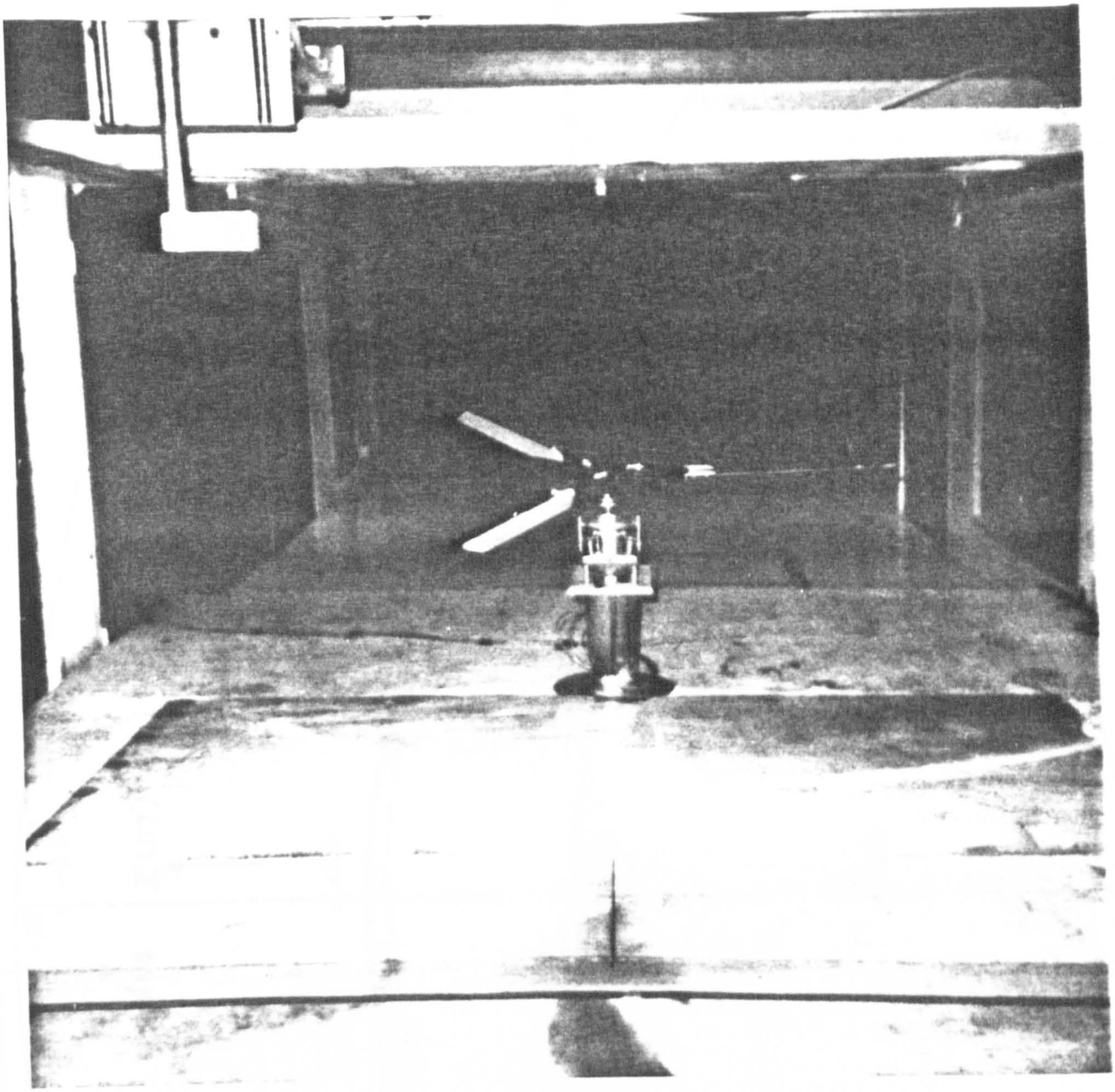

Figure 12 - Surface flow visualization

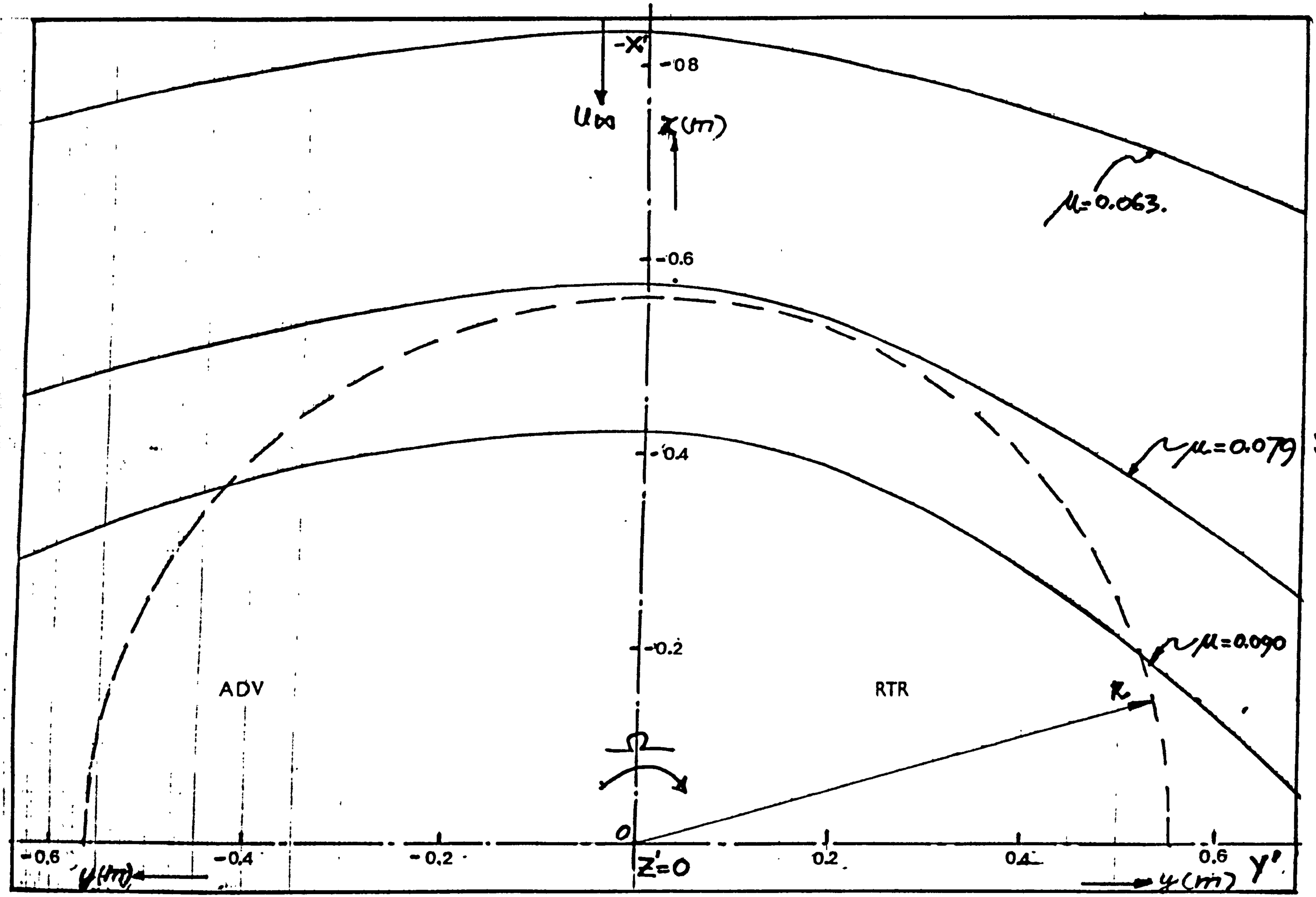

Figure 13 - Position of the interaction boundary at various

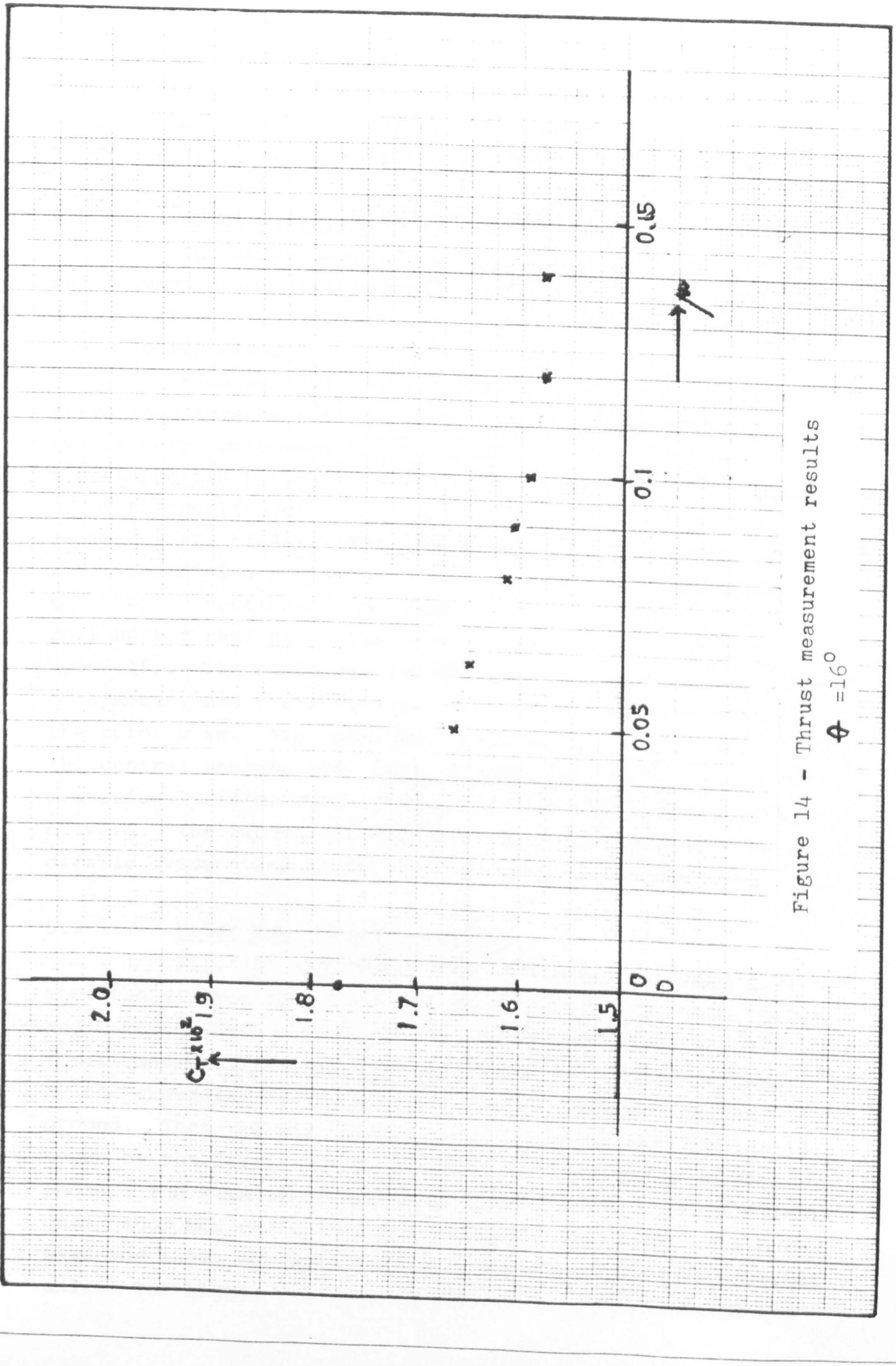

Figure 14 - Thrust measurement results

produces thrust continuously, the blades are coned up. In this situation, the flapping freedom cannot function to balance the thrust produced by the advancing side and the retreating side so as to allow the asymmetry to happen.

5.2 Smoke Visualisation Experiments

The smoke experiment was used to make rotor wake and ground vortex visible and obtain a qualitative global picture of the flow and assist in the interpretation of the velocity field.

Figures (15), (16) and (17) show the rotor wake at various advance ratios. The wake of a rotor contains two primary components. The first and most prominent is the strong tip vortices, which arise from the rapid rolling up of the portion of the vortex sheet shed from the tip region of the blades. The second component is the vortex sheet containing radial and trailing vorticity shed from the inboard section of the blades. This sheet does not roll up but remains in the form of distributed vorticity -(Ref.19). The smoke was injested in the longitudinal plane of symmetry and these figures show only a cross section of the rotor wake. Tip vortices appear as circles in which the central regions are clear of smoke due to the local centrifugal field, which forces the smoke particles radially outward. The top vortex cross sections in the near wake are clearly evident and so is the diffusion of the far wake.

5.2.1 Rotor Wake Characteristics

Fig.(18) from Ref.6 and Figs.(15), (16) and (17) show the visible rotor wake at advance ratios 0, 0.09, 0.079 and 0.063. The hover in ground effect case shows how the rotor wake contracts rapidly in the upper region followed by the expansion of the wake due to the presence of the ground. That the far wake underwent viscous dissipation is shown by the diffusion of the vortices visualised by the smoke. The wake flows radially outward. The forward flight cases show how the oncoming flow pushes the rotor wake backward and skews the wake through an angle χ from the vertical axis. The higher the advance ratio, the more backward the

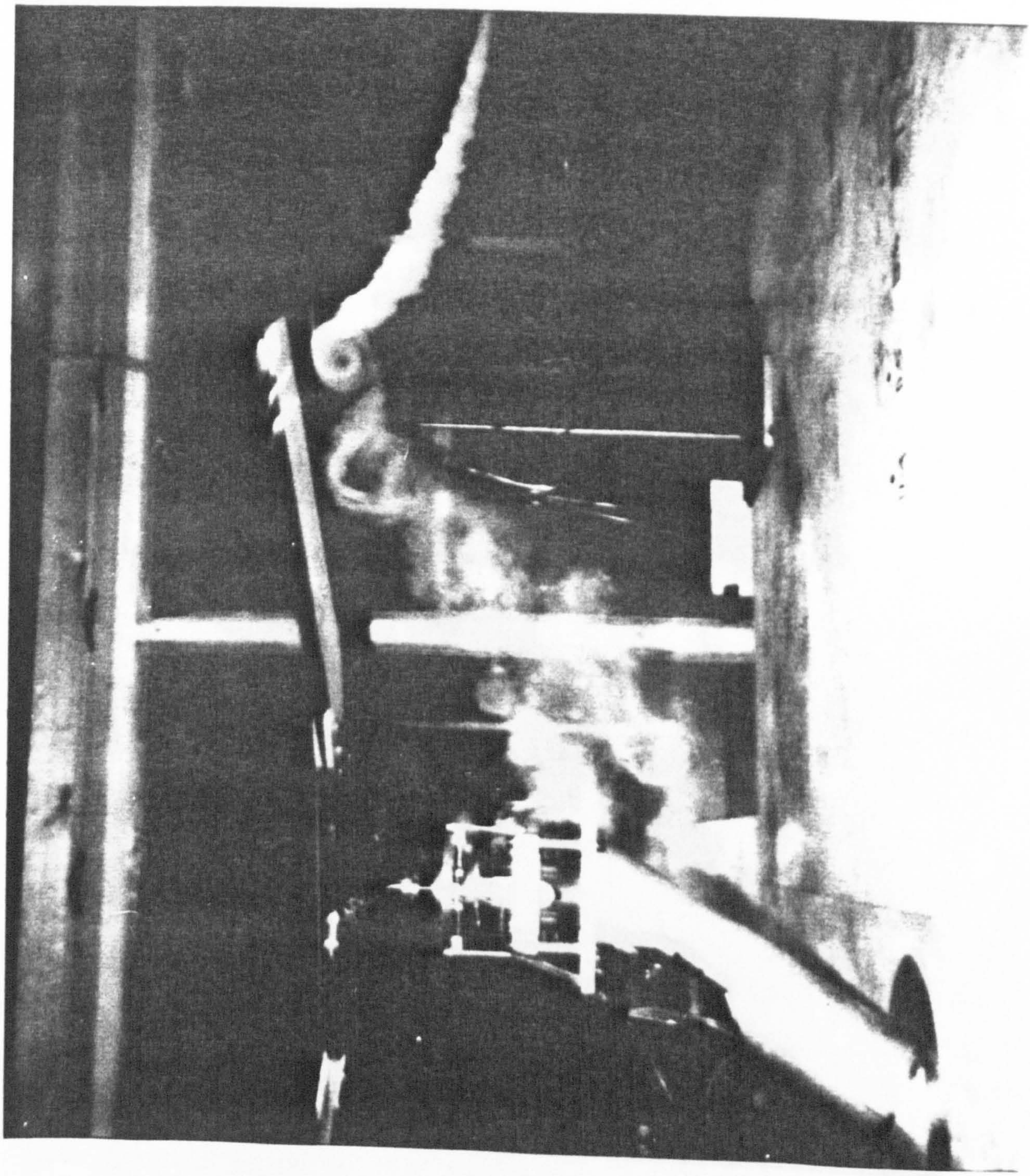

Figure 15 - Front boundary of the rotor wake at M =0.090

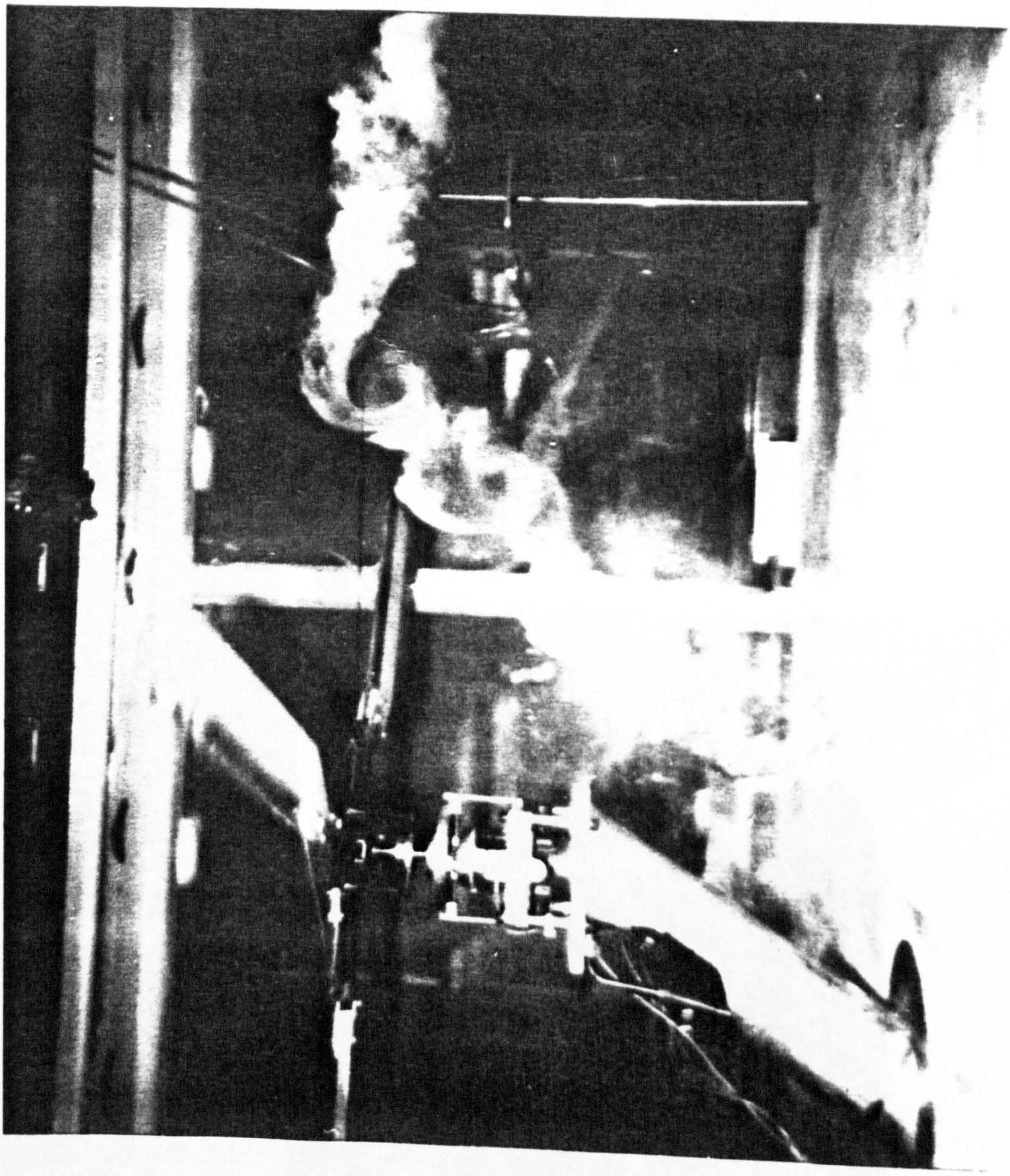

Figure 16 - Front boundary of the rotor wake at μ =0.079

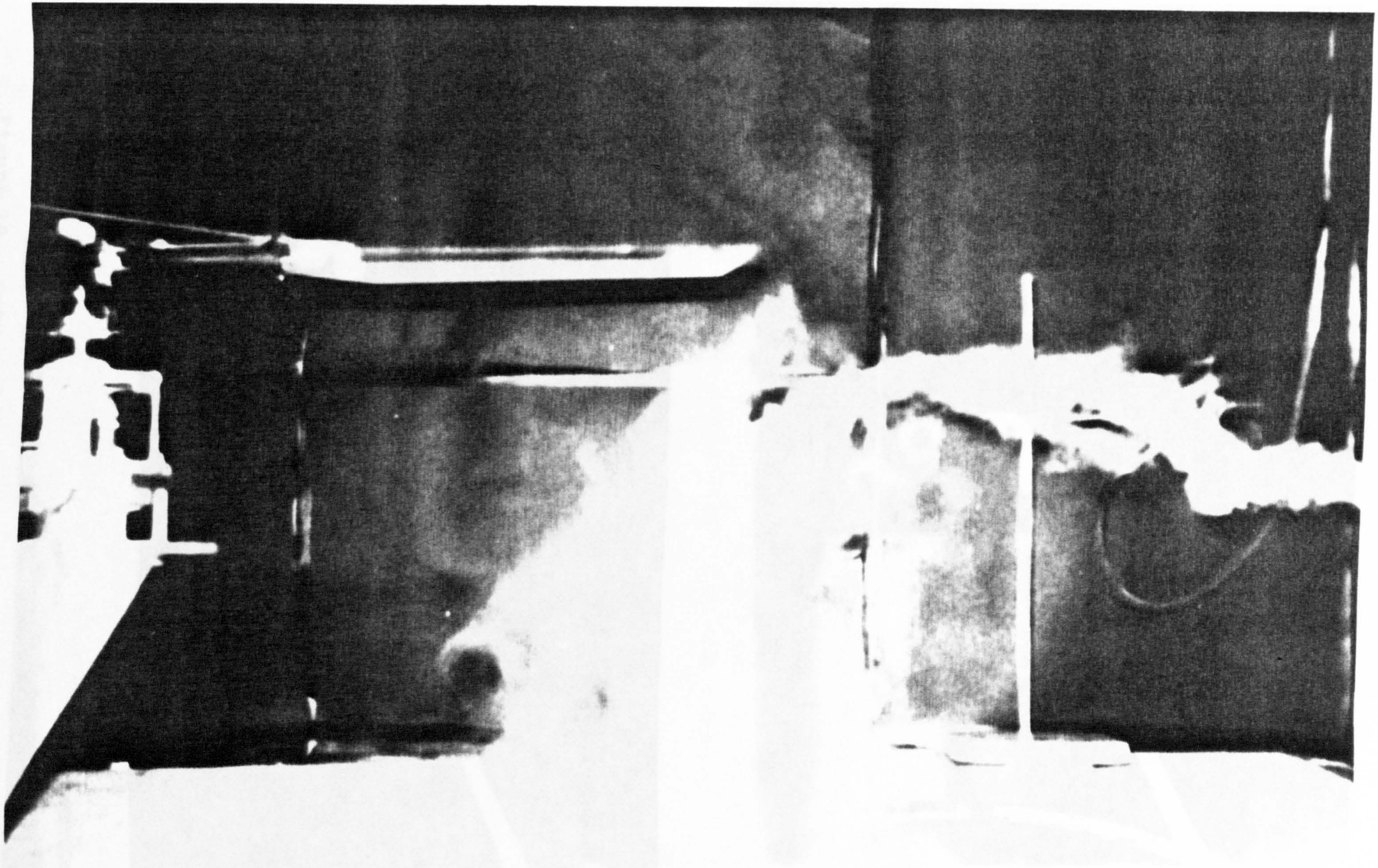

Figure 17 - Front boundary of the rotor wake at μ =0.063

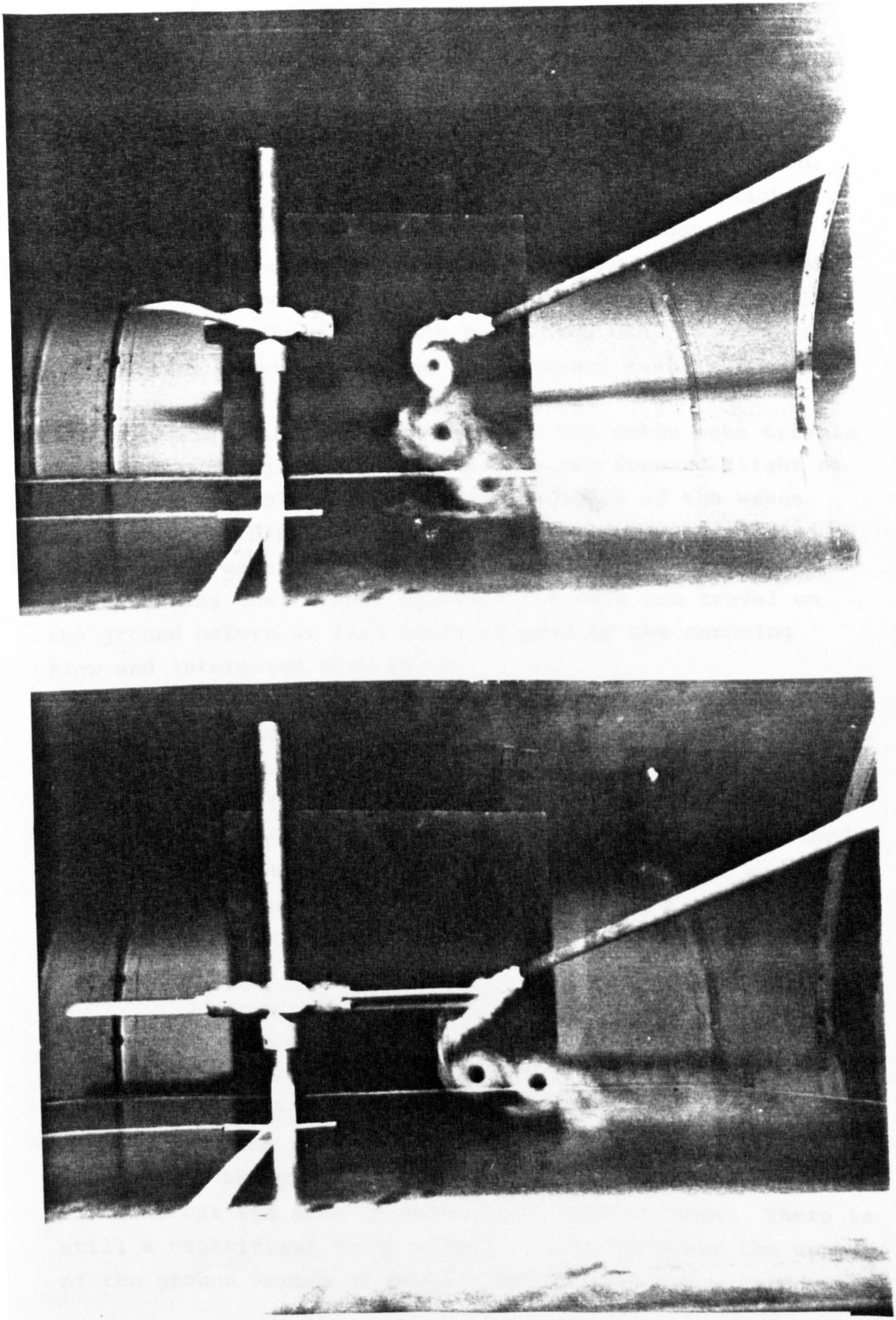

Figure 18 - Rotor wake in ground effect at hover

rotor wake is pushed by the oncoming flow. A fundamental difference observed between hover and forward flight is this location of the forward boundary of the rotor wake.

In hover, tip vortices are transported downward (although due to the wake contraction in the upper region, they come close to the rotor), whereas in forward flight the tip vortices travel inboard and slightly above the rotor and are then transported down through the rotor disk. Our rotor has three blades, so blade vortex intersection can occur more likely than the two bladed one. In case of blade vortex intersection the blade impact results in a diffusion of the concentrated vortex core.

Figs.(18) and (19) show how the rotor wake travels upstream on the ground for hover case and forward flight at advance ratio 0.079. The forward movements of the wakes were made possible by the extent of the impulses imparted to the rotor wake by the blade loading. The higher the blade loading the further upstream the wake can travel on the ground before at last being stopped by the oncoming flow and interacted with it.

As a result of this interaction process, the interaction boundary was created on the ground and the forward portion of the wake rolled up. In approaching the ground the wake first follows the skewed wake pattern until approximately 25% of rotor radius distance above the ground where the wake starts to expand gradually followed by moving upstream (some portion only) on the ground.

5.2.2 Ground Vortex

Figures (20) and (21) show the ground vortex for advance ratios 0.09 and 0.079 respectively. As we can see from Fig.(19) this vortex is generated by the rolling up of the front far wake portion of the rotor wake due to the interaction with the oncoming flow. The direction of rotation of the ground vortex is the same with the tip vortices but its size is about twice that of them. There is still a centrifugal force acting locally to clear the centre of the ground vortex of smoke. The size of the ground vortex

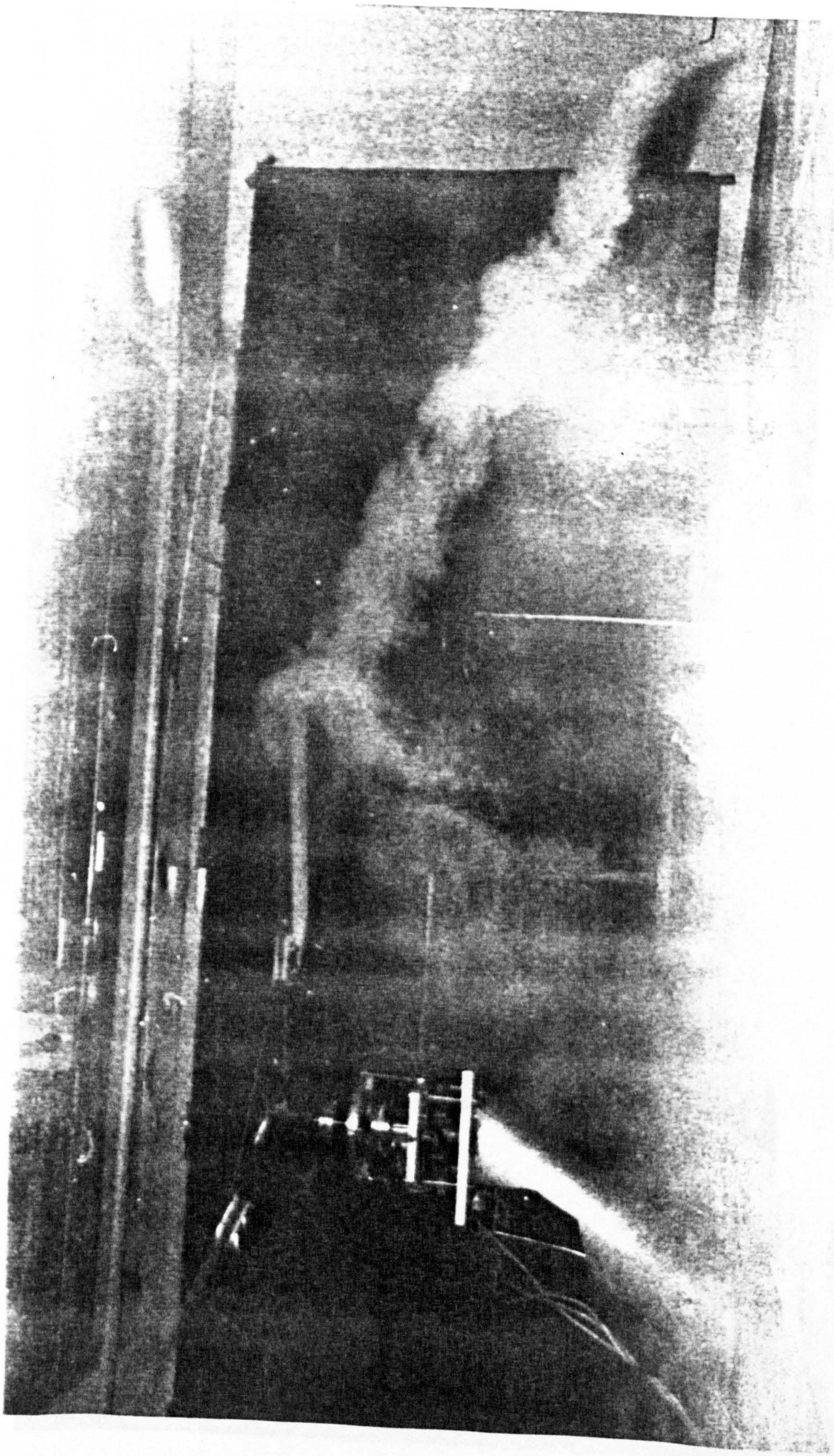

Figure 19 - Rotor wake in ground effect at μ =0.07

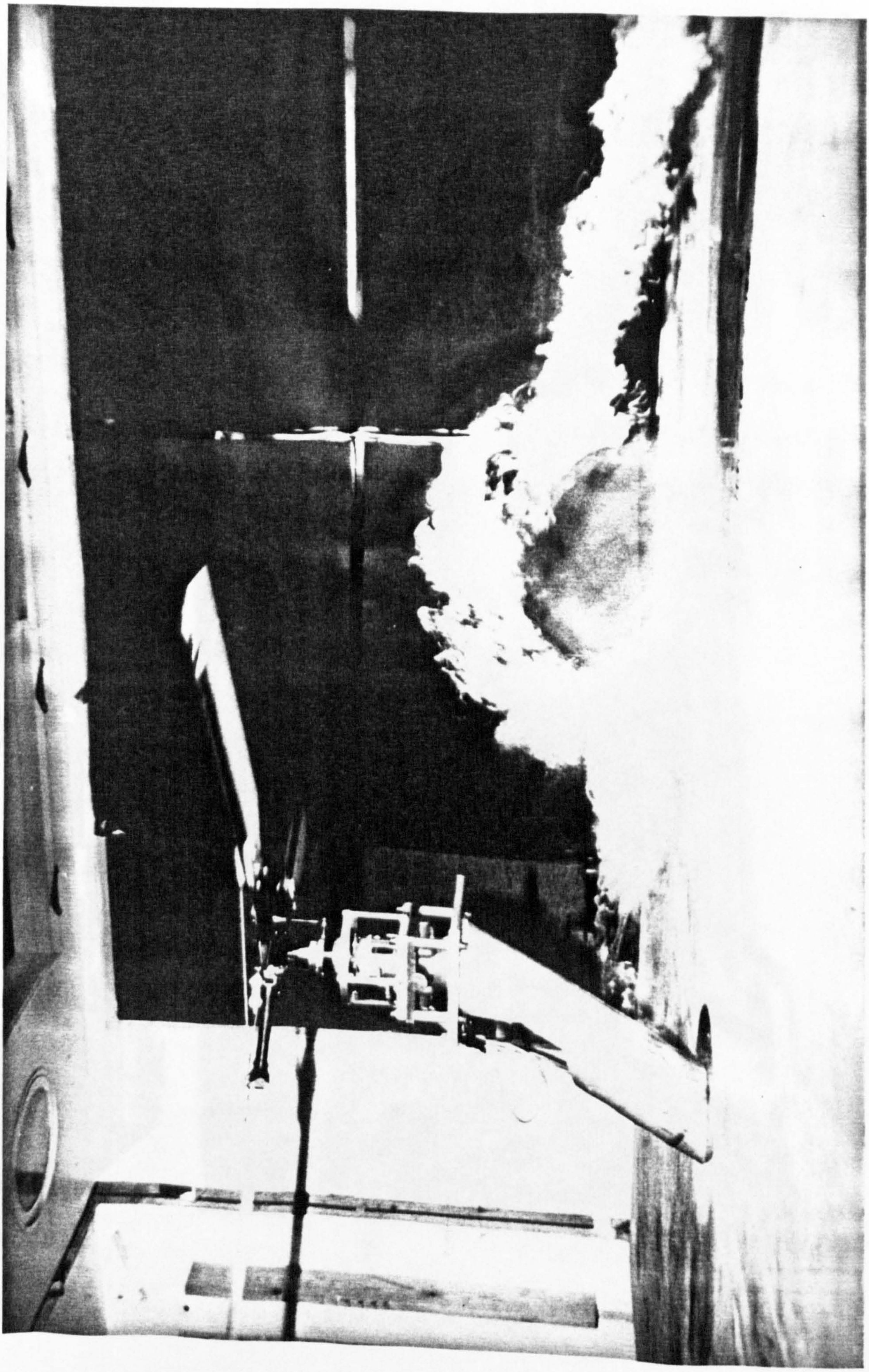

Figure 20 - Smoke picture of the ground vortex at $\mu = 0.090$

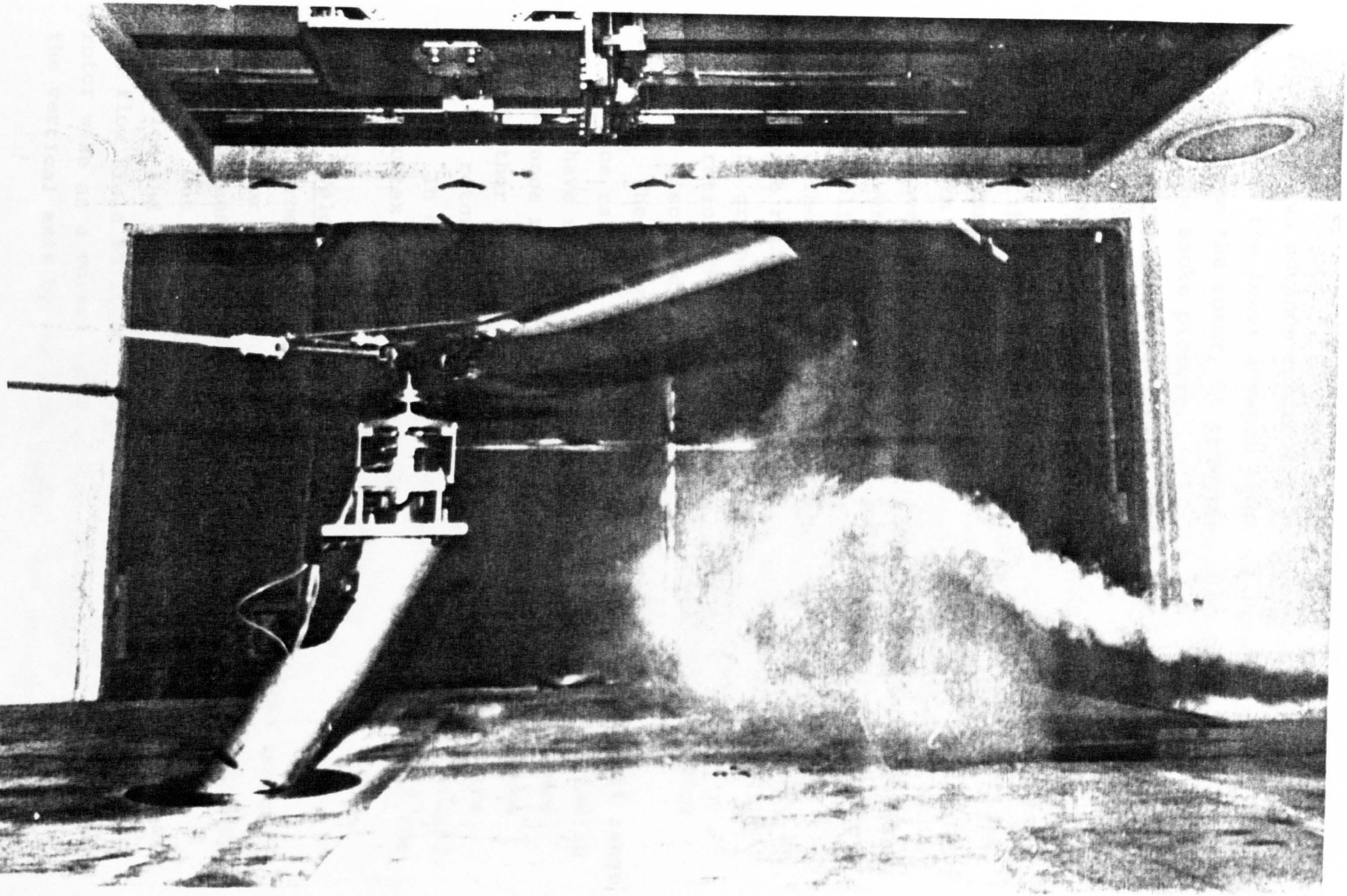

Figure 21 - Smoke picture of the ground vortex at μ =0.079

for these two advance ratios are almost constant, but since the wake at the lower advance ratio can travel further forward from the rotor, it underwent more diffusion as shown by the smoke picture.

From these results we can assume the generation of the ground vortex as follows:

The blades generate tip vortices and form the rotor wake. At a low advance ratio in ground effect, some portion of the wake can travel upstream and creates a kind of shearlayer. When the momentum of this wake is in balance with the oncoming flow, the vorticity contained in the wake have to concentrate into isolated vortices (rolling up of the wake). This rolled up wake encircles the rotor in a parabolic shape pattern.

The position of ground vortices are determined by the advance ratio (for a fixed pitch angle setting). The closer the ground vortex to the rotor (the higher the advance ratio) the more this vortex influences the rotor (will be discussed later).

The ground vortex is present for only a small range of advance ratios. Our preliminary experiments reported in Ref.(6) have shown that ground vortex strength increases with advance ratio up to a certain limit, then decreases with further increase of advance ratio and it disappears when the rotor wake has no more interaction with the ground.

In our experiments, for advance ratios > 0.12 the ground vortex is no longer present.

5.3 Velocity Measurements

From the two previous experiments we can imagine how the rotor wake in ground effect influences the velocity field underneath the rotor.

Out of ground effect, where there is no rotor wake expansion and no wake interaction with the oncoming flow, the flow field surrounding the rotor will only consider the rotor wake as a vortex cylinder moving downward inclined to the vertical axis by the skew angle. The measurement results

of the three components of velocity are combined and presented in Figures (23) to (52).

Since we are not able to present them in a single three dimensional picture, planar plottings have been used instead.

The velocity pictures are presented in two configurations as follows: (Figure.22).

- In the longitudinal plane of symmetry and planes parallel to it, the resultants of u (longitudinal component of velocity) and w (vertical component of velocity) were plotted.
- In the planes parallel to the ground or XOY plane, the resultants of u and v (lateral component of velocity) were plotted.

With this technique the complete velocity field can be illustrated.

The flow velocities vary from time to tome due to the rotation of the rotor which has a solidity ratio less than one. The three components of velocity are the results of time averaging.

5.3.1 Velocity Field Characteristics

To represent the velocity field underneath and surrounding the rotor we have chosen six planar plottings in the longitudinal plane of symmetry and planes parallel to it at y equals 0, -0.1, -0.2, -0.3, -0.4 and -0.5m, and three planar plottings in the planes parallel to the ground at z equals -0.08, -0.29 and -0.47m. (Figure 22). These vector plots provide pictorial representation of the velocity field there. These velocities were plotted with vector lengths scaled 1m/s equal to 0.1 inch and length dimensions scaled 0.01m equal to 0.1 inch, so that the magnitudes, directions and positions of the flow are depicted. Every vector shows the direction of the flow velocity and vector length shows the magnitude of the velocity measured at its tail.

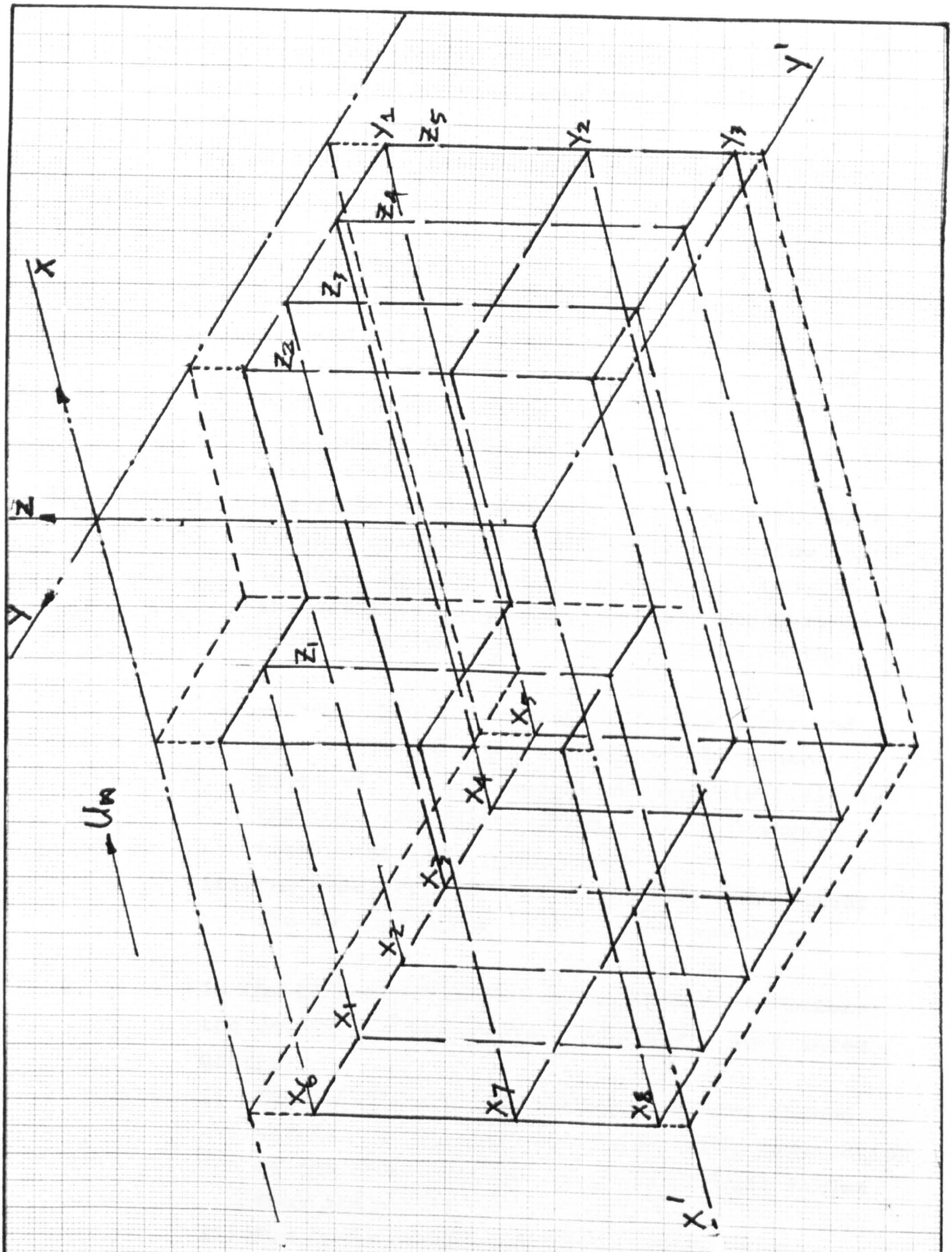

Figure 22 - Planar planes to represent the flow field

The front boundaries of the rotor wake were also drawn based on the smoke picture skew angle, to help interpret the flow field.

In general, the behaviour of the velocity field is as follows:

1. In the longitudinal plane of symmetry and planes parallel to it, the velocity field can be categorised into three groups:
   i) The field which is influenced by the ground vortex. Ground vortex induces its own velocity field which causes some redirection of the flow near to the vortex
   ii) The field which is dictated by the rotor wake. In this category are the inner wake flow which is shown by the jump in vector magnitude of the velocity as soon as the wake boundary is crossed and the shear layer created by the forward movement of the wake. Velocity vectors show the presence of this layer and were evaluated on the basis of the smoke pictures. This category of velocity field is the most unsteady since the rotor downwash totally dictates the nature.
   iii) The velocity field which is free from either the ground vortex or the rotor downwash.

2. In the planes parallel to the ground. As before the velocity field can be categorised into three groups:
   i) The field which is influenced by the ground vortex. At z equal to -0.27m, some redirection of the flow were caused by the ground vortex flow field.
   ii) The field inside the wake. Since there is some portion of the wake moving upstream on the ground, some flow is turned back to oppose the oncoming flow. This condition is shown by the

vector velocities in plane parallel to the ground at z equal to -0.47m.

iii) The field which is free from either the ground vortex or the rotor wake.

5.3.2 Effects of Ground Vortex

A ground vortex induces an upwash upstream of it, a downwash downstream of it and an inward flow on top of it, since its rotation direction is the same as that of the tip vortices. Refs.(1) and (6) indicate that ground vortex gains strength as it comes closer to the rotor. As a result, the closer the ground vortex to the rotor the more influence the rotor experiences from it. The induced upwash will try to oppose the rotor inflow velocity and reduce it, make the rotor work more efficiently with the same collective pitch angle setting and create a stronger wake locally. The induced downwash will redirect the flow downstream of it.

5.3.3 Effects of Advance Ratios

We have grouped the vector velocities plottings to account for the effect of advance ratios for the same collective pitch angle testing, starting from the highest one which is 0.09 in Figs.(23) to (31), followed by 0.079 in Figs.(32) to (40) and the lowest 0.063 in Figs.(41) to (46).

A higher advance ratio means a higher oncoming flow velocity and a higher wake skew angle. The velocity vectors show:

a. The change of vectors' magnitude with the increase of advance ratio.

b. The higher the advance ratio the closer the ground vortex to the rotor and the greater the influence from the ground vortex on the flow field underneath and surrounding the rotor. For instance at advance ratio 0.063 where the ground vortex position is far upstream from the rotor (indicated by the position of the interaction boundary only; the smoke picture could not visualise boundary only;

the smoke picture could not visualise it due to the extent the far wake underwent viscous diffusion). There seems little change in the flow behaviour approaching the rotor wake. At advance ratio 0.09, the influence of the ground vortex has altered the flow field quite considerably. The induced upwash from the ground vortex reached the rotor and reduced the inflow velocity to create a higher effective incidence angle locally.

5.3.4 Effects from the Ground

All velocity vectors inside the upper wake show that the magnitude of the vertical component of velocity (w) is smaller than what they should be in creating the wake skew angle χ ($w = -U_\infty ctg\chi$). This is the result of the ground induced upwash opposing the w component inside the wake. Ref.8 indicates that the greater the thrust produced by the rotor, the stronger the effect from the ground experienced by it.

In our experiments, the first collective pitch angle setting was 16 degrees which created a high thrust coefficient and it is understandable that the rotor experienced a strong upwash from the ground.

With the reduction of the w component of velocity inside the wake, the rotor can produce more thrust in ground effect than in the free air for a given collective pitch angle setting. The other effect from the ground shown by the velocity vectors is the deceleration of the flow in approaching the rotor wake. This is due to the upstream flow induced by the ground which can be considered as a result of the interaction between the original rotor flow field and the image rotor flow field which represents the ground. In this situation the image rotor produces an upstream flow opposing the oncoming flow and reduce its velocity. Thrust measurement results in Fig.(14) show how the thrust produced by the rotor varied with the oncoming flow velocity.

In the case of hover, the thrust was the highest and then decreased with the increase of the oncoming flow

velocity until at last it levelled out.

Following our preliminary result in Ref.(6) has shown that the ground effect decreases with forward flight, the increment of thrust produced above the level value results from the ground effect.

The combination of all the results about ground effect from smoke pirctures, thrust measurements and rotor velocity fields indicate that a rotor operating in ground effect can be seen to produce an air cushion on the ground which creates an enhancement on the lifting capability of the rotor and make it more efficiently usable. The thickness of this air cushion depends on the magnitude of the wake skew angle since the greater the angle the less portion of the mass of air that can move upstream with the wake on the ground. For instance at advance ratio 0.090 with skew angle 56.5 degrees, the thickness of the portion of flow moving upstream is less than at advance ratio 0.063 with skew angle of 37 degrees.

Rotor wake in ground effect can be approximated in Fig.(47).

5.3.5 Comparison with the Theoretical Model

Figures (48) to (53) are the computational results of velocity vectors in Figs.(23), (25), (32), (34), (41) and (43), based on Heyson's vortex cylinder model. There are some discrepancies between these two although some are in reasonable agreement. The weaknesses of the theoretical model are:

1. The theoretical model did not include the momentum of flow produced by the rotor and the energy imparted by the blades on the flow passing through them. As a result the forward movement of some portion of the blade could not be predicted and the wake which was assumed as being a vortex cylinder would only expand on the ground slightly and create a vortex immediately upstream of the wake.
2. The ground vortex which results from a viscous interaction is out of this inviscid solution scope.
3. We have assumed in the computational model that the blade loading is uniform along the blades and there is

no effect from the root vortex. By doing so we have ignored the trailed vorticity shed by the rotor. As a result there are differences between measurements and flow model for the flow inside the rotor wake.

5.3.6 Effects of Collective Pitch Angle Settings

Figures (54) and (55) are the velocity vectors of Figs.(23) and (32), but with collective pitch angle of 10 degrees. These figures show that collective pitch angle determines the position of the ground vortex and the wake skew angle. For the same advance ratio the ground vortex is closer to the rotor and the wake skew angle is greater for the low pitch angle than when the setting is higher. From the vector plottings, the ground vortex is smaller and weaker for the low pitch angle which implies no influence on the rotor performance. This result supports previous discussion in 5.3.4.

6. Concluding Remarks

This work presents experimental and analytical techniques which can be used to improve the understanding of the aerodynamics of low speed helicopter flight in ground effect. Flow visualisation techniques are useful in identifying rotor wake geometry, ground vortex, the interaction boundary on the ground and the interpretation of flow velocity data.

As a result of this work, it can be concluded that:

1. The velocity field of a rotor moving forward at low speeds in ground effect is strongly influenced by the ground vortex generated by the interaction of the rotor wake, the ground and the oncoming flow. The ground vortex induces a velocity field whose influence depends on advance ratios of the rotor and rotor collective pitch angle. When the ground vortex is close to the rotor the induced upwash from this vortex can reach the rotor and reduce the inflow velocity and make the rotor work more efficiently.

2. With the decrease in thrust produced by the rotor in ground effect as it changes the course from hover to forward flight, there is a need to increase the collective pitch angle to retain the height which has been obtained in hover. This implies that there is an increase of power to change from hover to forward flight

3. Rotor wake in ground effect can be explained as follows: The rotor wake first moves downward and rearward in almost a cylinder shape, then starts expanding as the ground is approached. There will be a forward movement of some portion of the wake if the momentum initiated by the rotor is not fully swept rearward and manages to push the wake forward. The deciding factor of this forward movement is the wake skew angle and the height above the ground.

4. Our results demonstrate that for a given height, increasing the collective pitch angle clearly increases the ground effect and the influence of the ground vortex on the flow field.

5. In general, the ground effect decreases the oncoming flow velocity and vertical component of velocity inside the wake which improves the rotor performance.

6. We have learned during the experiments that it is difficult to produce reliable measurement results in this three dimensional flow with embedded vortices and reverse flow regions by introducing a hot wire anemometer probe, without relying on other techniques such as flow visualisation. It is therefore necessary that in the future, quantitative measurements of this type of flow be made with optical techniques such as laser velocimeter or laser particle tracing which are completely non-intrusive to the flow and reliable on their own.

7. From the comparison between the experiment results and computation model there is a need to improve the analytical model by taking into account the momentum produced by the rotor and viscous interaction.

REFERENCES

1. P.F.SHERIDAN & W.WIESNER
Aerodynamics of Helicopter Flight Near the Ground
Preprint No.77.3-04,AHS Forum 1977

2. H.H.HEYSON
Theoretical Study of Conditions Limiting V/STOL Testing in Wind Tunnel with Solid Floors
NASA TN D-5819, 1970

3. H.H.HEYSON
Equations for the Induced Velocities near a Lifting Rotor with Nonuniform Azimuthwise Vorticity Distribution.
NASA TN D-394, 1960.

4. W.WIESNER AND G.KOHLER
Tail Rotor Performance in Presence of Main Rotor, Ground and Winds
A.H.S.Journal Vol.19, No.3, 1974.

5. F.A.DuWALDT
Wakes of Lifting Propellers in Ground Effect
Cornell Aeronautical Laboratory, Report CAL CAL BB-1665-S-3, 1966.

6. E.A.BOYD and I.KUSMARWANTO
Ground Effect on a Rotor Wake
C of A Report 8323, 1983.

7. H.H.HEYSON
Theoretical Study of the Effect of Ground Proximity on the Induced Efficiency of Helicopters Rotors.
NASA TM-X-71951, 1977.

8. H.C.CURTISS,Jr.,W.F.PUTMAN AND E.J.HANKER,Jr.
Rotor Aerodynamics in Ground Effect at Low Advance Ratio.
Princeton University Report No.1571-MAE,1982

9. J.L.JENKINS,Jr.
Trim Requirements and Static Stability Derivatives from a Wind Tunnel Investigation of a Lifting Rotor in Transition.
NASA TN D-2655, 1965.

10. F.H.SCHMITZ and C.R.VAUSE
Near Optimal Take Off Policy for Heavily Loaded Helicopters Exiting from Confined Areas.
J.Aircraft, May, 1976.

11. W.H.RAE
Limits on Minimum-Speed V/STOL Wind Tunnel Tests.
J.Aircraft, May-June, 1967.

12. L.F.EAST
The Measurement of Ground Effect using a Fixed Ground Board in a Wind Tunnel
A.R.C.Report R & M No.3689.

13. H.H.HEYSON
Linearised Theory of Wind Tunnel Jet-Boundary Corrections and Ground Effect for V/STOL Aircraft
NASA TR R-124, 1962

14. H.H.HEYSON
A Note on the Mean Value of Induced Velocity for a Helicopter Rotor.
NASA TN D-240, 1960.

15. DISA TRIAXIAL PROBE
DISA, June 1971.

16. A.GESSOW and G.C.MYERS,Jr.
Aerodynamics of the Helicopter
Frederick Ungar Publishing Co., 7th Ed.1978.

17. B.O.PEIRCE
A Short Table of Integrals
Ginn and Co., 1929.

18. J.L.TANGLER, R.M.WOHFIELD and S.J.MILEY
An Experimental Investigation of Vortex Stability,
Tip Shapes, Compressibility and Noise for
Hovering Model Rotors.
NASA CR-2305, 1973.

19. A.J.LANG REBE and T.A.EGOLT
Rotorcraft Wake Analysis for the Prediction of
Induced Velocities
A.H.S.Forum Proceedings, 1975.

20. A.R.MILLER
BASIC Program for Scientists and Engineers
SYBEX, 1981.

21 M.R.DAVIS
Design of Flat Plate Leading Edges to avoid
Flow Separation
A.I.A.A.Journal, May, 1980.

BIBLIOGRAPHY

1. W.JOHNSON
Helicopter Theory
Princeton University Press, 1980.

2. H.H.HEYSON
Operational Implications of some NACA/NASA Rotary Wing Induced Velocity Studies.
NASA TM-80232, 1980

3. R.B.GRAY
Experimental Smoke and Electromagnetic Analog Study of Induced Flow Field about a Model Rotor in Steady Flight within Ground Effect
NASA TN D-458, 1960.

4. A.R.S.BRAMWELL
Helicopter Dynamics
Edward Arnold Publishers, 1976.

5. E.A.FRADENBURGH
The Helicopter as a Ground Effect Machine
The Princeton University Conference - Symposium on Ground Effect Phenomena, 1959.

6. H.C.CURTISS,Jr., MAO SUN and E.J.HANKER
Dynamic Phenomena in Ground Effect
AHS Forum, Paper No. A-83-39-76-0000, 1983

7. P.CRIMI
Theoretical Prediction of the Flow in the Wake of Helicopter Rotor.
Cornell Aeronautical Laboratory Report
BB-1994-S-1, 1965.

8. C.TUNG, S.L.PUCCI, F.X.CARADONNA and H.A.MORSE
The Structure of Trailing Vortices generated by Model Rotor Blades.
Vertica Vol.7, No.1, 1983.

9. K.R.REDDY
Calculations of the Aerodynamic Flow Field in the Vicinity of a Sea King Helicopter
ARL-AERO-REPORT-158, 1983.

10. A.F.LEHMAN
Model Studies of Helicopter Rotor Flow Patterns in a Water Tunnel
AHS Forum, Paper No. 207, 1968.

11. R.W.EMPEY and R.A.ORMISTON
Tail Rotor Thrust on a 5.5foot Helicopter Model in Ground Effect.
AHS Forum, Preprint No.802, 1974.

12. T.A.EGOLT and A.J.LANDGREBE
Helicopter Rotor Wake Geometry and its Influence in Forward Flight.
NASA CR-3726, 1983

13. A.J.LANDGREBE and B.V.JOHNSON
Measurement of Model Helicopter Rotor Flow Velocities with a Laser Doppler Velocimeter
A.H.S.Journal, July, 1974.

14. H.H.HEYSON
A Brief Survey of Rotary Wing Induced Velocity Theory
NASA TM 78741, 1978

15. R.J.GOLDSTEIN
Fluid Mechanics Measurements
Hemisphere Publishing Corporation, 1983

16. A.E.PERRY
Hot Wire Anemometry
Clarendon Press, Oxford, 1982

17. O.O.MOJOLA
Measurements in a Turbulent Horseshoe Vortex and the Problem of Probe Interference
I.C.Aero Report 73-08, 1973.

APPENDIX A

I. Blade Circulation

The blade circulation for our model is assumed to be constant along the radius, but may vary azimuthwise according to:

$$\Gamma = \Gamma_0 - \Gamma_1 \sin\psi \qquad \text{(Ref.14)} \qquad (1)$$

ψ = azimuth angle evaluated anticlockwise

Ω = rotor angular velocity clockwise

Since

$$dT = \rho U_T \Gamma_{dr}$$

$$= \frac{b}{2\pi}\rho(\Omega r - \mu\Omega R\sin\psi)(\Gamma_0 - \Gamma_1\sin\psi)\,dr\,d\psi$$

(μ is the rotor advance ratio)

then the rotor thrust T is:

$$T = \frac{b}{2\pi}\int_0^{2\pi}\int_0^{R}(\Omega\Gamma_0 r - \mu\Gamma_0\Omega R\sin\psi - \Gamma_1\sin\psi\,\Omega r + \mu\Gamma_1\Omega R^2\sin^{-2}\psi)\,dr\,d\psi$$

which yields

$$T = \frac{b\rho\Omega R^2}{2}(\Gamma_0 + \mu\Gamma_1) \qquad (2)$$

The thrust moment M_T is T x r

$$M_T = \int_0^R \rho(\Omega r - \mu\Omega R\sin\psi)(\Gamma_0 - \Gamma_1\sin\psi)\,r\,dr$$

$$= \rho\Omega R^3\left[\frac{\Gamma_0}{3} - \left(\frac{\Gamma_1}{3} + \frac{\mu\Gamma_0}{2}\right)\sin\psi + \frac{\mu}{2}\Gamma_1\sin^{-2}\psi\right] \qquad (3)$$

The thrust moment M_T is independent of the azimuth angle ψ if only first harmonic flapping is considered. Ref.(16). (in fact experimentally all harmonics above the second have been found to be small).

Thus the first harmonic of the thrust moment must be zero.

From equation (3) $\frac{\Gamma_1}{3} + \frac{\mu}{2}\Gamma_0 = 0$

$$\Gamma_1 = -\frac{3}{2}\mu\,\Gamma_0$$

Equation (1) becomes

$$\Gamma = \Gamma_0(1 + 1.5\mu \sin\psi)$$

II Induced Velocities of the rotor wake in free air

We have assumed in our theoretical model that there are no effects from the root vortices and the radial component of vorticity. As a result, only the outer wake which induces velocity field superimposed on the free stream flow. The velocity field can be found by integrating the Biot Savart law over the entire outer cylinder wake (Ref.14).

If P(x,y,z) is a point in the flow field, then:

$$d\bar{q}_p = \frac{1}{4\pi}\frac{d\Gamma}{dL}\frac{d\bar{s} \times \bar{a}}{|a|^3} dL \qquad (4)$$

From Fig.9 these following quantities can be evaluated by inspection:

$$\bar{s} = \bar{i}(R\cos\psi + L\sin\chi) + \bar{j}(R\sin\psi) + \bar{k}(-L\cos\chi)$$

$$d\bar{s} = \left[\bar{i}(-R\sin\psi) + \bar{j}(R\cos\psi) + \bar{k}(0)\right]d\psi$$

$$\bar{a} = \bar{i}(R\cos\psi + L\sin\chi - x) + \bar{j}(R\sin\psi - y) + \bar{k}(-L\cos\chi - z)$$

Substituting these quantities into equation (4) and integrating yields:

$$\bar{q}_p = \frac{R}{4\pi}\int_0^{2\pi}\int_0^{\infty}\frac{d\Gamma}{dL}\frac{\begin{vmatrix} \bar{i} & \bar{j} & \bar{k} \\ -\sin\psi & \cos\psi & 0 \\ (R\cos\psi+L\sin\chi-x) & (R\sin\psi-y) & (-L\cos\chi-z) \end{vmatrix} dLd\psi}{\left[(R\cos\psi+L\sin\chi-x)^2 + (R\sin\psi-y)^2 + (-L\cos\chi-z)^2\right]^{\frac{3}{2}}} \qquad (5)$$

Vertical component (w)

The vertical ($\bar{k}$) component of induced velocity is, from equation (5)

$$w = \frac{R}{4\pi}\int_0^{2\pi}\int_0^{\infty}\frac{d\Gamma}{dL}\frac{(x\cos\psi+y\sin\psi-R-L\sin\chi\cos\psi)dLd\psi}{\left[R^2+x^2+y^2+z^2-2R(x\cos\psi+y\sin\psi)+2L(z\cos\chi-x\sin\chi+R\sin\chi\cos\psi)+L^2\right]^{\frac{3}{2}}} \qquad (6)$$

This integration with respect to L may be accomplished with the solutions of Ref.(17) which are as follows:

Let $A = a + bx + cx^2$ and $q = 4ac - b^2$

Then $\int\frac{dx}{A\sqrt{A}} = \frac{2(2cx+b)}{q\sqrt{A}}$

$\int\frac{xdx}{A\sqrt{A}} = \frac{-2(bx+2a)}{q\sqrt{A}}$

$\Big\}\ \int\frac{(x+1)dk}{A\sqrt{A}} = \frac{2\left[(2c-b)x + (b-2a)\right]}{q\sqrt{A}}$

$$\int_0^{\infty} \frac{(E-Gx)\,dx}{A\sqrt{A}} = \left| \frac{2\left[E(2c+b)+G(bx+2a)\right]}{(4ae-b^2)\sqrt{a+bx+cx^2}} \right|_0^{\infty} \qquad (7)$$

where in our case:

$a = (R^2+x^2+y^2+z^2-2R(x\cos\psi+y\sin\psi))$

$b = 2(z\cos\chi-x\sin\chi+R\sin\chi\cos\psi) = 2F$

$c = 1$

$E = x\cos\psi + y\sin\psi - R$

$G = \sin\chi\cos\psi$

Substituting limits we get from equation (7):

$$\frac{(4Ec+2Gb)}{(4ac-b^2)\sqrt{c}} - \frac{(2Eb+4Ga)}{(4ac-b^2)\sqrt{a}}$$ substituting $c = 1$ and $b = 2F$ yields:

$$\frac{(4E+4GF)\sqrt{a} - (4EF+4Ga)}{(4a-4F^2)\sqrt{a}} = \frac{E-G\sqrt{a}}{(\sqrt{a}+F)\sqrt{a}} \qquad (8)$$

Combining terms reduces equation (6) to:

$$w = \frac{R}{4\pi}\int_0^{2\pi} \frac{d\Gamma}{dL} \frac{(x\cos\psi+y\sin\psi-R-\sin\chi\cos\psi\sqrt{R^2+x^2+y^2+z^2-2R(x\cos\psi+y\sin\psi)}\;d\psi}{\{(\sqrt{R^2+x^2+y^2+z^2-2R(x\cos\psi+y\sin\psi)}+(z\cos\chi-x\sin\chi+R\sin\chi\cos\psi))\sqrt{R^2+x^2+y^2+z^2-2R(x\cos\psi y\sin\psi)}\}} \qquad (9)$$

Noting that $R_c = \sqrt{R^2+x^2+y^2+z^2-2R(x\cos\psi+y\sin\psi)}$, equation (9) becomes:

$$w = -\frac{R}{4\pi}\int_0^{2\pi}\frac{d\Gamma}{dL}\frac{(R + R_c(\sin\chi\cos\psi)-x\cos\psi - y\sin\psi)}{[R_c(R_c+z\cos\chi-x\sin\chi+R\sin\chi\cos\psi)]}\,d\psi$$

$$= -\frac{1}{4\pi}\int_0^{2\pi}\frac{d\Gamma_0(1+1.5\mu\sin\psi)}{dL}\frac{(1+\frac{R_c}{R}(\sin\chi\cos\psi)-\frac{x}{R}\cos\psi-\frac{y}{R}\sin\psi)}{[\frac{R_c}{R}(\frac{R_c}{R}+\frac{z}{R}\cos\chi-\frac{x}{R}\sin\chi+\sin\chi\cos\psi)]}\,d\psi \qquad (10)$$

At the centre of the rotor where x, y and z = 0

$$w_o = -\frac{1}{4\pi}\frac{d\Gamma_0}{dL}2\pi \qquad \text{or} \qquad \frac{d\Gamma_0}{dL} = -2w_o$$

Since $\frac{U_\infty}{w_o} = -\tan\chi$, then $\frac{d\Gamma}{dL} = 2U_\infty ctg\chi(1+1.5\mu\sin\psi)$

so that finally:

$$w = -\frac{U_\infty ctg\chi}{2\pi}\int_0^{2\pi}\frac{(1+1.5\mu\sin\psi)(1+\frac{R_c}{R}(\sin\chi\cos\psi)-\frac{x}{R}\cos\psi-\frac{y}{R}\sin\psi)d\psi}{[\frac{R_c}{R}(\frac{R_c}{R}+\frac{z}{R}\cos\chi-\frac{x}{R}\sin\chi+\sin\chi\cos\psi)]} \qquad (11)$$

Longitudinal component (u)

The longitudinal ($\bar{i}$) component of the induced velocity, from equation (8) is:

$$u = \frac{R}{4\pi}\int_0^{2\pi}\int_0^{\infty}\frac{d\Gamma}{dL}\frac{-(z + L\cos\chi)\cos\psi \quad dLd\psi}{[R^2+x^2+y^2+z^2-2R(x\cos\psi+y\sin\psi)+2L(z\cos\chi-x\sin\chi+R\sin\chi\cos\psi)+L^2]^{\frac{3}{2}}} \qquad (12)$$

Since the denominator is the same as in the w component evaluation, we can apply the equation (7) and (8) with G = $\cos\chi\cos\psi$ and E = z $\cos\psi$

Noting that:

$$R_c = \sqrt{R^2 + x^2 + y^2 + z^2 - 2R(x\cos\psi + y\sin\psi)}$$

$$\frac{d\Gamma}{dL} = 2U_\infty \text{ ctg } \chi(1+1.5\mu\sin\psi)$$

The final result is:

$$u = -\frac{U_\infty \text{ctg}}{2\pi} \int_0^{2\pi} (1+1.5\mu\sin\psi) \frac{(\frac{z}{R} + \frac{R_c}{R}\cos\chi)\cos\psi \quad d\psi}{\left[\frac{R_c}{R}(\frac{R_c}{R} + (\cos\psi - \frac{x}{R})\sin\chi + \frac{z}{R}\cos\chi)\right]} \tag{13}$$

Lateral component (v)

The lateral ($\bar{j}$) component of the induced velocity from equation (5) is:

$$v = \frac{R}{4\pi} \int_0^{2\pi} \int_0^{\infty} \frac{d\Gamma}{dL} \frac{-(z + L\cos\chi)\sin\psi \, dL d\psi}{\left[R^2+x^2+y^2+z^2-2R(x\cos\psi+y\sin\psi)+2L(z\cos\chi-x\sin\chi+R\sin\chi\cos\psi)+L^2\right]^{\frac{3}{2}}} \tag{14}$$

It is apparent that equation (14) differs from equation (12) only by a factor in the numerator ($\cos\psi$ and $\sin\psi$), which does not effect the integration with respect to L. Thus, the final expression for the lateral component of induced velocity in comparison with equation (13) may be written immediately as:

$$v = -\frac{U_\infty \text{ctg}\chi}{2\pi} \int_0^{2\pi} (1+1.5\mu\sin\psi) \frac{(\frac{z}{R} + \frac{R_c}{R}\cos\chi) \sin\psi \, d\psi}{\left[\frac{R_c}{R}(\frac{R_c}{R} + (\cos\psi - \frac{x}{R})\sin\chi + \frac{z}{R}\cos\chi)\right]} \tag{15}$$

Discussion

It will be observed that the equations for the three components of induced velocity of a rotor wake in free air (eqns.(13), (15), and (12)) have been left in the form of integrals with respect to ψ. It appears that these integrals cannot be solved analytically, however results can be obtained by numerical integration.

Appendix B

Calculations of velocity vectors from a three-element hot wire anemometer signals

The linearised anemometer signals from a three-wire probe can be assumed to correspond with the relationship between the output voltage signals and the velocities in the direction of the three wires as: (Ref.15).

$$V_x^2 = s^2(k_1^2 x^2 + y^2 + k_2^2 z^2)$$

$$V_y^2 = s^2(k_2^2 x^2 + k_1^2 y^2 + z^2) \qquad (1)$$

$$v_z^2 = s^2(x^2 + k_2^2 y^2 + k_1^2 z^2)$$

where:

V_x, V_y and V_z	are the linearised anemometer signals
x, y, z	are velocities in the direction of the three wires
s	is signal sensitivity (which must be equal for the three linearised signals)
k_1	is the correction term for the tangential cooling effect. The mean value is 0.15.
k_2	is the correction term for the pitch angle influence. The mean value is 1.02.

Substituting the values of k_1 and k_2 in equation (1) and solving the equation with respect to x, y and z, we get:

$$\begin{vmatrix} x^2 \\ y^2 \\ z^2 \end{vmatrix} = \frac{1}{s^2} \begin{vmatrix} k_1^2 & 1 & k_2^2 \\ k_2^2 & k_1^2 & 1 \\ 1 & k_2^2 & k_1^2 \end{vmatrix}^{-1} \begin{vmatrix} V_x{}^2 \\ V_y{}^2 \\ V_z{}^2 \end{vmatrix}$$

$$= \frac{1}{s^2} \begin{vmatrix} -0.506 & 0.515 & 0.475 \\ 0.475 & -0.506 & 0.515 \\ 0.515 & 0.475 & -0.506 \end{vmatrix} \begin{vmatrix} V_x{}^2 \\ V_y{}^2 \\ V_z{}^2 \end{vmatrix} \qquad (1)$$

Coordinate transformation

The velocity components in the wire system may be transformed into another coordinate system with a fixed orientation with respect to the probe.

In our experiments, we assumed the dominant velocity to be the u component of velocity of the flow field and also the U_∞ tunnel free stream velocity. We aligned the probe axis as the u axis, the v axis and w axis in the horizontal and vertical plane respectively with the z wire lying in the vertical plane defined by u and w (Fig.11). From this figure, to transform the wire coordinate system into the rotor coordinate system, we have to yaw the system through the angle of 45^o and then pitching it up through the angle of 35.3^o. The transformation yields:

$$\begin{vmatrix} u \\ v \\ w \end{vmatrix} = \begin{vmatrix} & B & \end{vmatrix} \begin{vmatrix} x \\ y \\ z \end{vmatrix}$$

where B from Fig.(11) is:

$$B = \begin{vmatrix} \cos45\cos35.3 & \sin45\cos35.3 & \sin35.3 \\ -\sin45 & \cos45 & 0 \\ -\cos45\sin35.3 & -\cos45\sin35.3 & \cos35.3 \end{vmatrix} \quad (2)$$

Combining equations (1) and (2) yields:

$$\begin{vmatrix} u \\ v \\ w \end{vmatrix} = \frac{1}{s} \begin{vmatrix} B \end{vmatrix} \begin{vmatrix} A \end{vmatrix}$$

where A is:

$$\sqrt{-0.506V_x^2 + 0.515V_y^2 + 0.475V_z^2}$$

$$A = \sqrt{0.475V_x^2 - 0.506V_y^2 + 0.515V_z^2}$$

$$\sqrt{0.515V_x^2 + 0.475V_y^2 - 0.506V_z^2}$$

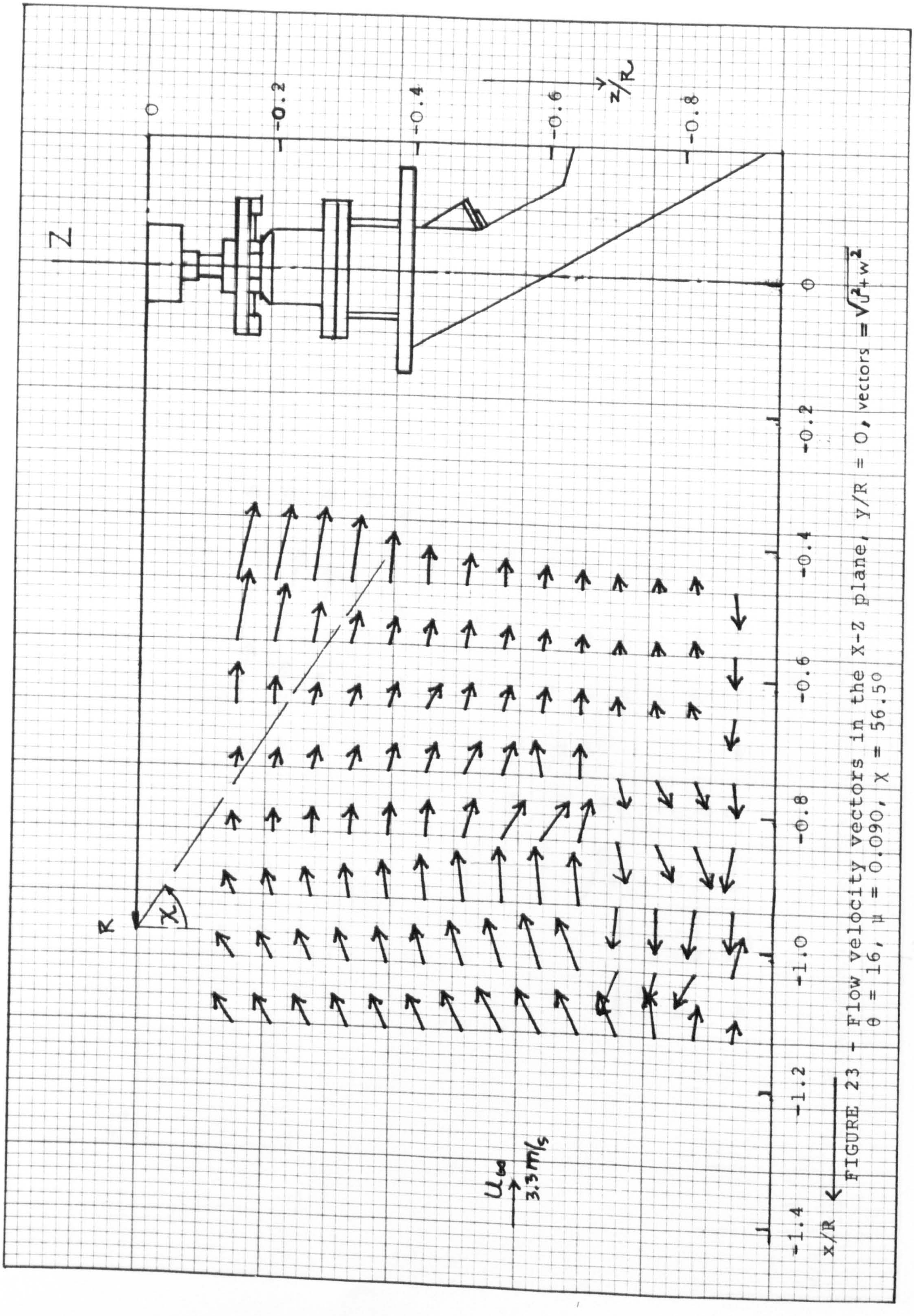

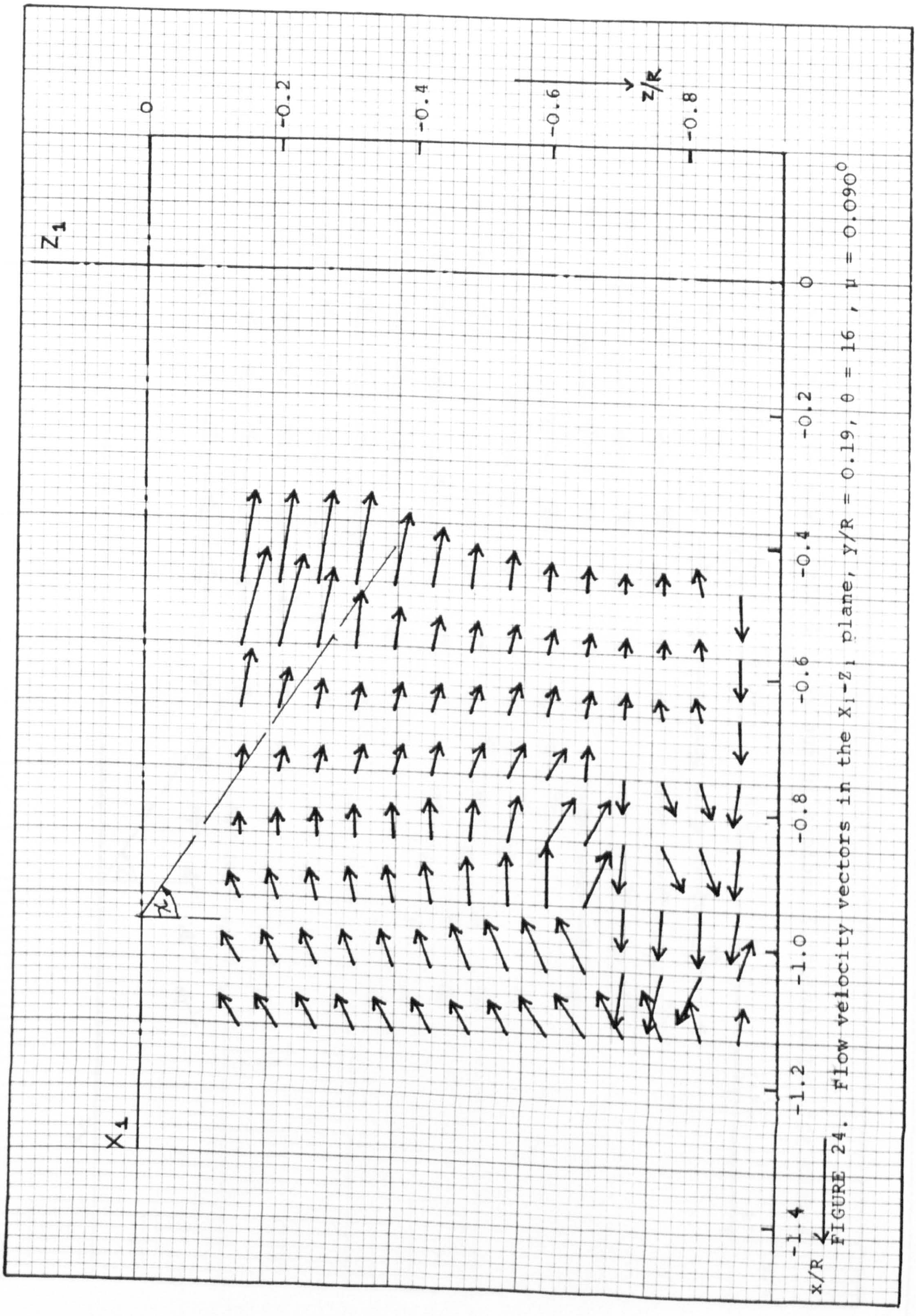

FIGURE 24. Flow velocity vectors in the X_1-Z_1 plane, Y/R = 0.19, θ = 16°,

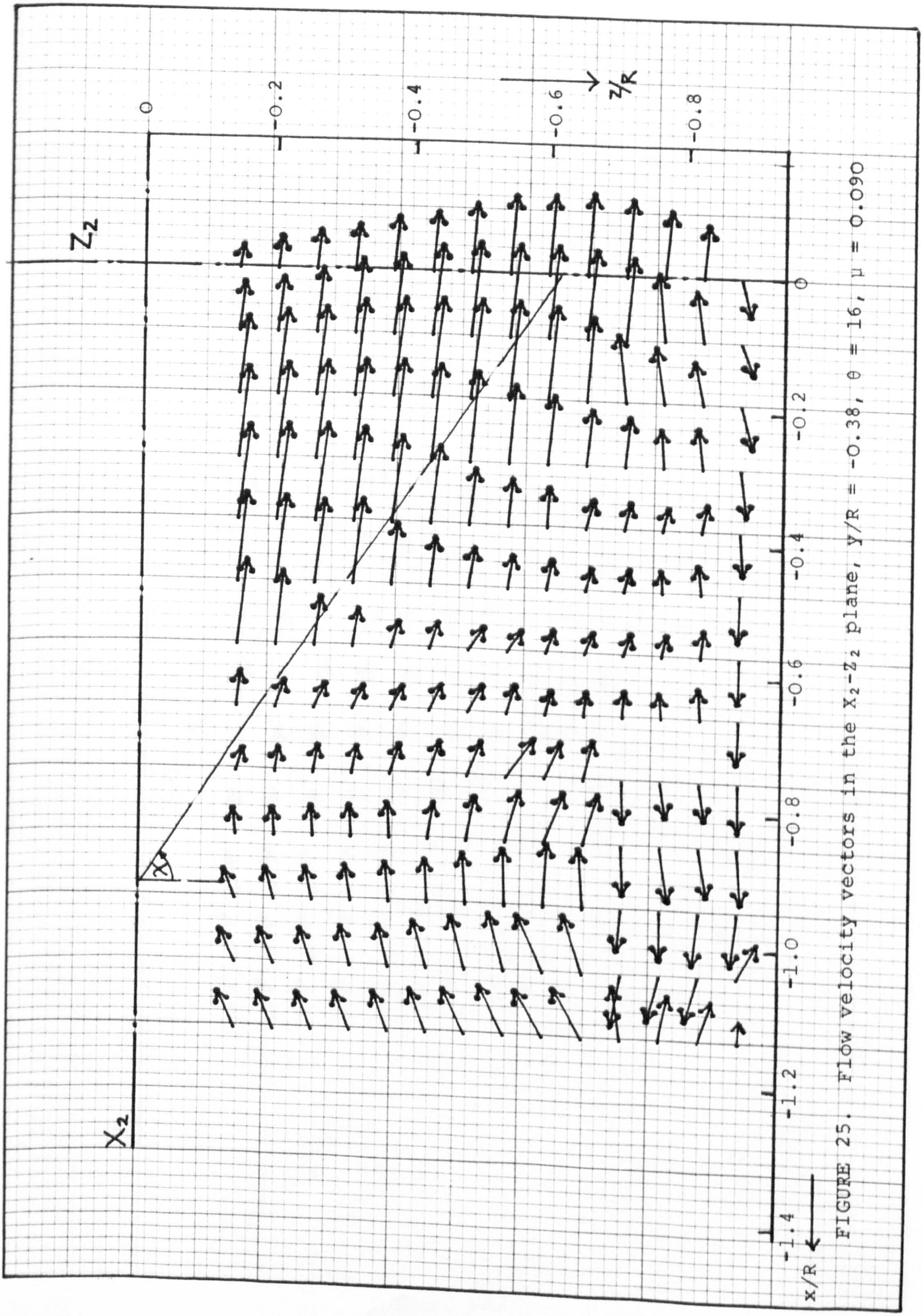

FIGURE 25. Flow velocity vectors in the X_2-Z_2 plane, Y/R = -0.38, θ = 16, η/δ = 0.090

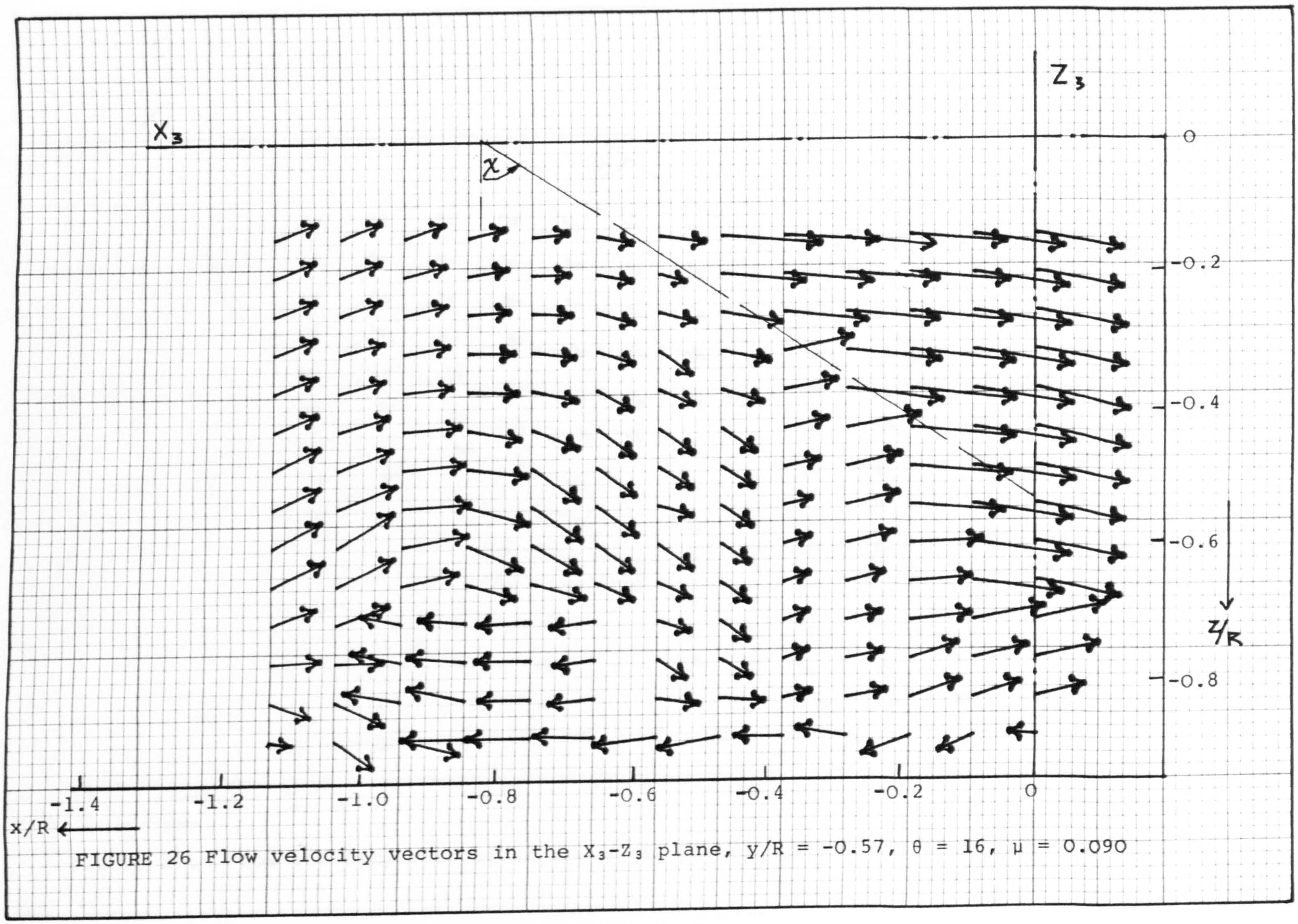

FIGURE 26 Flow velocity vectors in the X_3-Z_3 plane, y/R = -0.57, θ = 16, μ = 0.090

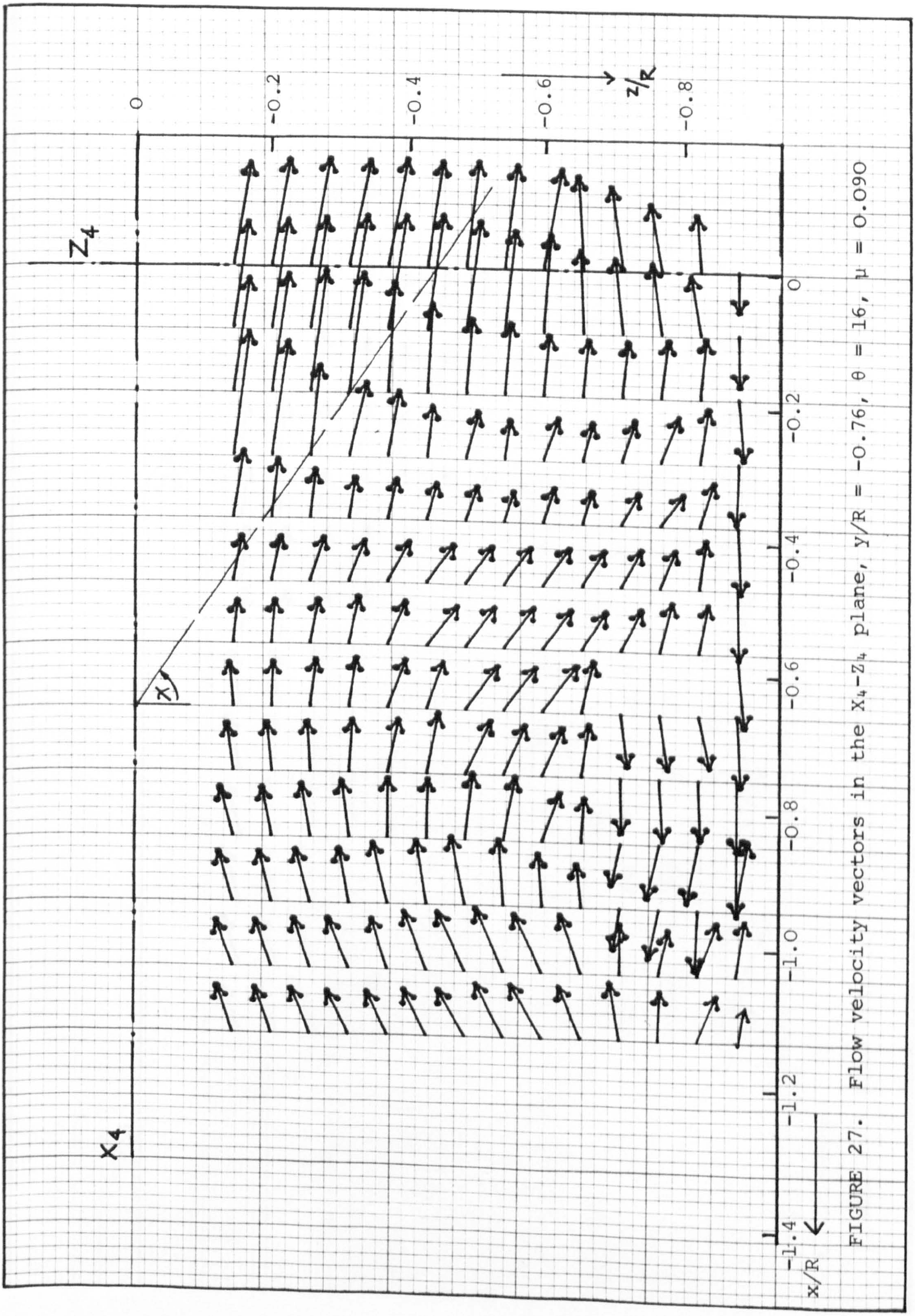
0
-0.2
-0.4
-0.6
-0.8
z/R
Z_4
X_4
χ
0
-0.2
-0.4
-0.6
-0.8
-1.0
-1.2
-1.4
x/R
Flow velocity vectors in the X_4-Z_4 plane, y/R = -0.76, θ = 16, μ = 0.090

FIGURE 27.

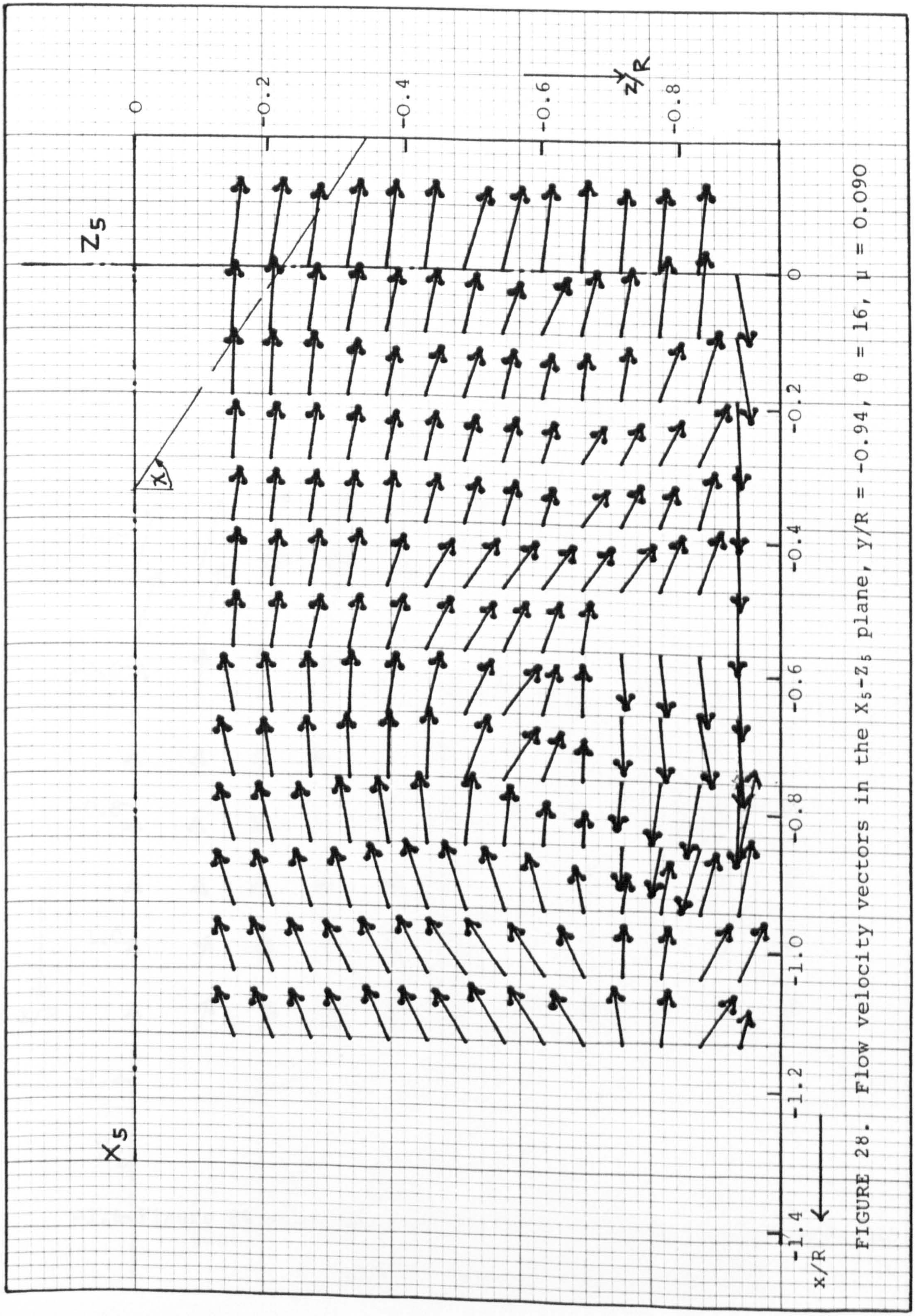

FIGURE 28. Flow velo

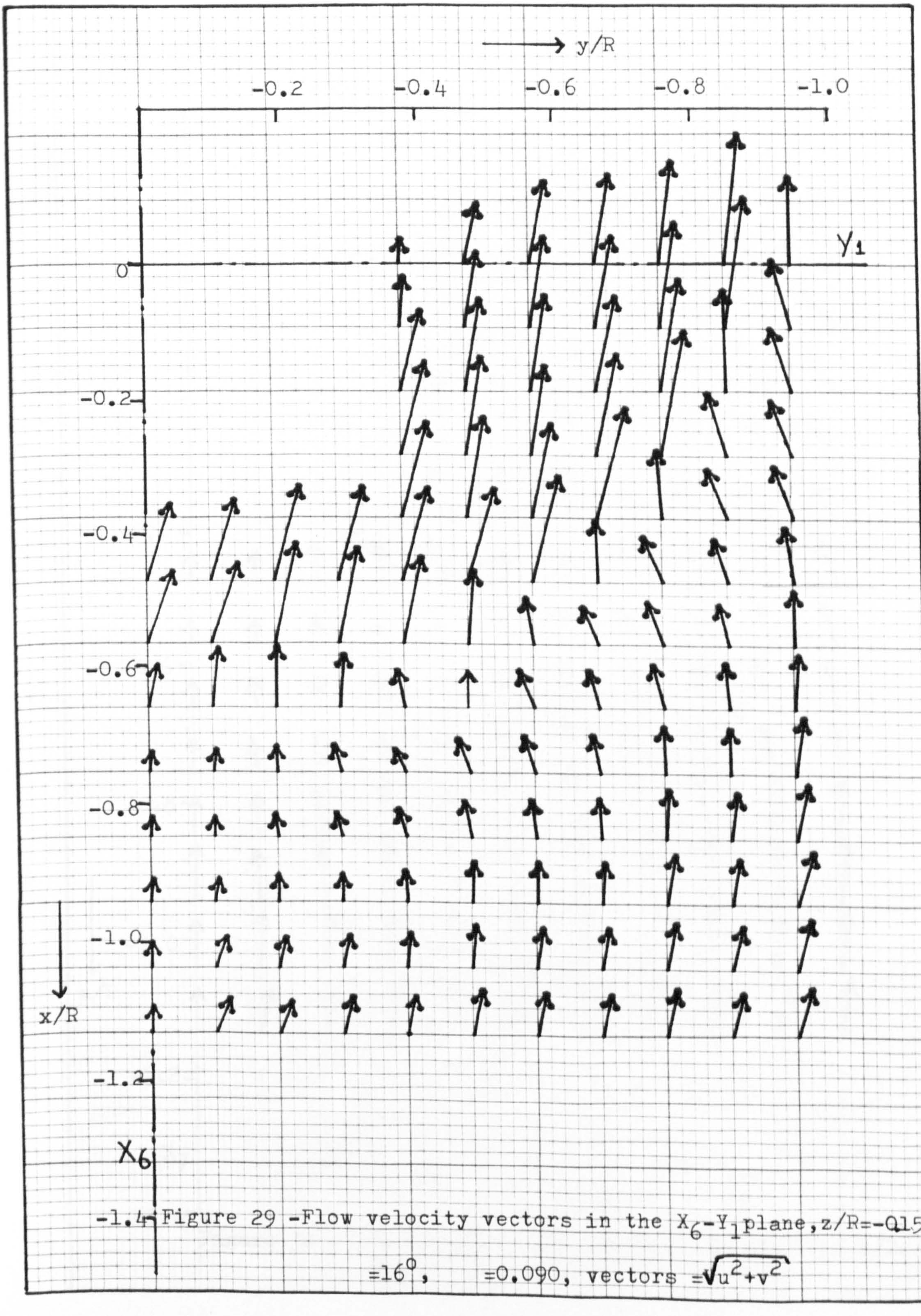

Figure 29 -Flow velocity vectors in the X_6-Y_1 plane, z/R=-0.15

=16°, =0.090, vectors =$\sqrt{u^2+v^2}$

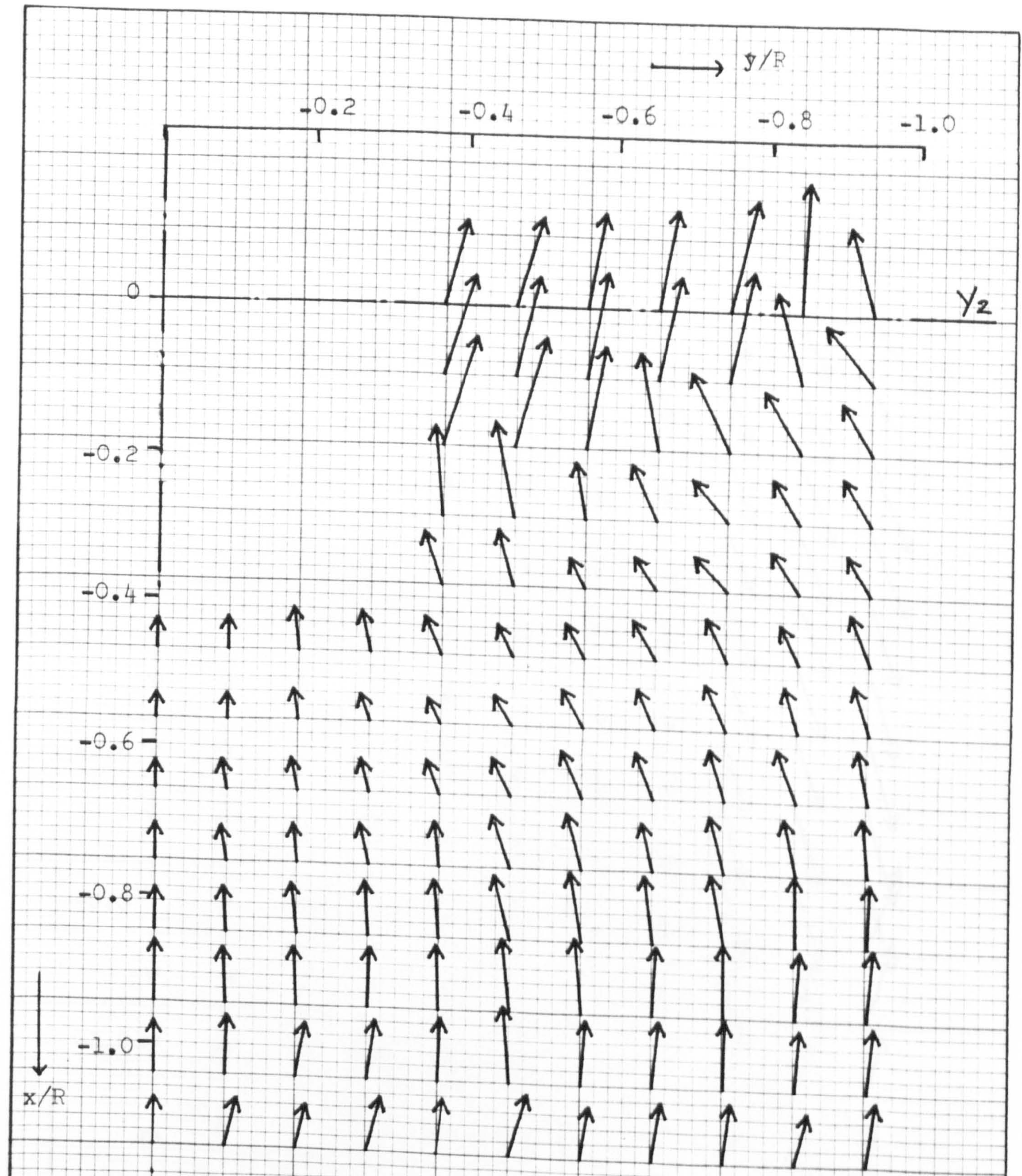

Figure 30 -Flow velocity vectors in the X_7-Y_2 plane, z/R=-0.55
θ=16°, μ=0.090

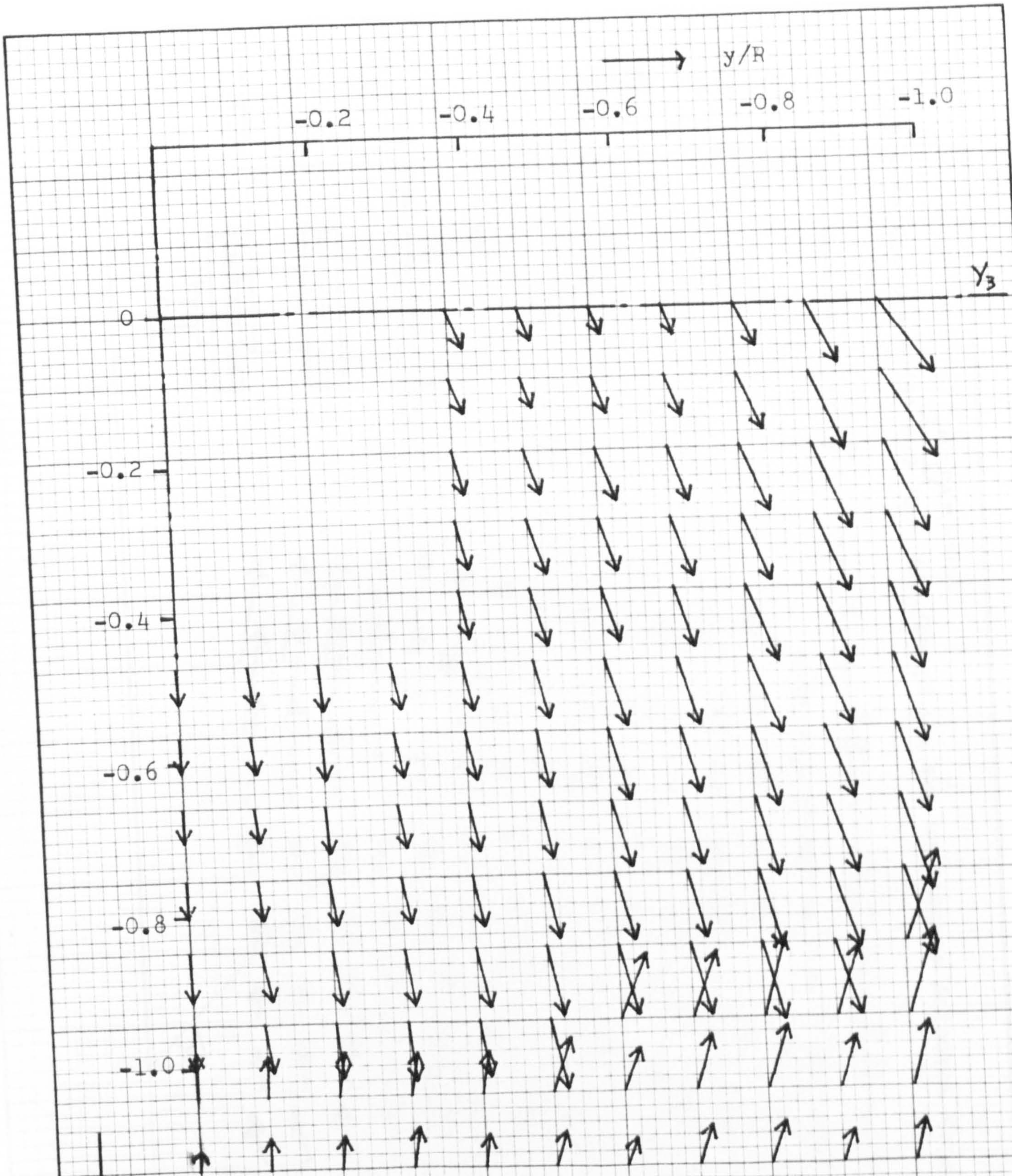

Figure 31 -Flow velocity vectors in the X_8-Y_3 plane, z/R= -0.79.
θ =16°, μ =0.090

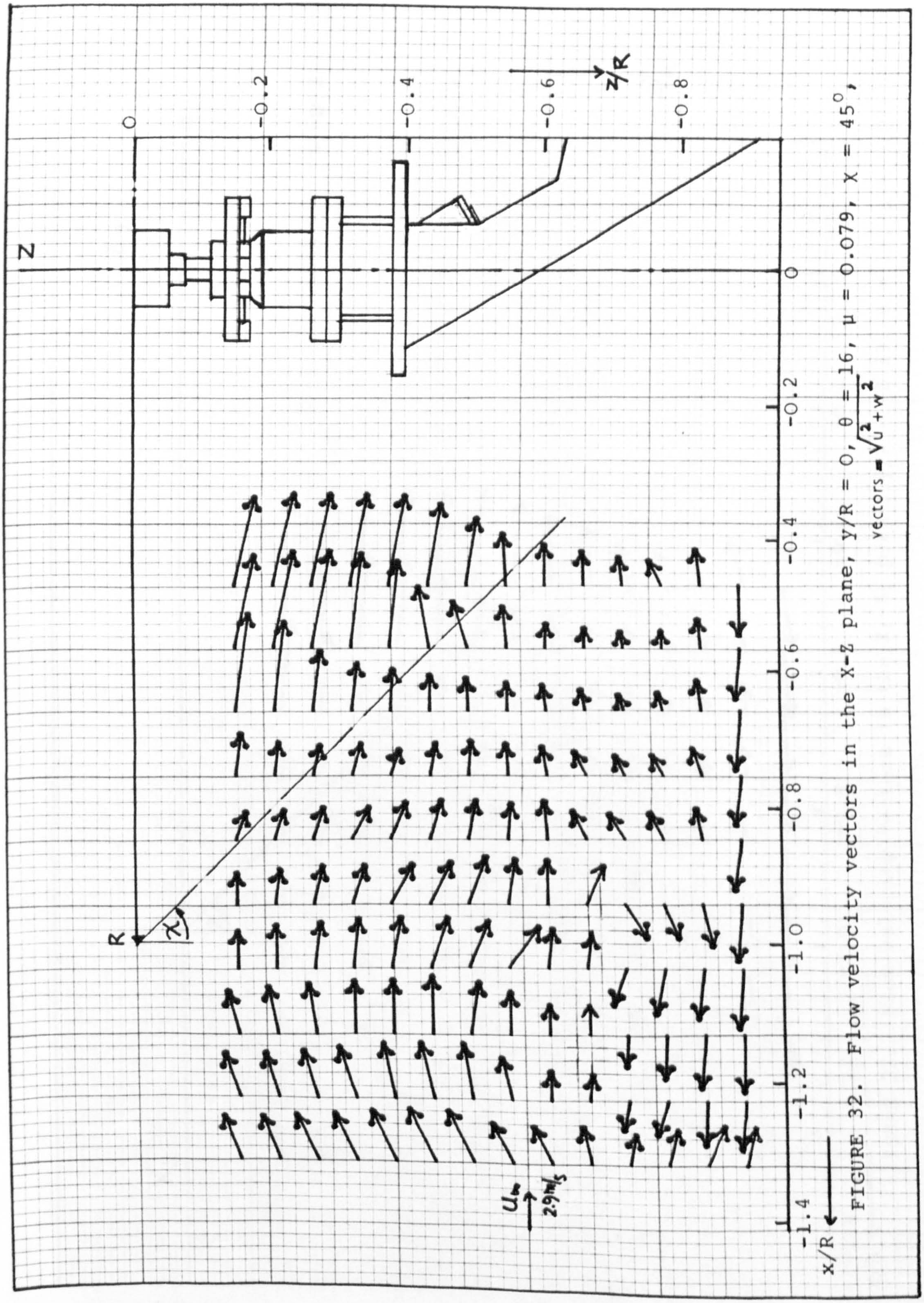

FIGURE 32. Flow velocity vectors in the X-Z plane, Y/R = 0, θ = 16, μ = -0.079, χ = 45°, vectors = $\sqrt{u^2+w^2}$

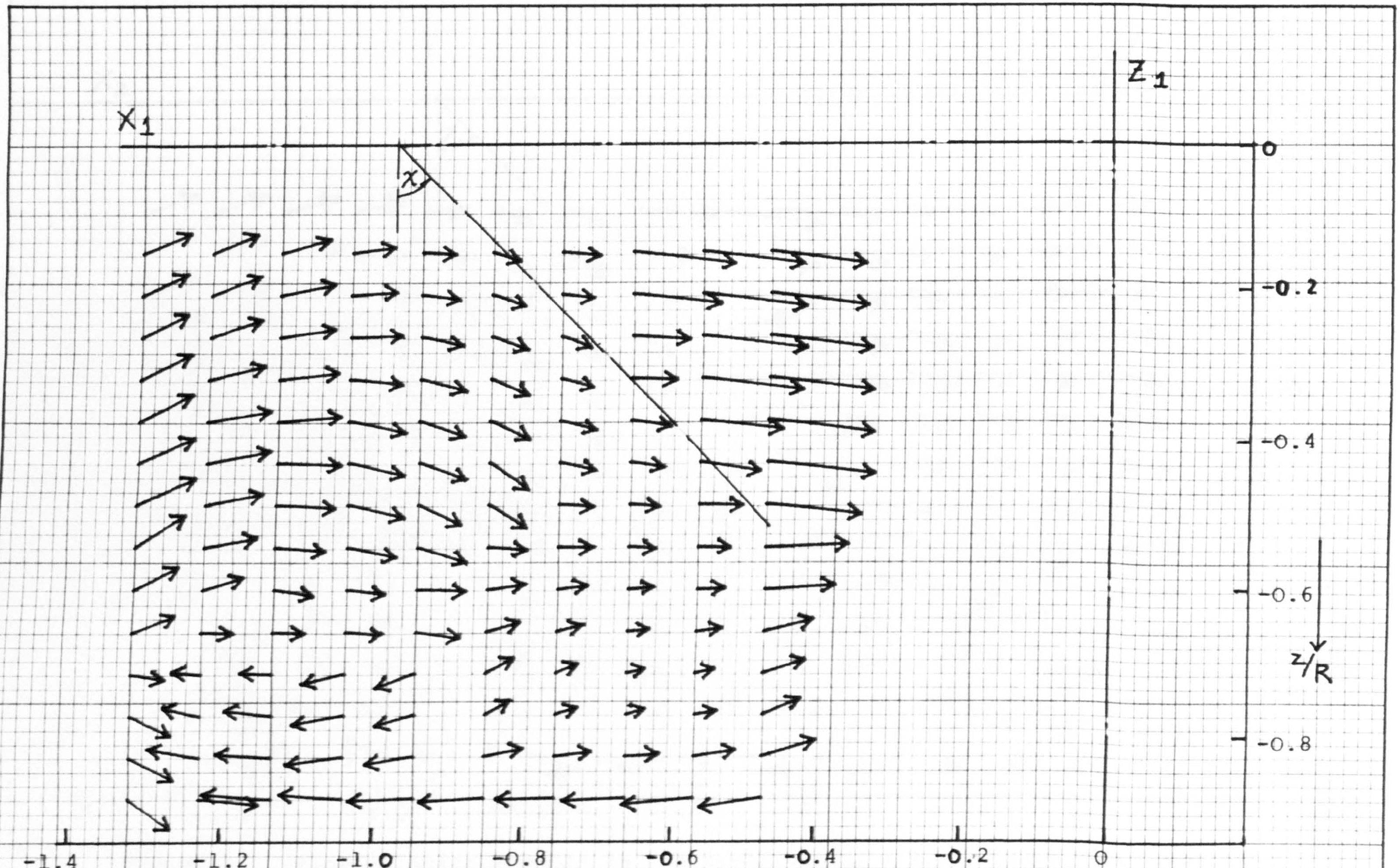

FIGURE 33. Flow velocity vectors in the X_1-Z_1 plane, y/R = -0.19, θ = 16, μ = 0.079

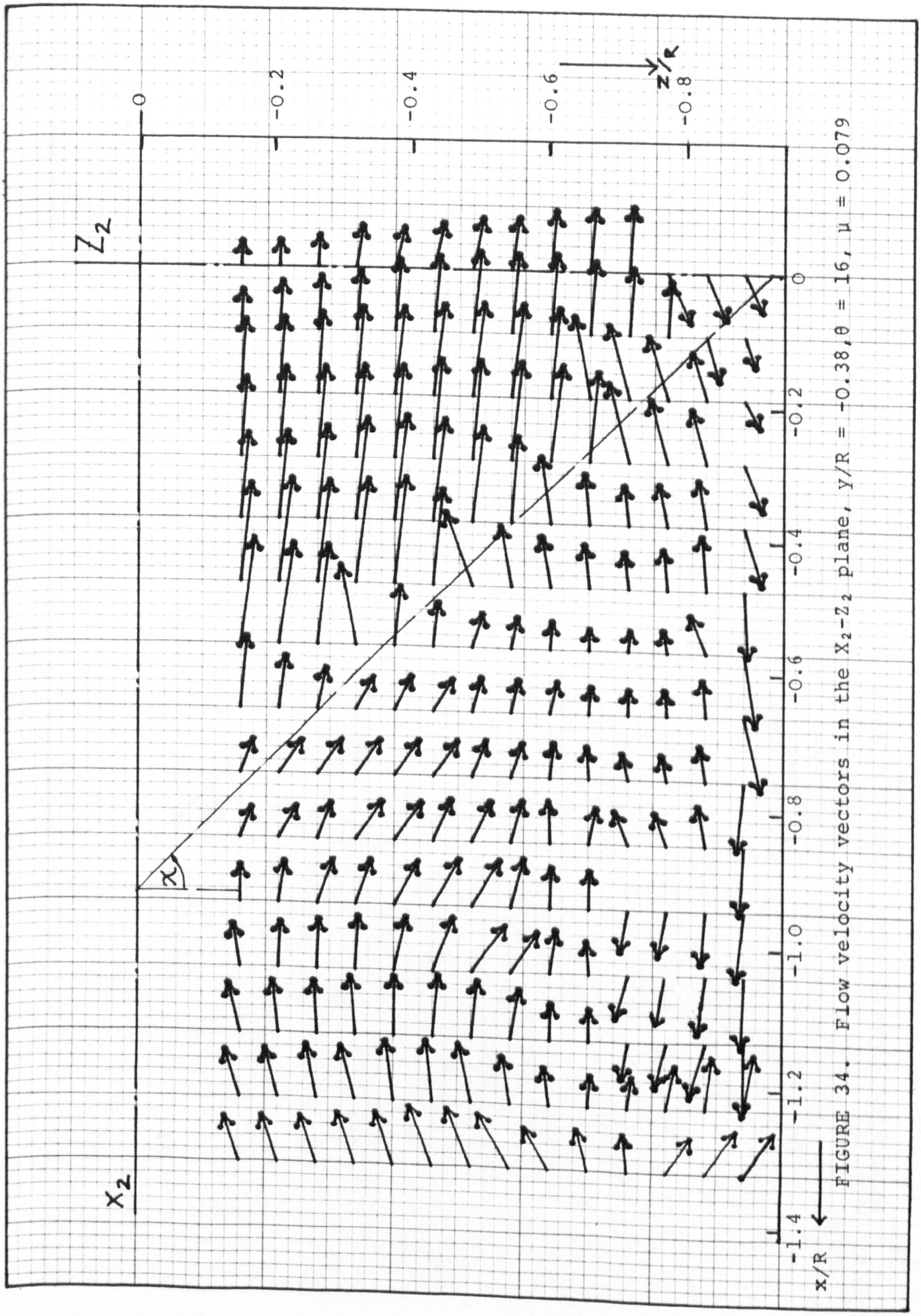

FIGURE 34. Flow velocity vectors in the X_2-Z_2 plane, y/R = -0.38, θ = 16, μ = 0.079

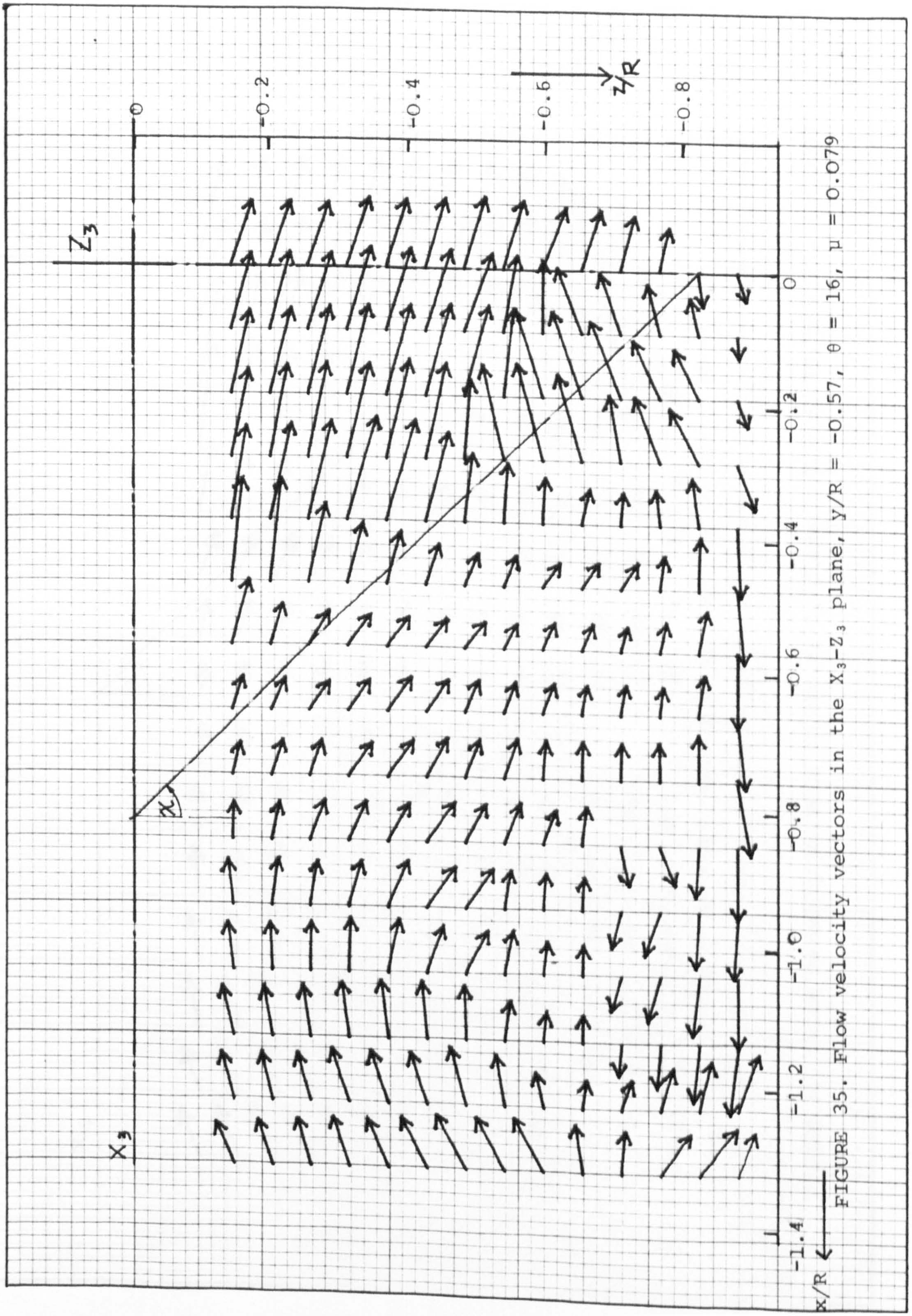

FIGURE 35. Flow velocity vectors in the X_3–Z_3 plane, y/R = -0.57, θ = 16°, μ = 0.076

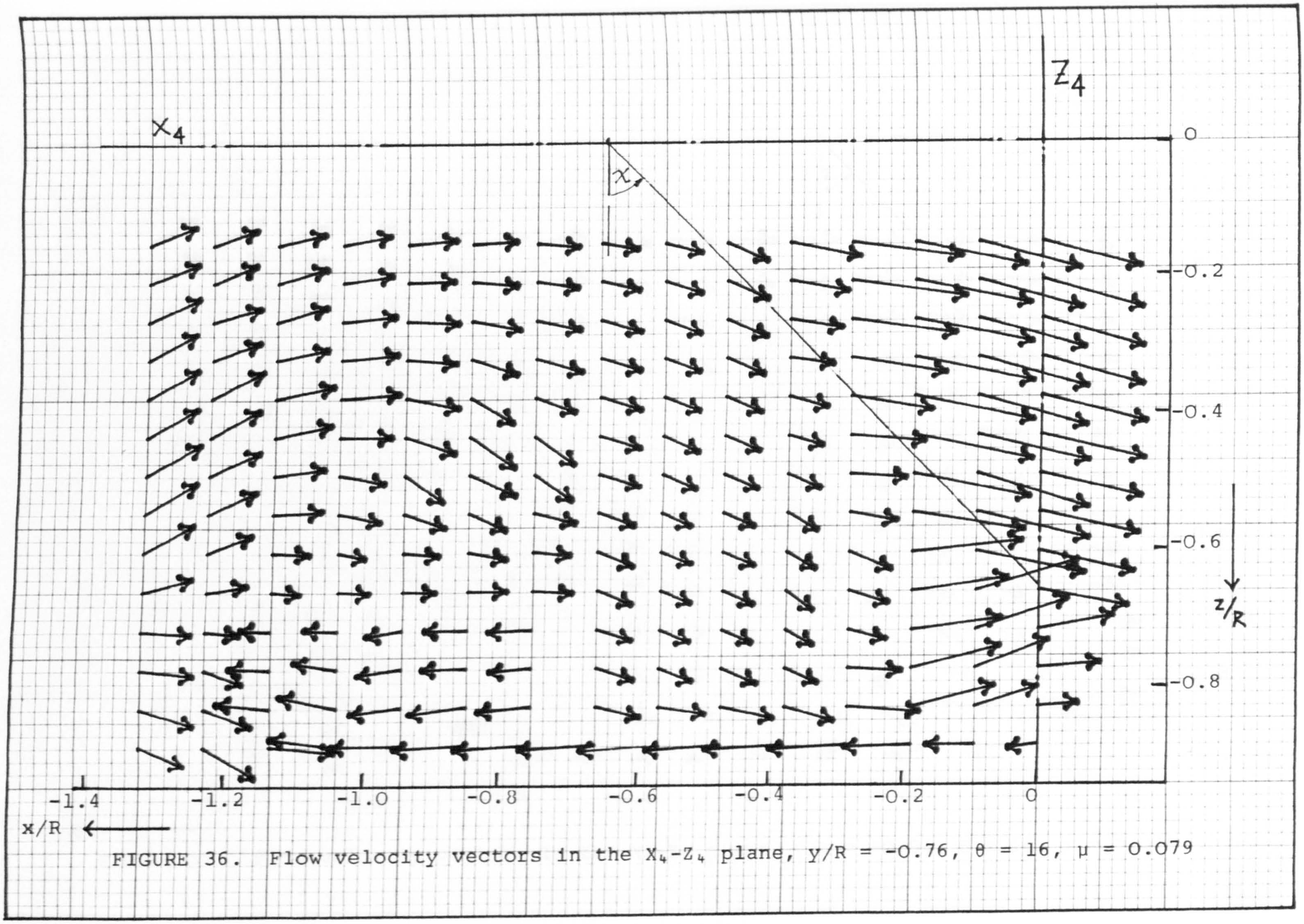

FIGURE 36. Flow velocity vectors in the X_4-Z_4 plane, y/R = -0.76, θ = 16, μ = 0.079

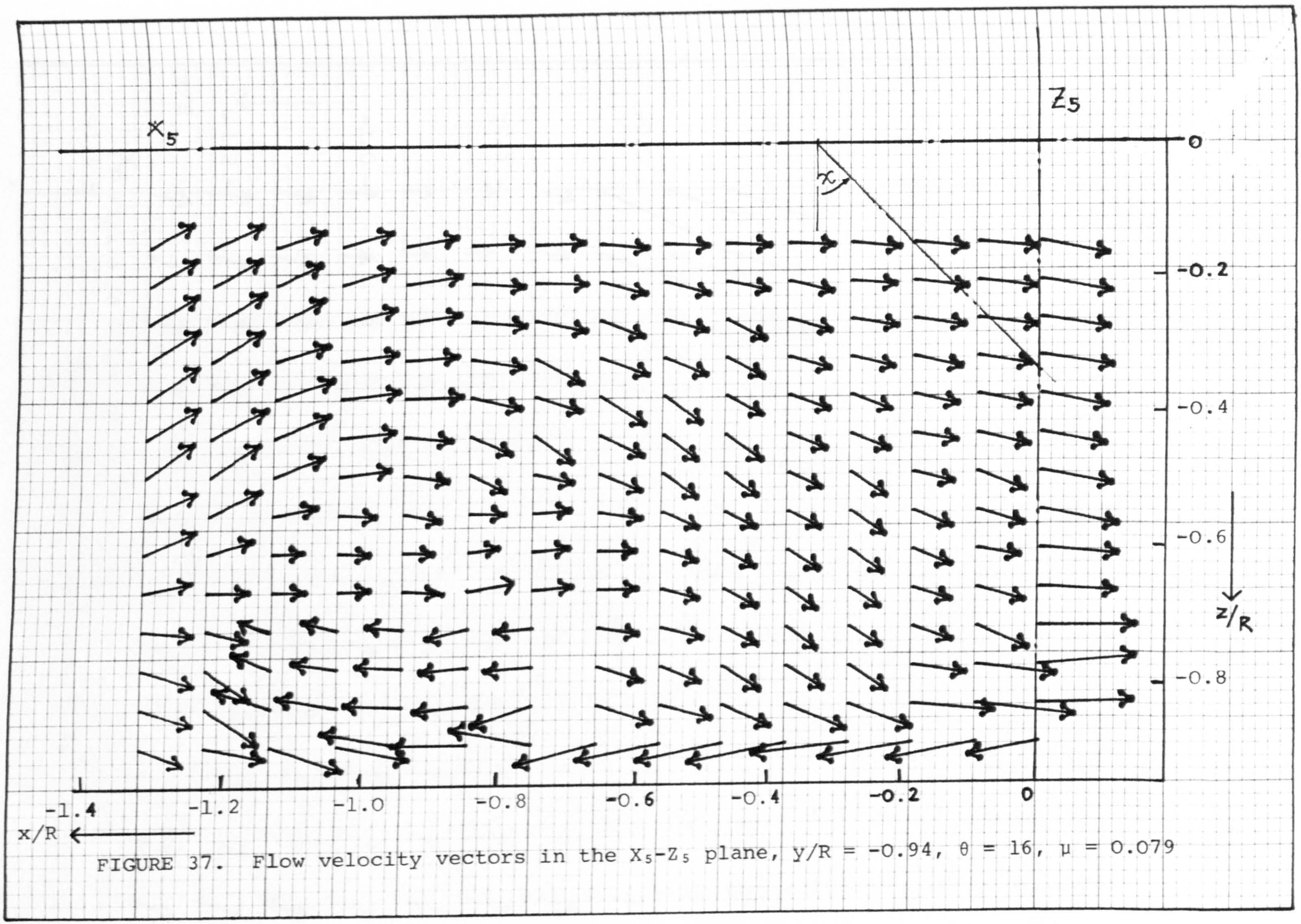

FIGURE 37. Flow velocity vectors in the X_5-Z_5 plane, y/R = -0.94, θ = 16, μ = 0.079

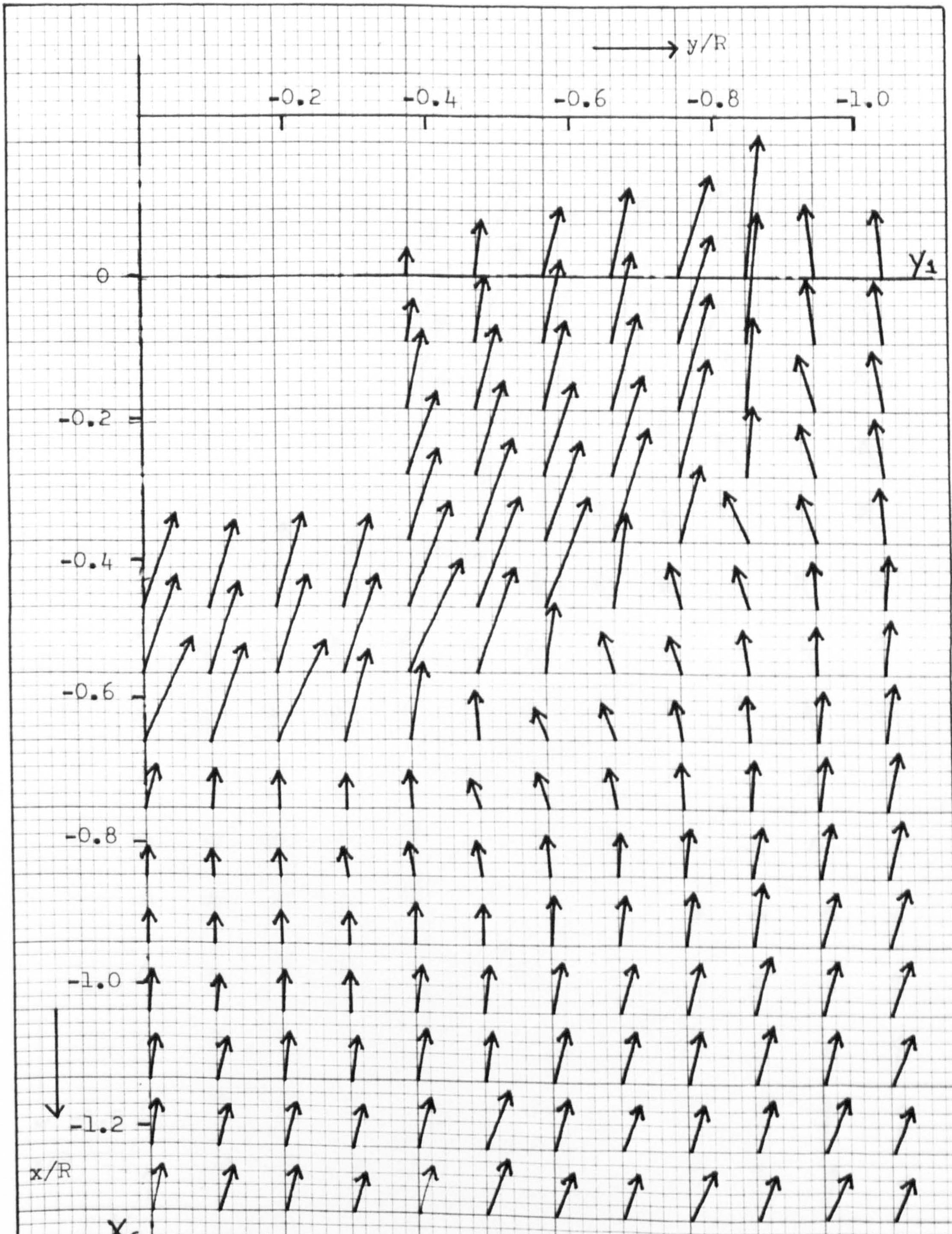

Figure 38 -Flow velocity vectors in the X_6-Y_1 plane, z/R=-0.15
$\theta=16^{o}$, $\mu=0.079$, vectors=$\sqrt{u^2+v^2}$

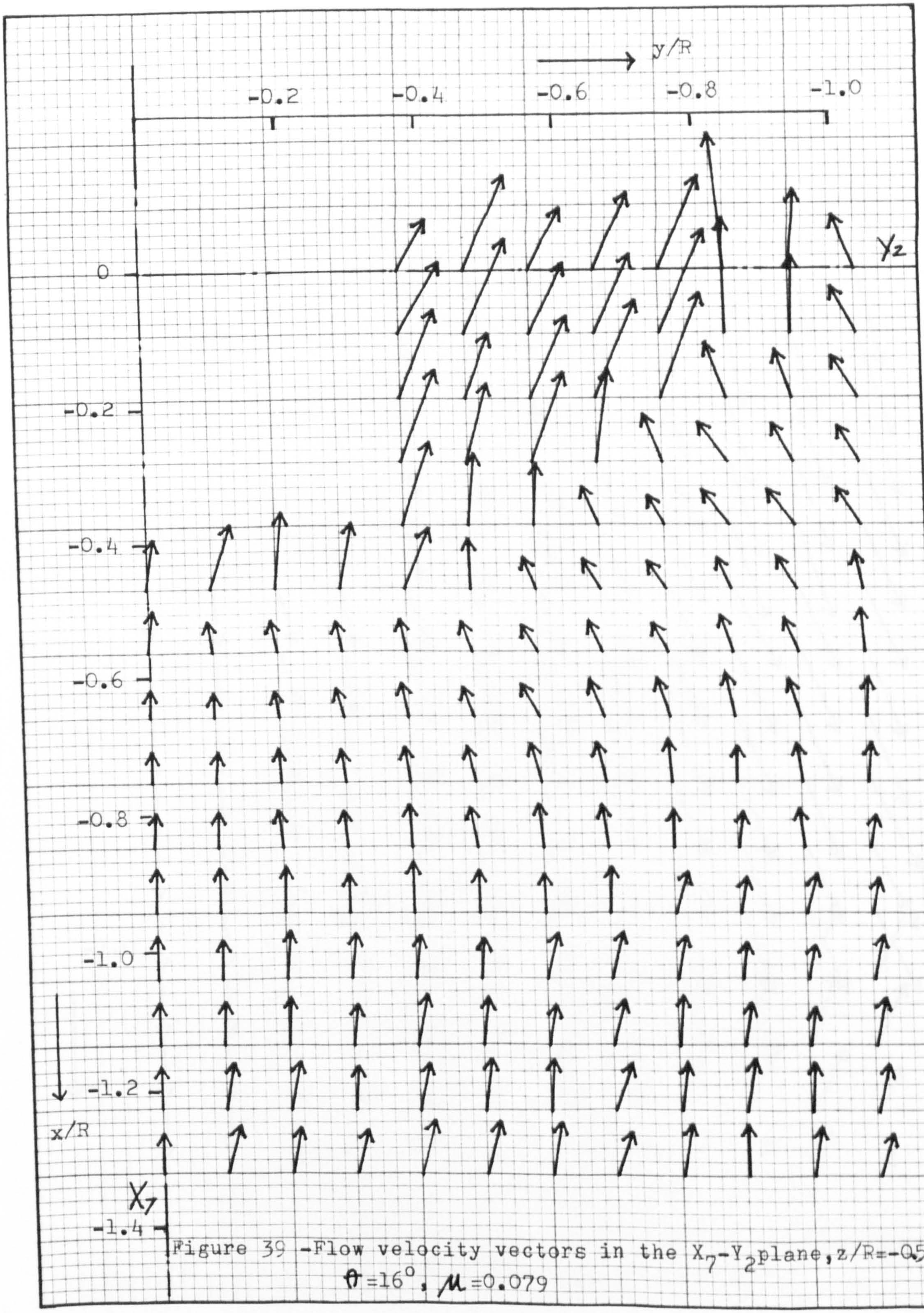

Figure 39 -Flow velocity vectors in the X_7-Y_2 plane, z/R=-0.55
$\theta = 16^{\circ}$, $\mu = 0.079$

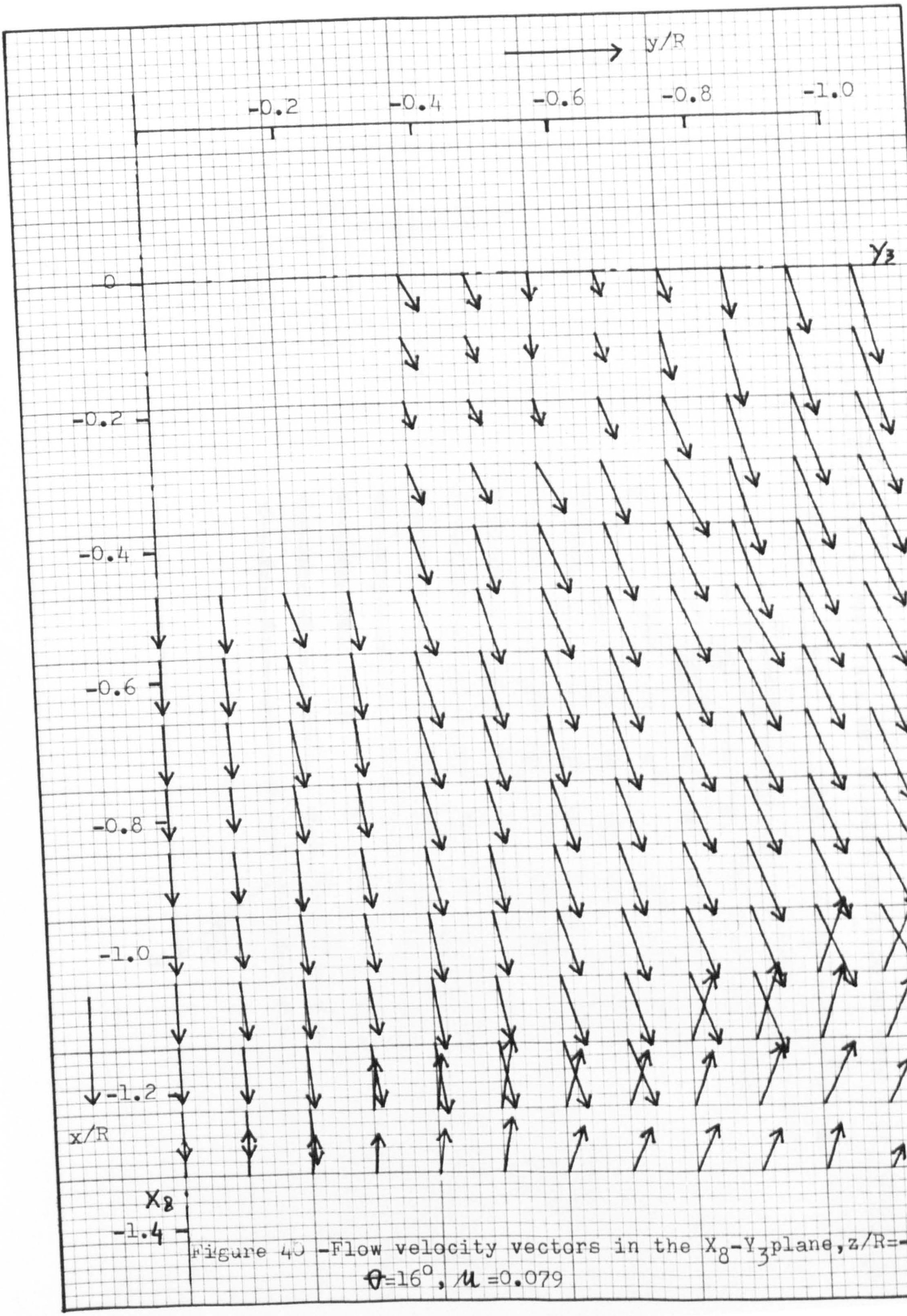

Figure 40 -Flow velocity vectors in the X_8-Y_3 plane, z/R=-0.79
$\theta=16^{\circ}$, $\mu=0.079$

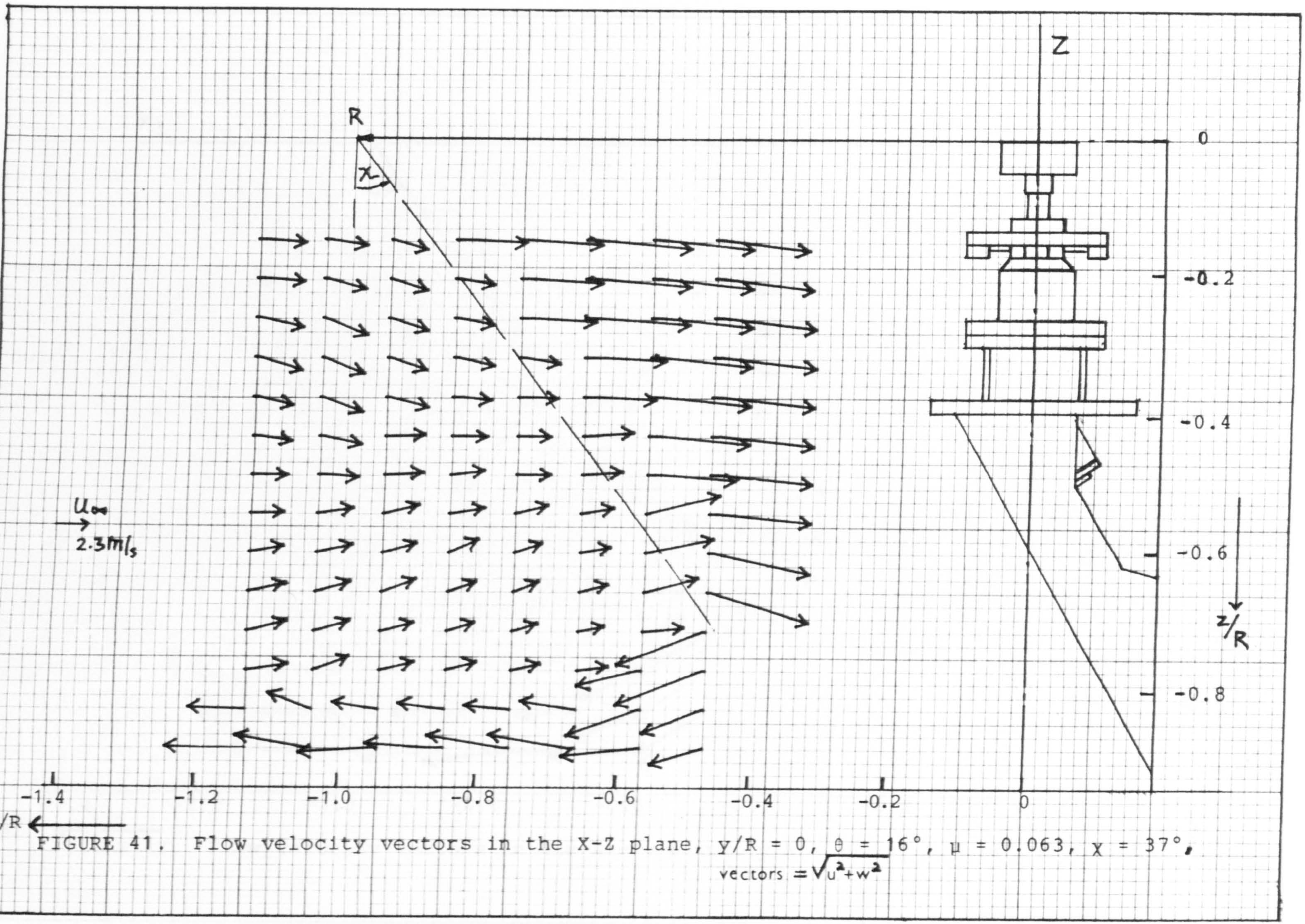

FIGURE 41. Flow velocity vectors in the X-Z plane, y/R = 0, θ = 16°, μ = 0.063, χ = 37°,

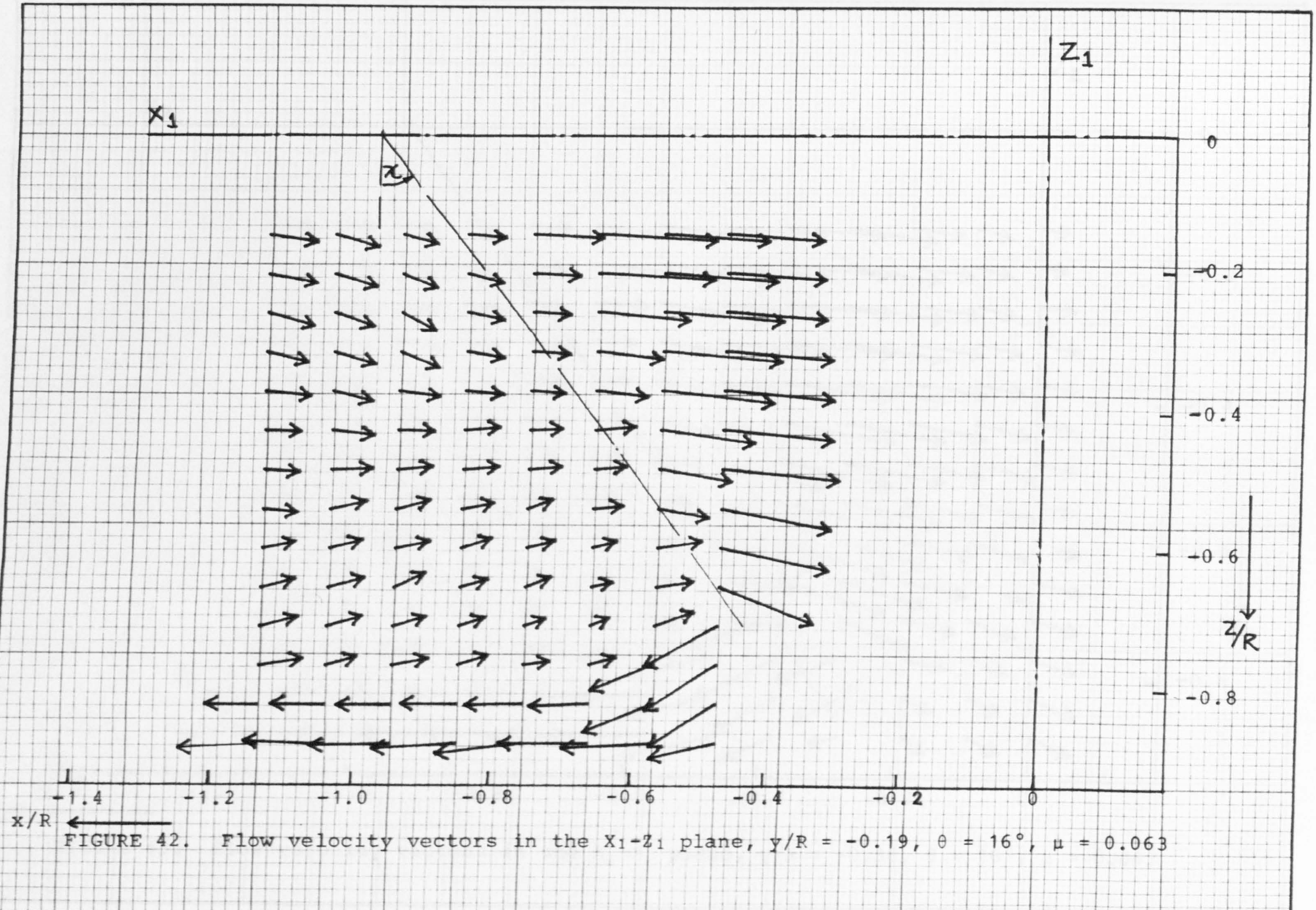

FIGURE 42. Flow velocity vectors in the X_1-Z_1 plane, y/R = -0.19, θ = 16°, μ = 0.063

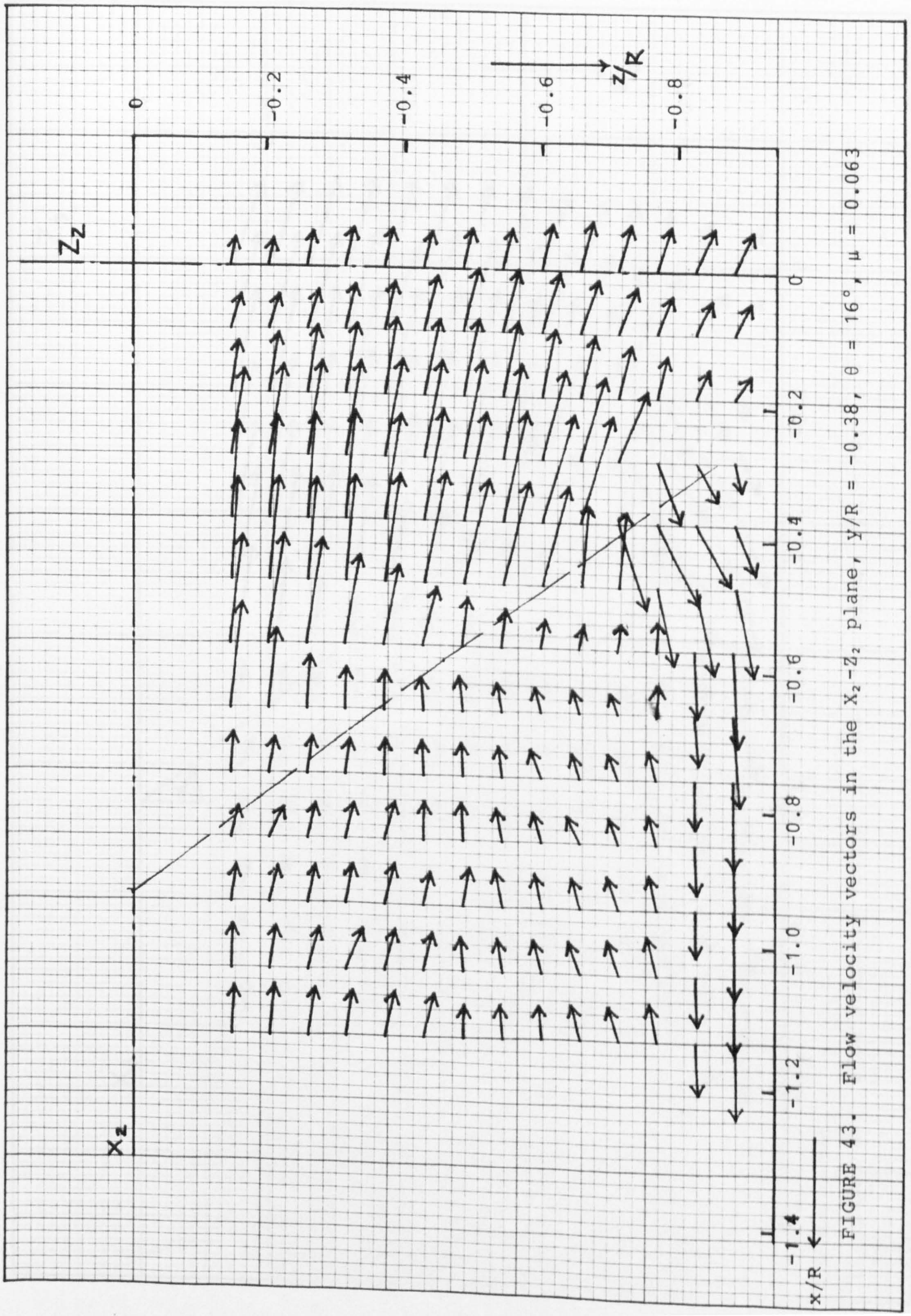

FIGURE 43. Flow velocity vectors in the X_2-Z_2 plane, Y/R = -0.38, θ = 16°, μ = 0.063

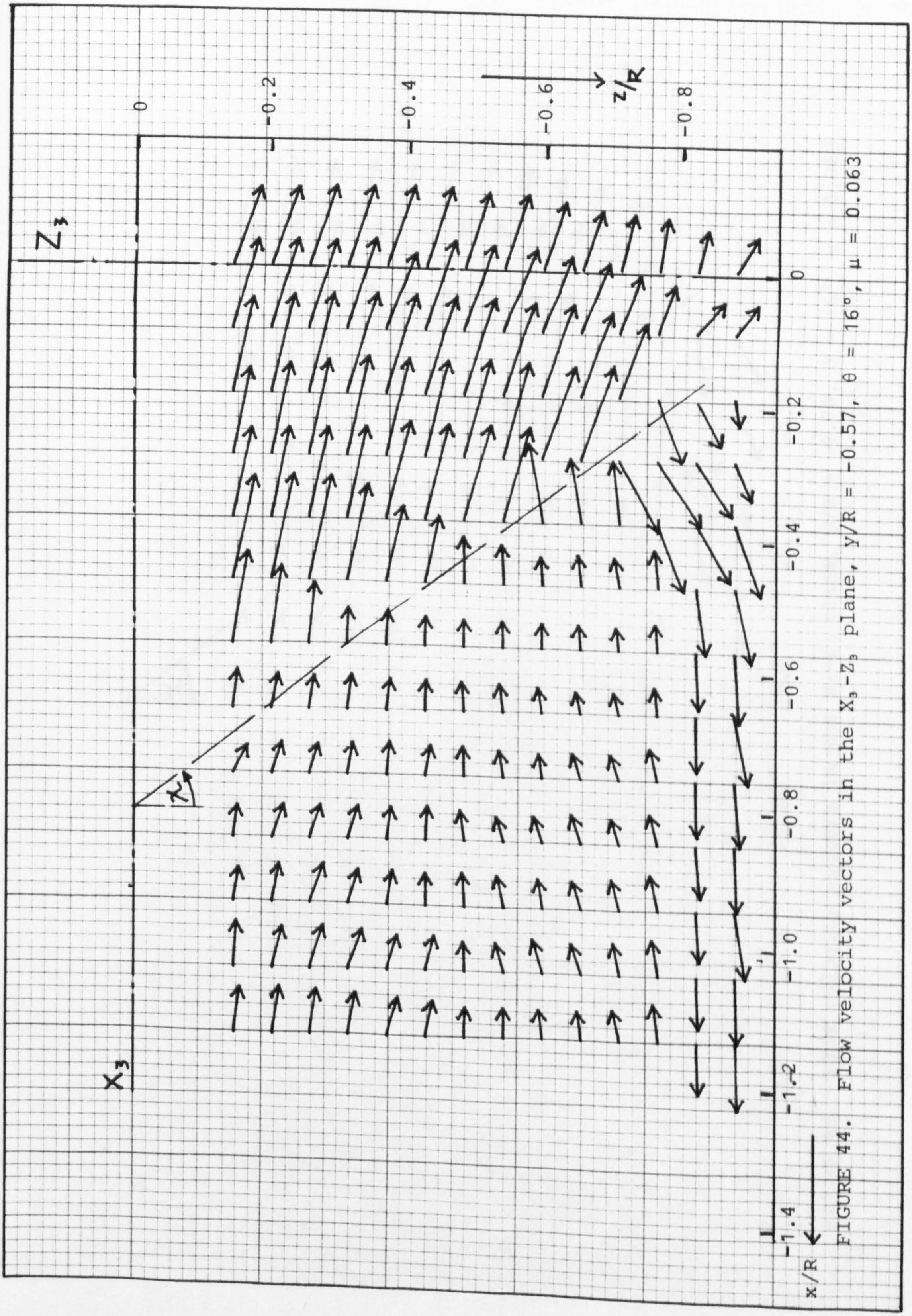
0
-0.2
-0.4
-0.6
-0.8
z/R
Z_3
X_3
x/R
0
-0.2
-0.4
-0.6
-0.8
-1.0
-1.2
-1.4
$\mu = 0.063$, $y/R = -0.57$, $\theta = 16°$,
Flow velocity vectors in the X_3-Z_3 plane,

FIGURE 44.

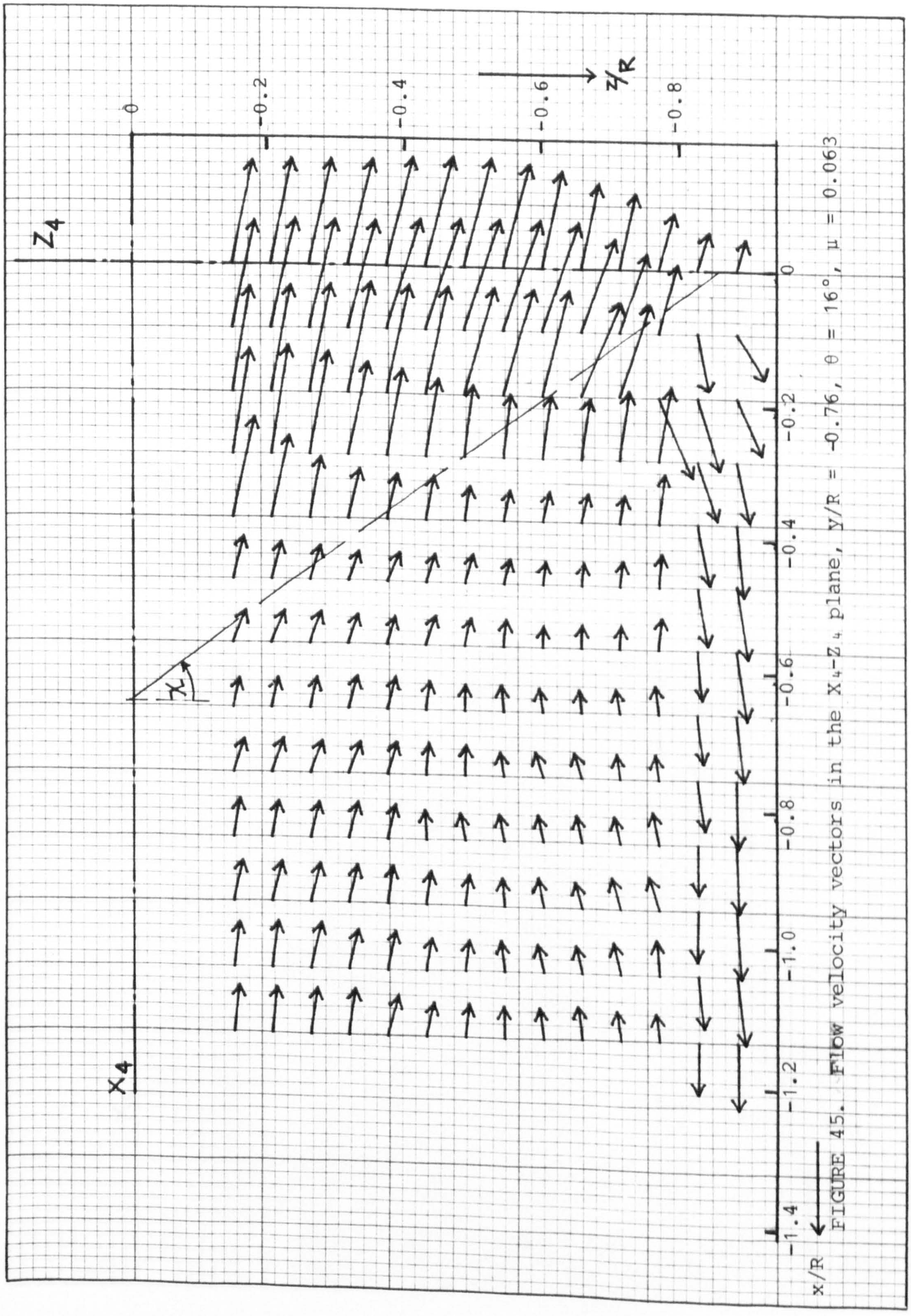

FIGURE 45. Flow velocity vectors in the X_4-Z_4 plane,

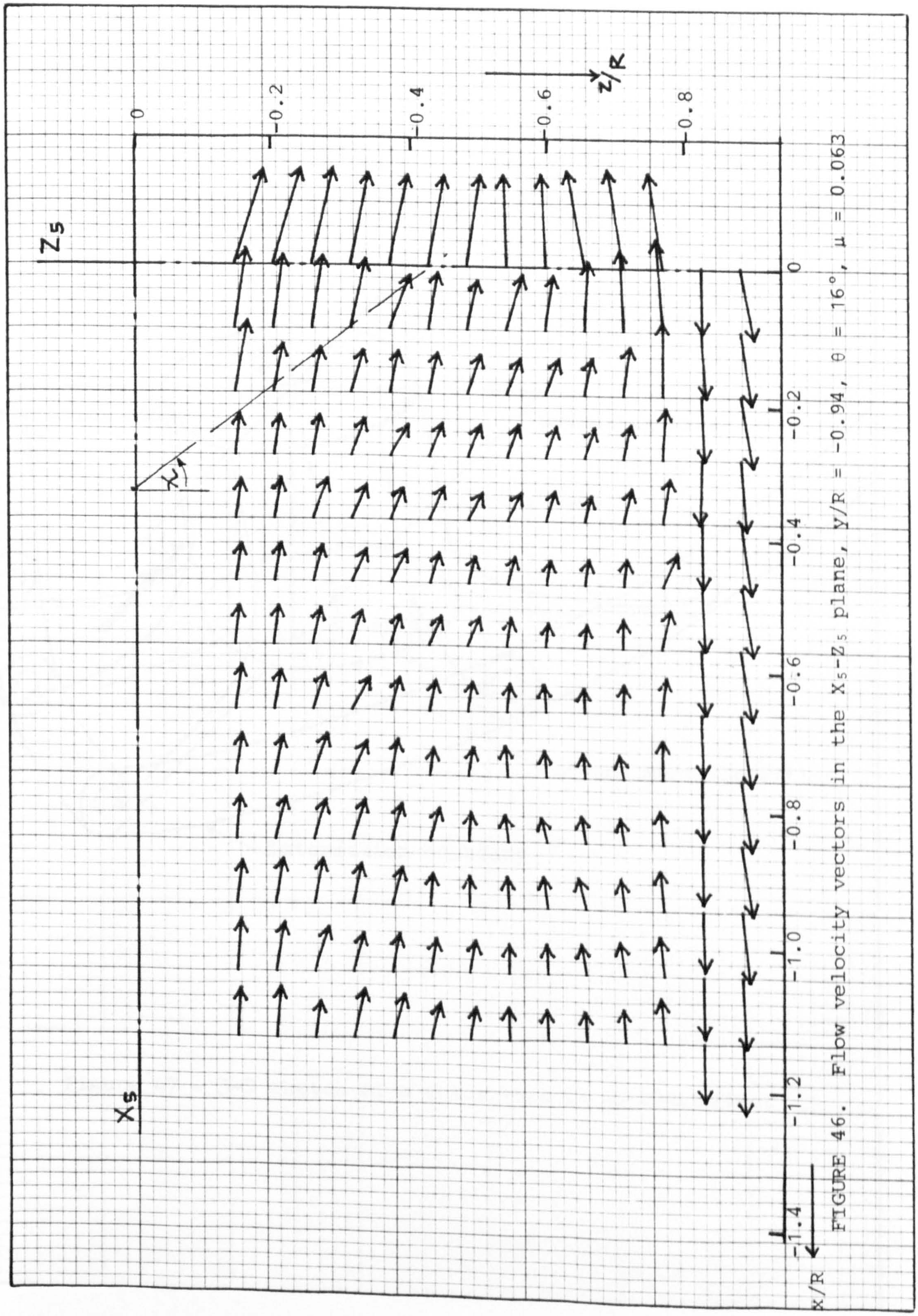
z/R
0
-0.2
-0.4
-0.6
-0.8
Z_5
Y_5
X_5
0
-0.2
-0.4
-0.6
-0.8
-1.0
-1.2
-1.4
x/R
Flow velocity vectors in the X_5-Z_5 plane, y/R = -0.94, θ = 16°, μ = 0.063

FIGURE 46.

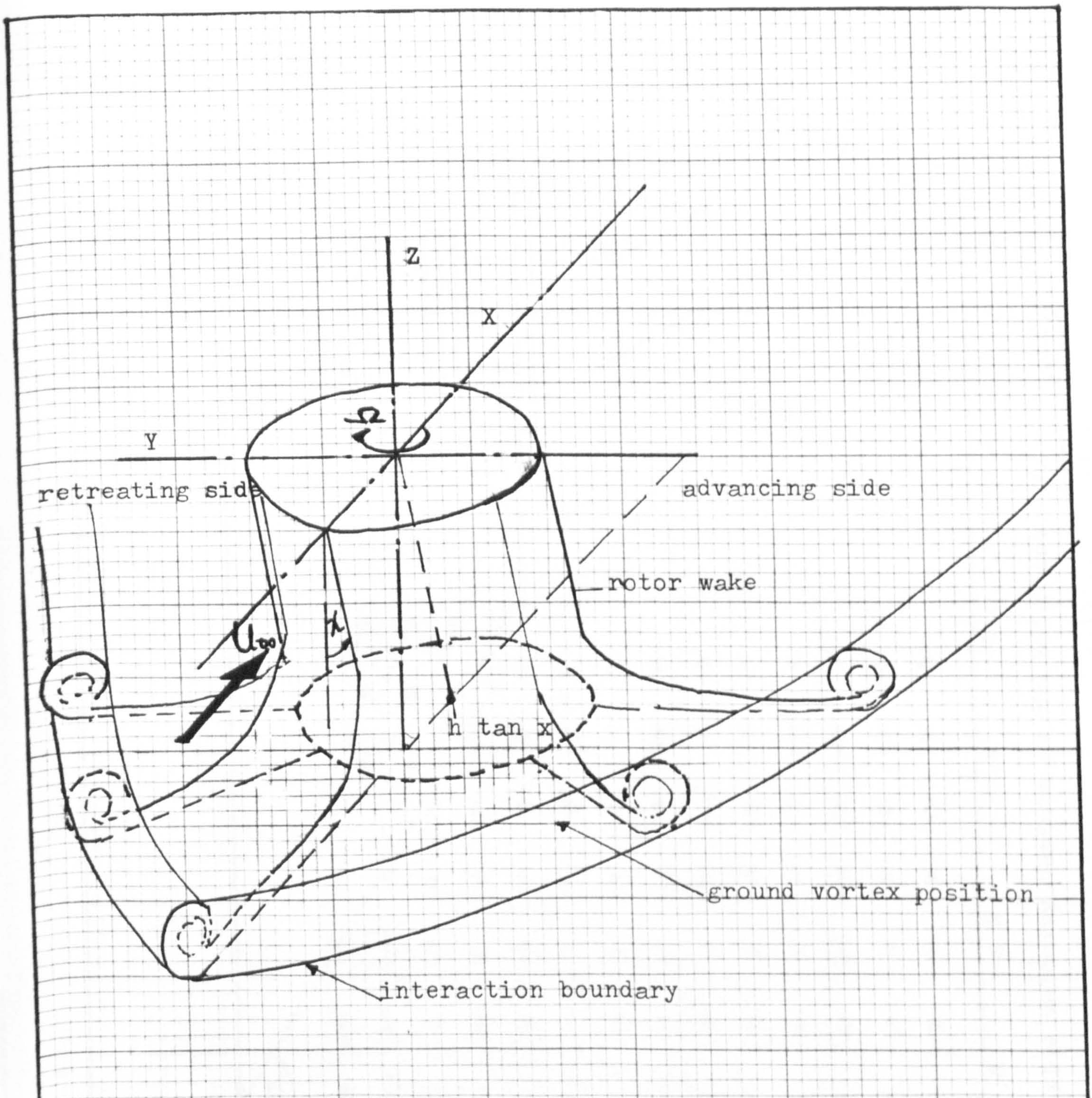

Figure 47 - 3-D sketch of a rotor wake in ground effect

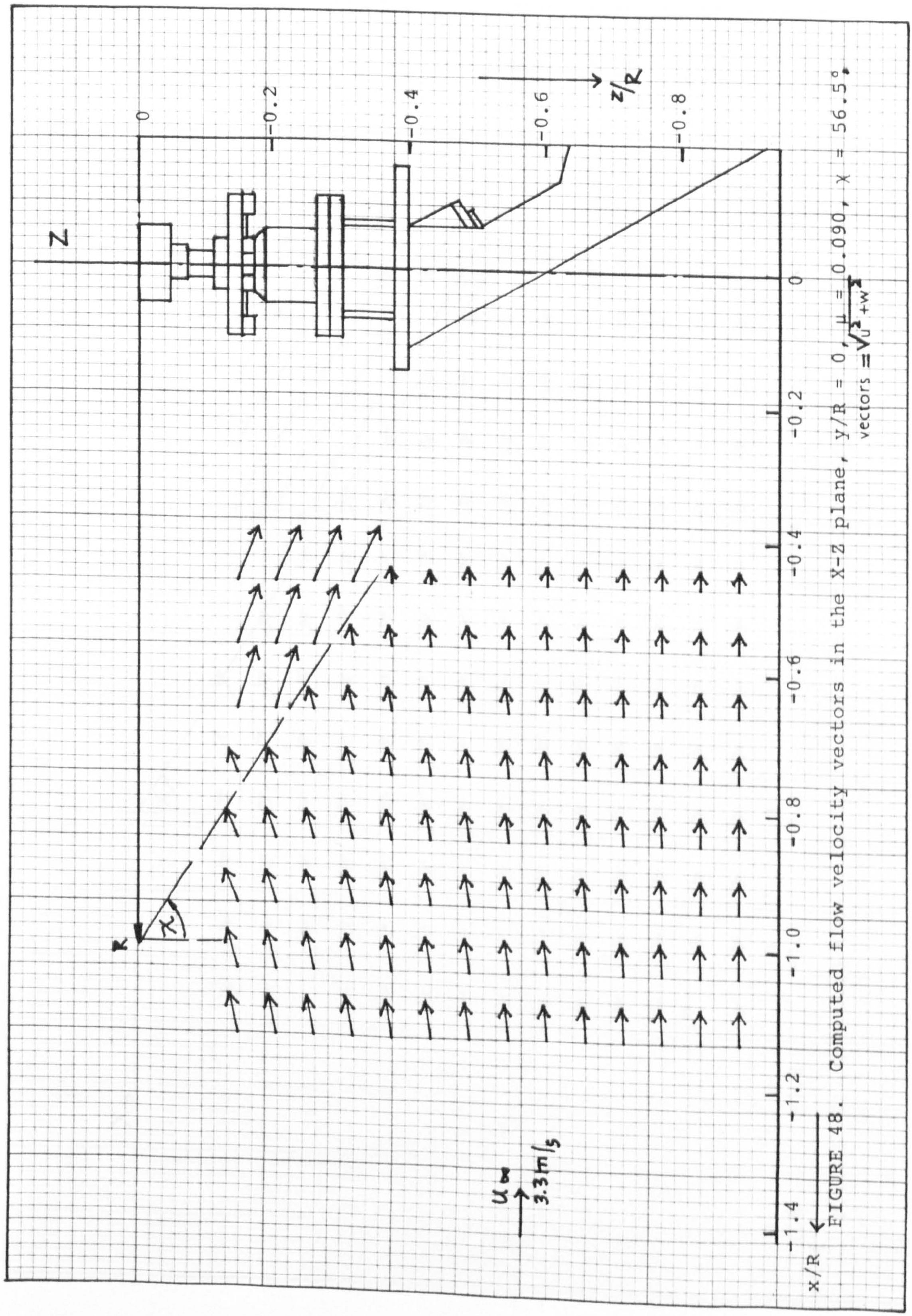

FIGURE 48. Computed

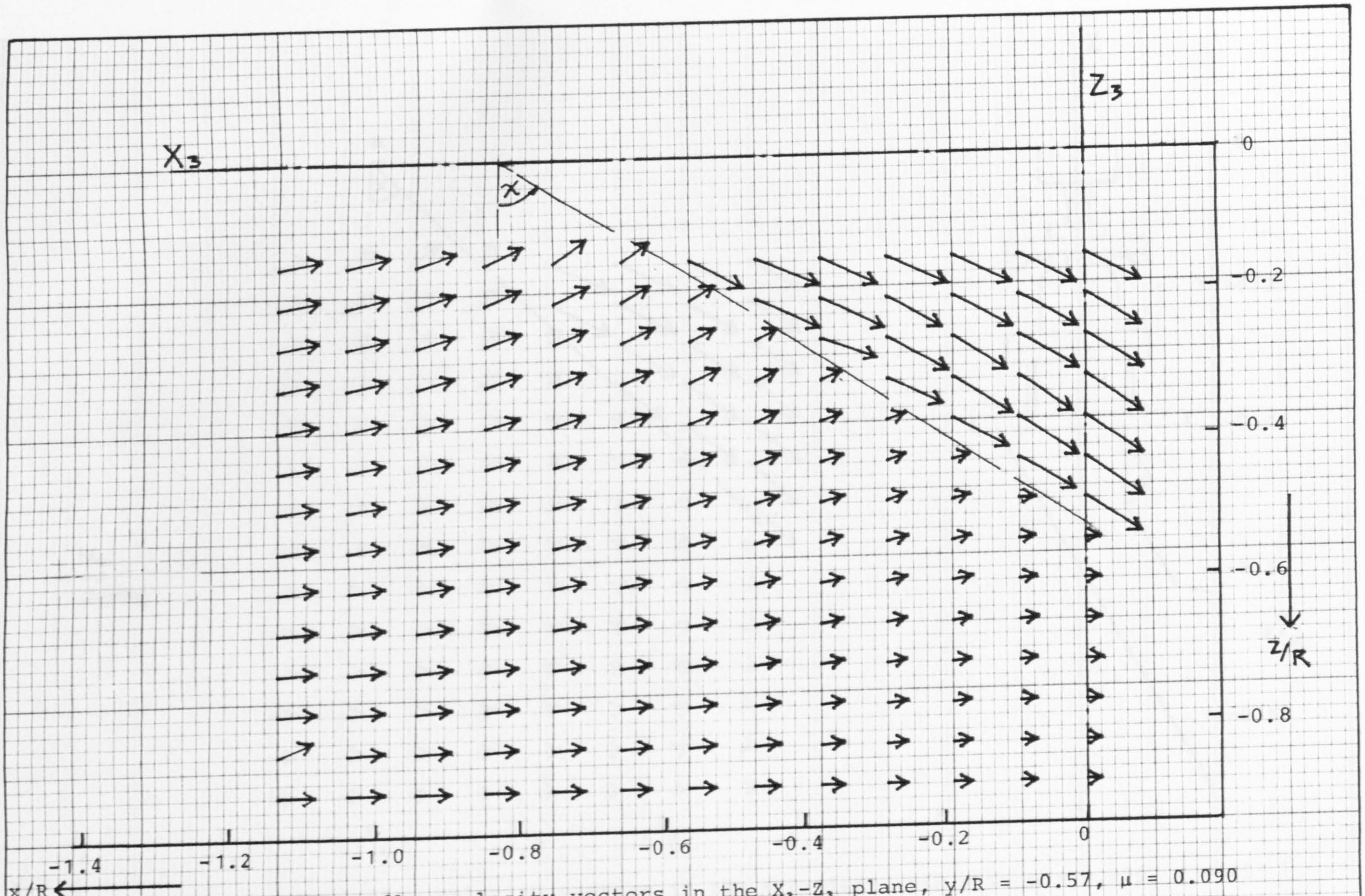

FIGURE 49. Computed flow velocity vectors in the X_3-Z_3 plane, $y/R = -0.57$, $\mu = 0.090$

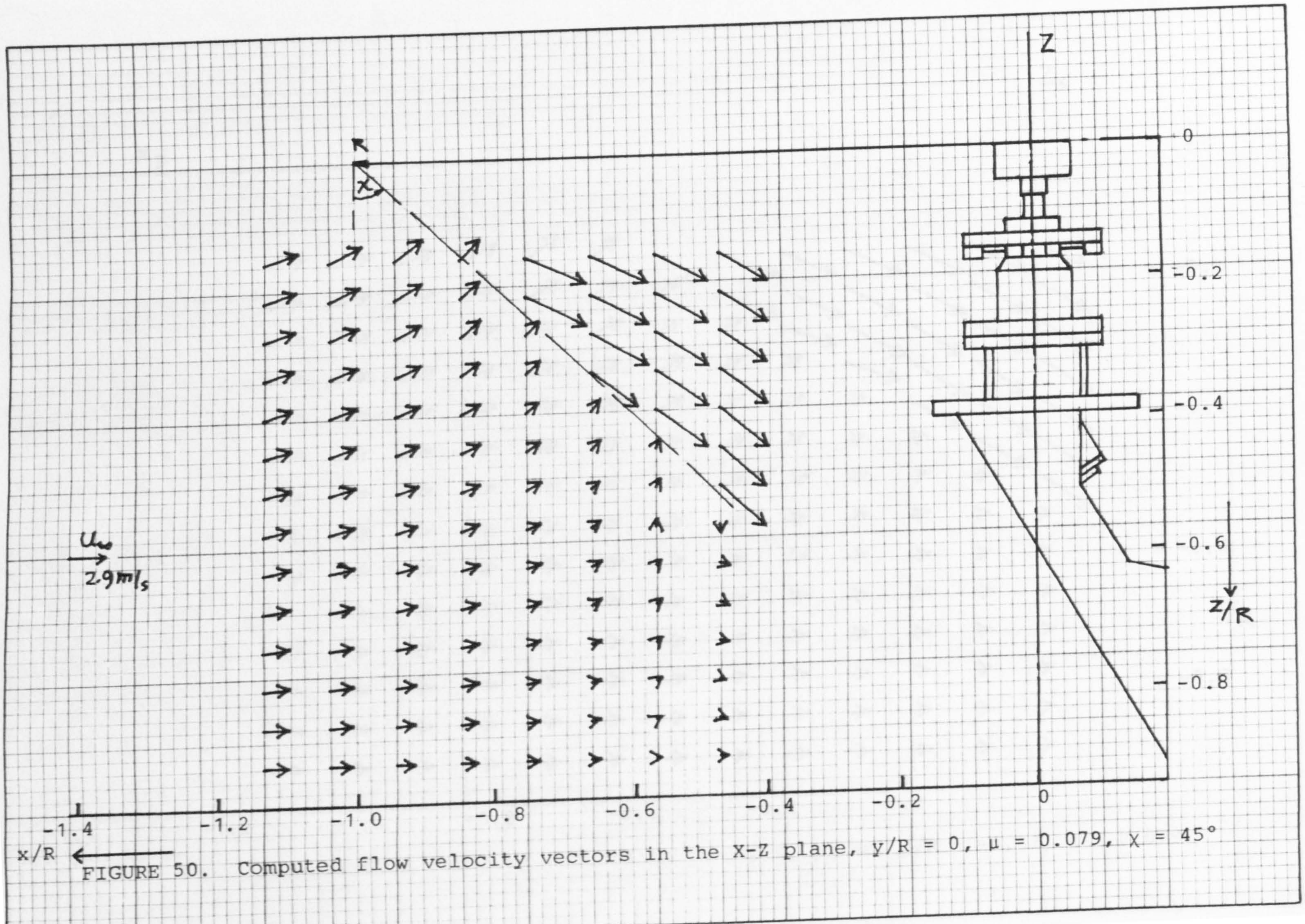

FIGURE 50. Computed flow velocity vectors in the X-Z plane, y/R = 0, μ = 0.079, χ = 45°

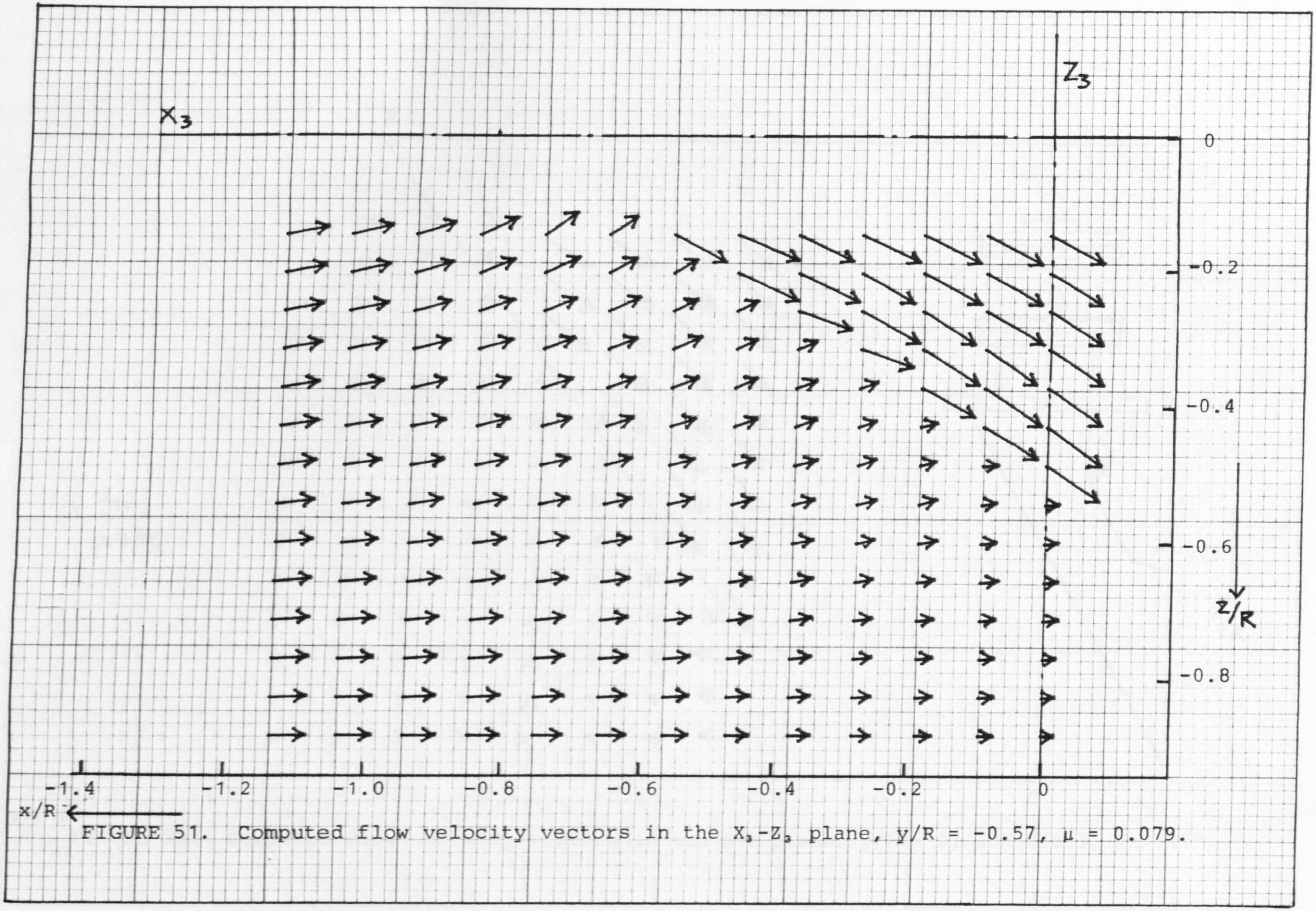

FIGURE 51. Computed flow velocity vectors in the X_3-Z_3 plane, y/R = -0.57, μ = 0.079.

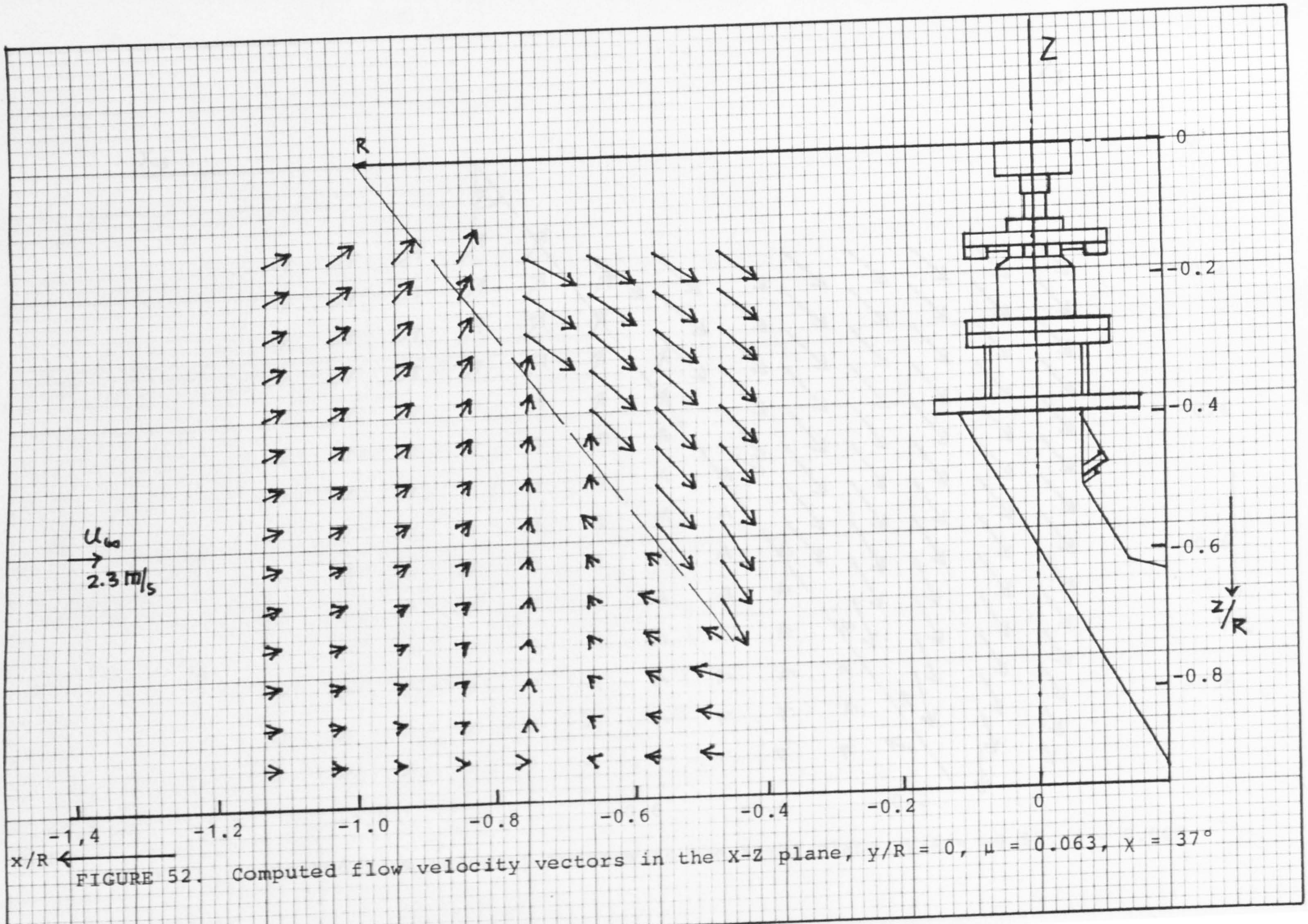

FIGURE 52. Computed flow velocity vectors in the X-Z plane, y/R = 0, μ = 0.063, χ = 37°

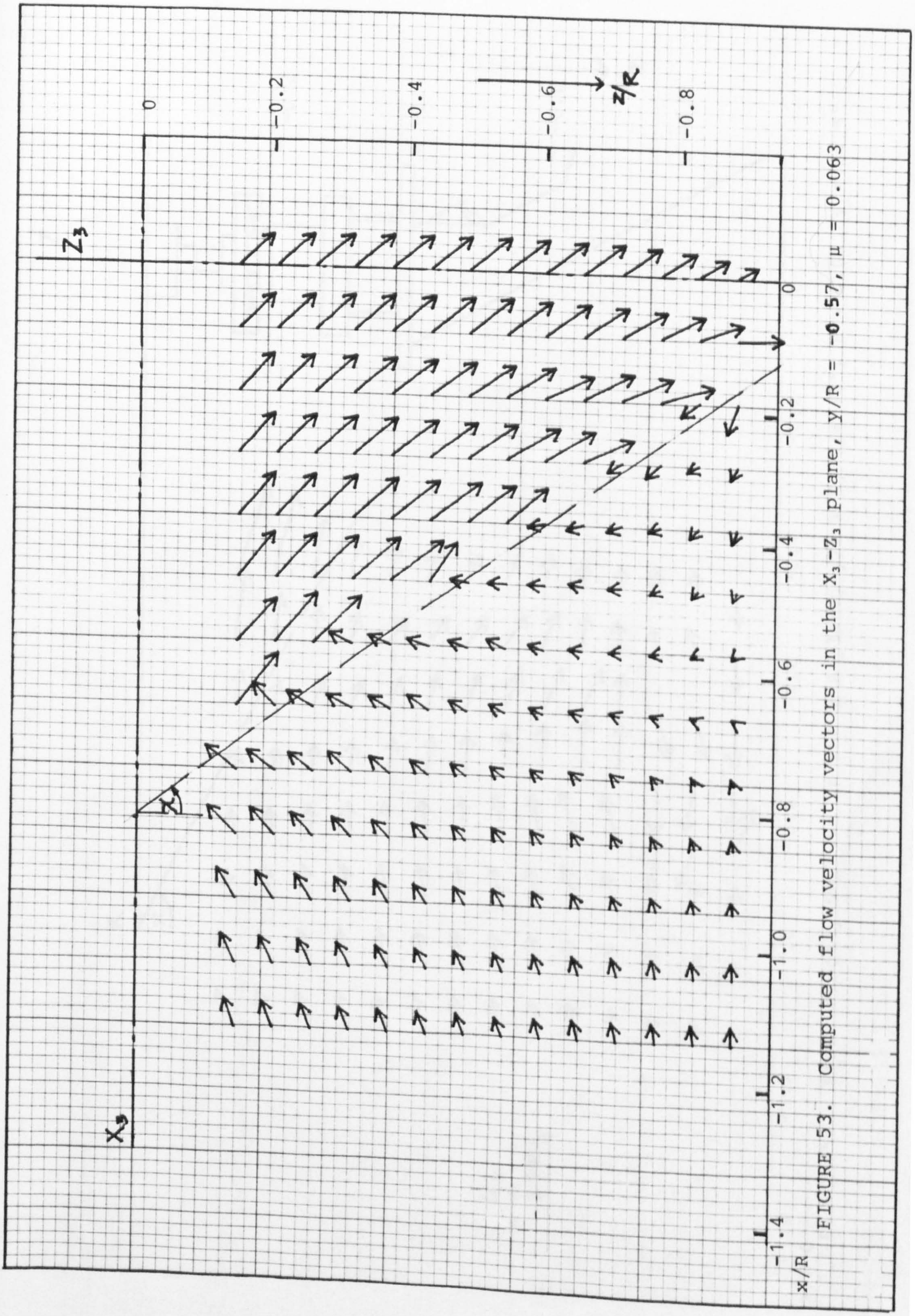

FIGURE 53. Computed flo

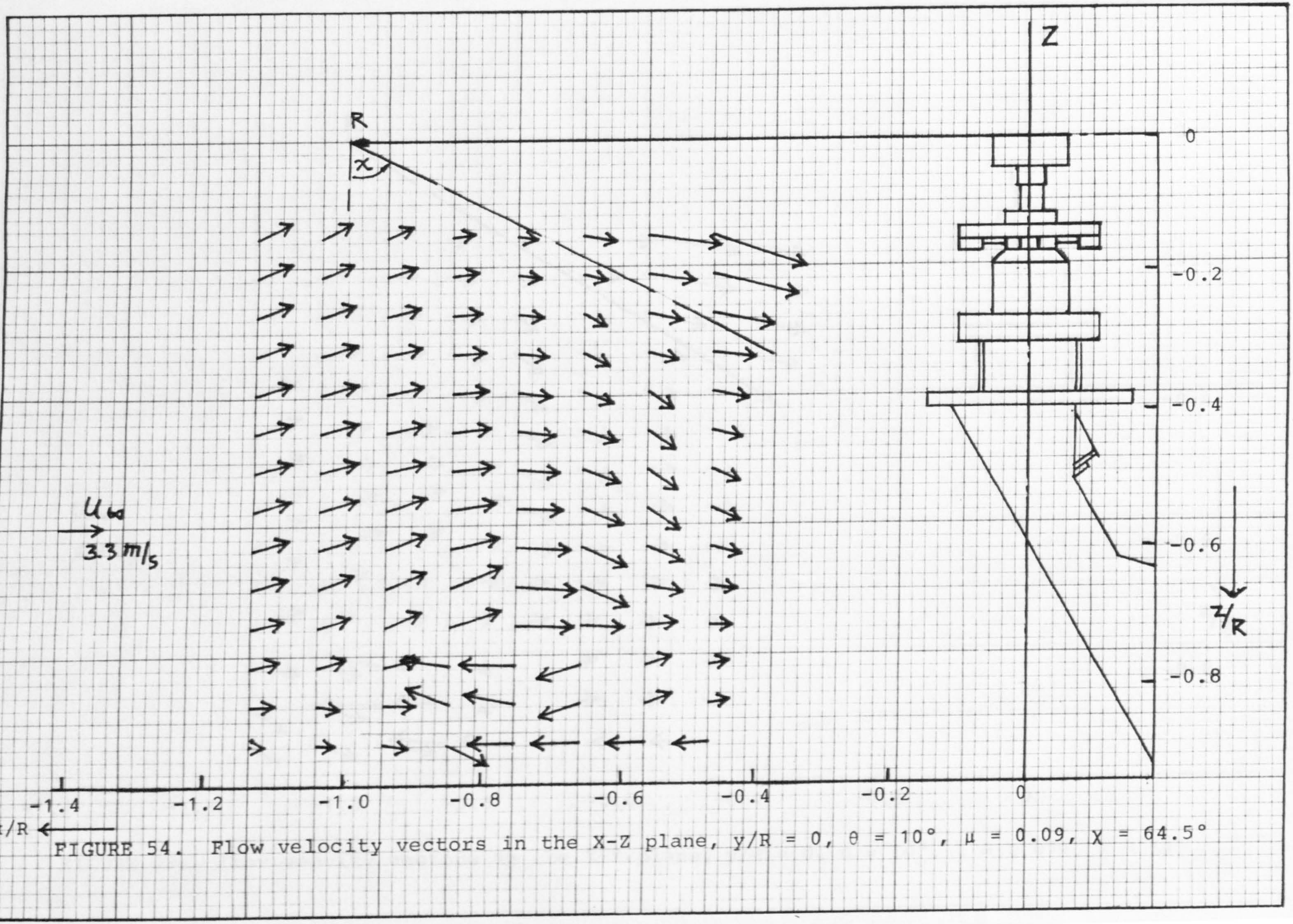

FIGURE 54. Flow velocity vectors in the X-Z plane, y/R = 0, θ = 10°, μ = 0.09, χ = 64.5°

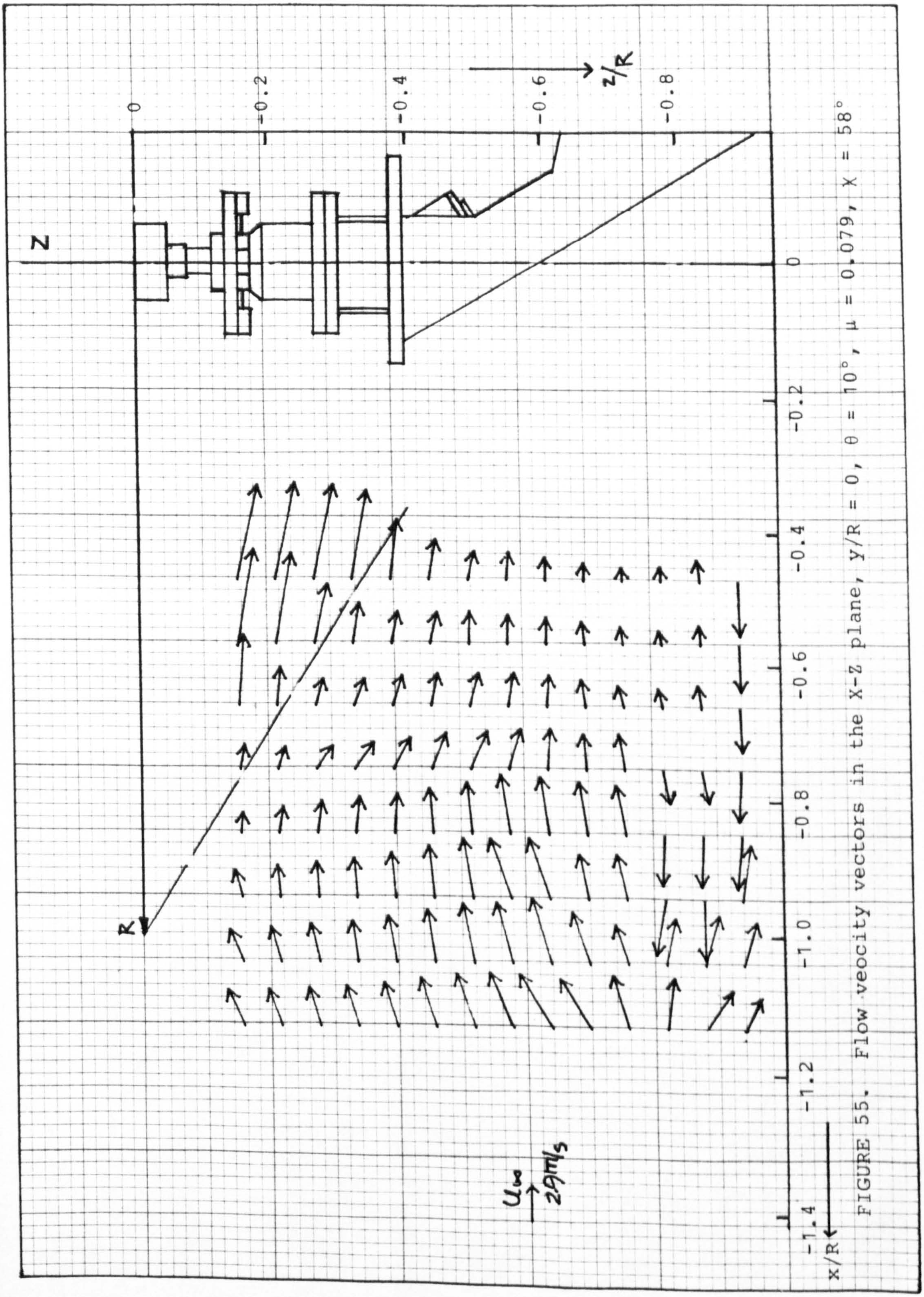

FIGURE 55. Flow veo